MASTER'S THESIS

Development of a Mesoporous Silica-based mid-Infrared Biosensor for the Quantification FAME in Jet fuel

carried out at the

Institute of Chemical Technologies and Analytics
Research Group for Process Analytics

under the supervision of

Univ.Prof. Bernhard Lendl
Projektass. Dipl.-Ing. Felix Frank

by

Adea Loxha, BSc
11728983
[redacted]

Vienna, 10.06.2024

Eidesstattliche Erklärung: Ich erkläre hiermit an Eides statt, dass ich die vorliegende Arbeit selbstständig verfasst, andere als die angegebenen Quellen/Hilfsmittel nicht benutzt, und die den benutzten Quellen wörtlich und inhaltlich entnommenen Stellen als solche kenntlich gemacht habe.

Statutory declaration: I hereby declare that I have authored this thesis independently, that I have not used other than the declared sources/resources, and that I have explicitly marked all material which has been quoted either literally or by content from the used sources.

Abstract

Jet fuel in Europe is often transported though the same pipelines and tankers as biodiesel. This leads to the contamination of the kerosene with fatty acid methyl esters (FAME), which diminishes the quality of the fuel. Therefore, it is important to monitor and quantify the FAME in kerosene before usage. The measurement is usually performed off-line in test labs. The goal of this thesis is the development of a biosensor for the quantification of FAME which can be used at-line, making the testing more time efficient. The enzyme lipase should be used for selective reaction of FAME in a complex matrix. In the mid-infrared, biosensors can be successfully realized by immobilizing the bioactive substance (ipase) in the evanescent field of attenuated total reflection (ATR) crystals allowing for the real-time monitoring of the catalyzed reaction. The effectiveness of this approach can be enhanced by employing mesoporous layers to significantly increase the surface area and, thus, the number of bioactive enzymes in the spectroscopically probed volume.

This study aimed to enhance the substrate quantification of enzymatic reactions, specifically investigating hydrolysis and aminolysis using FTIR spectroscopy. Of special interest was the optimization of the aminolysis reaction of FAME facilitated by a lipase as the foundation for the biosensor. A comprehensive study of suitable lipase-substrate pairs was performed to determine the most efficient pairings. Further, mesoporous silica films, which were optimized to attain pore sizes of approx. 8 nm and a layer thickness of 500 nm, were applied onto Si ATR crystals. Lipase enzymes were then immobilized onto these silica films, leveraging their unique structure to facilitate enzyme attachment and further serve as an enrichment layer for the analyte. This approach demonstrates the applicability of mesoporous silica film-coated ATR crystals in overcoming challenges associated with traditional biosensors in IR spectroscopy.

With a functioning enzymatic system, an adequate mesoporous layer and successful immobilization, these findings hold promise for advancing biosensing capabilities by combining mesoporous silica films and ATR-FTIR spectroscopy, not only for quantification and in-situ reaction monitoring via IR but also enhancing enzymatic sensor technology.

Kurzfassung

Jet-Kraftstoff in Europa wird oft durch dieselben Pipelines und Tanker wie Biodiesel transportiert. Dies führt zu einer Kontamination des Kerosins mit Fettsäuremethylestern (FSME), was die Qualität des Kraftstoffs mindert. Daher ist es wichtig, FSME im Kerosin vor der Verwendung zu überwachen und zu quantifizieren. Die Messung wird normalerweise off-line in Testlabors durchgeführt. Ziel dieser Arbeit ist die Entwicklung eines Biosensors zur Quantifizierung von FSME, der at-line verwendet werden kann, um die Prüfung effizienter zu gestalten. Das Enzym Lipase soll für die selektive Reaktion von FSME in einer komplexen Matrix eingesetzt werden. Im mittleren Infrarotbereich können Biosensoren erfolgreich realisiert werden, indem die bioaktive Substanz (Lipase) im evaneszenten Feld von abgeschwächten Totalreflexions- (ATR) Kristallen immobilisiert wird, wodurch eine Echtzeitüberwachung der katalysierten Reaktion ermöglicht wird. Die Effektivität dieses Ansatzes kann durch den Einsatz von mesoporösen Schichten verbessert werden, um die Oberfläche und damit die Anzahl der bioaktiven Enzyme im spektroskopisch untersuchten Volumen erheblich zu erhöhen.

Diese Arbeit zielte darauf ab, die Substratquantifizierung enzymatischer Reaktionen zu verbessern, wobei insbesondere die Hydrolyse und Aminolyse mittels FTIR-Spektroskopie untersucht wurden. Besonderes Interesse galt der Optimierung der Aminolyse-Reaktion von FSME, die durch eine Lipase katalysiert wurde, als Grundlage für den Biosensor. Eine umfassende Untersuchung geeigneter Lipase-Substrat-Paare wurde durchgeführt, um die effizientesten Paarungen zu bestimmen. Weiterhin wurden mesoporöse Siliciumdioxid-Filme, die auf eine Porengröße von ca. 8 nm und eine Schichtdicke von 500 nm optimiert wurden, auf Si-ATR-Kristalle aufgebracht. Lipase-Enzyme wurden dann auf diesen Siliciumdioxid-Filmen immobilisiert, wobei deren einzigartige Struktur genutzt wurde, um die Enzymadsorption zu erleichtern und weiterhin als Anreicherungsschicht für den Analyten zu dienen. Dieser Ansatz zeigt die Anwendbarkeit von mesoporösen Siliciumdioxid-Film-beschichteten ATR-Kristallen zur Überwindung von Herausforderungen, die mit traditionellen Biosensoren in der IR-Spektroskopie verbunden sind.

Mit einem funktionierenden enzymatischen System, einer angemessenen mesoporösen Schicht und erfolgreicher Immobilisierung zeigen diese Erkenntnisse vielversprechende

Fortschritte für die Biosensortechnologie, indem mesoporöse Siliciumdioxid-Filme und ATR-FTIR-Spektroskopie kombiniert werden, nicht nur zur Quantifizierung und *in-situ* Reaktionsüberwachung mittels IR, sondern auch zur Verbesserung der enzymatischen Sensortechnologie.

Acknowledgments

I want to acknowledge the European Union's Horizon Research and Innovation Programme for funding the BROMEDIR project (101092697), and thus this work.

First and foremost, I would like to express my gratitude to Prof. Bernhard Lendl, for finding me a spot in his group to conduct my research in. His leadership and vision have been instrumental in guiding my work and ensuring its success.

I am very grateful to my supervisor, Felix Frank. Felix, you always ensured that everything ran smoothly and offered your help whenever I needed it. Your respect for my input and your encouragement have greatly enriched my experience.

To Sebastian and Lisa, my bros, your emotional support and our Aperol evenings have meant the world to me. You two have made the challenging moments much easier to bear. My Master's wouldn't have been half as much fun without you.

I would also like to acknowledge the wonderful members of the research group (CAVS) who contributed to a vibrant and enjoyable work environment: Shilpa, Loisi, Daniel, Dani, Leo, Lena, Ufuk, Dominik, Alicja, Iskander, Davide, Giovanna, Georg, Savda, Alex, Elisabeth, Jesus, Yide, Paul, Harald, Gustavo and Elizandra.

My heartfelt thanks go to my closest companions throughout my studies: Geri, Rares, Michi, Miranda, Edma, Schnölli and Lukas. The laughter and memories we've shared have been a highlight in my academic journey.

To my boyfriend, Basti, your support through all my mental breakdowns and your steadfast encouragement have been a cornerstone of my strength. From the first day of university as a friend and now as a partner, you have always been there for me.

I want to express my gratitude to my parents and brother. Your encouragement from the very beginning, despite the challenges of letting me go for my studies, has been unwavering. Mom, thank you for listening to every detail of everyday of my studies. Dad, your reminders to see the bigger picture have guided me through many tough decisions. Ardi, thank you for the books and IT consulting.

I also want to thank Michael Stöger-Pollach (USTEM, TU Wien) for TEM measurements and Werner Artner (XRC, TU Wien) for his support with XRD measurements and interpretation.

Last but not least, I would like to thank myself for having delved into enzyme kinetics, despite my previous decision of never dealing with biochemistry topics again. 'Twas more fun than expected.

Abbreviations

2MEA	2-MethoxyEthylAmine
3DAPA	3-(DimethylAmino)-1-PropylAmine
3MPA	3-MethoxyPropylAmine
3PPA	Iso-PropoxyPropylAmine
ALA	Amino Lipase A from Aspergillus niger
ALPF	Amano Lipase from Pseudomonas Fluorescens
APTES	(3-AminoPropyl)TriEthoxySilane
ATR	Attenuated-Total-Reflection
BSA	Bovine Serum Albumine
CALB	Candida Antarctica Lipase B
CMC	Critical Micelle Concentration
CPTES	(3-ChloroPropyl)TriEthoxySilane
CTAB	CetylTrimethylAmmonium Bromide
DLS	Dynamic Light Scattering
EC	Enzyme Commision
EISA	Evaporation Induced Self Assembly
EtOH	Ethanol
F127	Pluronic® F-127
FAME	Fatty Acid Methyl Ester

FIB	Focused Ion Beam
FIR	Far-InfraRed
FKM	Gluoro Rubber Material
FSME	FettSäureMethylEster
FTIR	Fourier-Transform InfraRed
GC-MS	Gas Chromatography Mass Spectrometry
HMDS	HexaMethylDiSilazane
HPLC	High Performance Liquid Chrmoatography
IR	InfraRed
IRE	Internal Reflection Element
LCR	Lipase from Candida Rugosa
LOD	Limit Of Detection
MM	Methyl Mytistate
MIR	Mid-InfraRed
NIR	Near-InfraRed
PMMA	PolyMethylMethAcrylate
PZC	Point of Zero Charge
RH	Relative Humidity
SA-XRD	Small-Angle X-Ray Diffraction
SDS	Sodium Dodecyl Sulfate
TEOS	TetraEthyl OrthoSilicate
TEM	Transmission Electron Microscopy

Contents

1. Motivation

The composition of kerosene (jet fuel) has rigid specifications and needs to continuously be monitored to detect contaminants. In Europe, the same transportation infrastructures (i.e. cargo tankers and pipelines) are employed to move different fuels, biodiesel among others. Biodiesel is a term reserved for diesel that consists in part of fatty acid methyl esters (FAME), which can be used as fuel as well. They are produced from a base catalyzed transesterification of triacylgycerides (fats and oils), and added to conventional diesel fuel. Fatty acid methyl esters have a tendency to adsorb on surfaces and the metal surfaces of pipelines are no exception. Therefore, transporting biodiesel prior to kerosene leads to a contamination of the jet fuel with FAME. As FAME have a different composition compared to the components of jet fuel, they therefore have different properties that are not compatible the systems set in place for kerosene. For this reason, the maximum concentration of FAME allowed in kerosene is regulated by the Defence Standard 91-091 and is set to $50\,\mathrm{mg\,mL^{-1}}$.[1] Consequently, the FAME concentration in kerosene needs to be monitored to ensure that the limit is not exceeded. This is typically done by standardized methods such as FTIR (IP 583), GC-MS (IP 585), or HPLC (IP 590). The disadvantage of these procedures lies in their off-line execution, and while accurate, they are not time efficient.

This work aims to provide the first steps to developing a biosensor for the determination of FAME in jet fuel, which can be used at-line. The idea for this biosensor is based on a similar project from Quantared Technologies GmbH.[2] In their approach, the sample is passed in a loop though a cartridge filled with immobilized enzyme, where it is converted to another compound after an amine reactant is injected. The sample is measured by transmission IR spectroscopy before the amine injection and after 23 min. The enzyme, in the presence of an amine, catalyzes an aminolysis reaction, converting the fatty acid methyl esters into fatty acid amides. Consequently, there is a decrease of the ester carbonyl IR band at $1749\,\mathrm{cm^{-1}}$, through which the FAME concentration in the sample can be calculated.[3] The goal of this thesis is to build on this idea and improve the sensitivity, as well as have the reaction and the measurement happen simultaneously in the same part of the biosensor, thus compacting the biosensor.

The biosensor proposed in this thesis is an attenuated total reflection (ATR) FTIR-based enzymatic sensor. Similarly to the approach by Quantared, the enzymatic aminolysis reaction is the center of this biosensor. Mid-infrared radiation is suitable for detection, since the carbonyl absorption band of FAME with 5.7 μm falls within the wavelength range of this radiation. The shift of the carbonyl band from and ester to an amide can utilized for quantification. A mesoporous silica film on top of the ATR crystal is to be used as immobilization substrate for the enzymes. The mesoporous silica also serves a second purpose, as it should function as an enrichment layer for the FAME and product, thus, improving the sensitivity of the method. The first aspect this work deals with is the optimization of the synthesis of the mesoporous silica film and its characterization; the pores need to be large enough for the enzyme to be accommodated and the layer thickness needs to be tuned with respect to the evanescent field of the ATR. The second aspect of the thesis deals with the optimization of the enzymatic aminolysis, as the reaction is not as straightforward as other enzymatic reactions. Lastly, the enzymes need to be successfully immobilized and the reaction needs to be tested within the mesoporous layer. With the successful implementation these mentioned goals, the initial part of the biosensor development would be seen as complete.

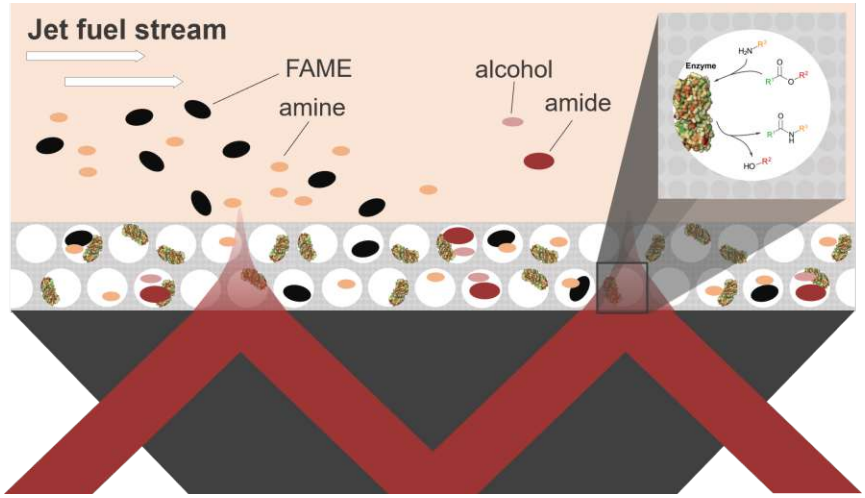

Figure 1.1.: Schematic visualization of the biosensor.

2. Theoretical Introduction

The first part of this theoretical introduction, section 2.1., provides a short summary of infrared spectroscopy, the analytical method for the proposed biosensor. Section 2.2. offers insights on mesoporous silica, the enzyme substrate and enrichment layer of the senor. The background of the enzymatic reaction, which is quintessential for this work, is presented in section 2.3.. Lastly, to understand how all the components work together, a brief introduction into biosensors can be found in section 2.4..

2.1. Fundamentals of Infrared Spectroscopy

As is the case for all kinds of spectroscopies, infrared (IR) spectroscopy utilizes the interaction between electromagnetic radiation and matter to gain chemical and physical information. Operating within the wavelength range of 700 nm to 1 mm, IR spectroscopy utilizes radiation absorbed or scattered by the target molecule. Since energy of molecules is quantized, it is imperative for the incoming radiation to have the appropriate energy in order to get absorbed. The appropriate energy, in this case, refers the energy that is needed to promote the molecule to transition to a higher energy state. IR radiation induces (what are called) vibrational as well as rotational-vibrational transitions. These vibrations involve stretching and bending of the chemical bonds that hold the atoms together. Thus, the energy that is absorbed is structure dependent. Further, the dipole selection rule needs to be fulfilled, i.e. the dipole moment of the molecule needs to change upon absorption of radiation. Molecules have different vibrational modes based on the movement of their atoms relative to each other. Not all vibrational modes cause a change in dipole moment, but the ones that do are asymmetric and symmetric stretching, as well as bendings such as scissoring, wagging, rocking, and twisting.

Theoretical foundations of molecular vibrations can be modeled by Hooke's Law, governing harmonic oscillators behavior, described by the differential equation:

$$\ddot{x} + \frac{k}{\mu} \cdot x = 0, \tag{2.1}$$

which has the following solutions, describing the vibration of an atom in a molecule:

$$x(t) = A \cdot sin\left(\sqrt{\frac{k}{\mu}} \cdot t\right); x(t) = B \cdot cos\left(\sqrt{\frac{k}{\mu}} \cdot t\right), \tag{2.2}$$

where k is the spring constant, μ the reduced mass, t the time and x is the displacement from the equilibrium position. Since in molecules the vibrational energy is quantized, the vibrational energy levels are denoted by:

$$E_\upsilon = \left(\upsilon + \frac{1}{2}\right) h\nu \tag{2.3}$$

where E_υ is is the energy of the n-th vibrational level, ν the *resonant frequency*, h Planck's constant, and υ the *vibrational quantum number* ($\upsilon = 0, 1, 2, ...$). Selection rules, governed by the quantum mechanical principles of symmetry, dictate which transitions are allowed. For a diatomic molecule, the selection rules state that only transitions with a change in vibrational quantum number $\Delta\upsilon = \pm 1$ are possible.

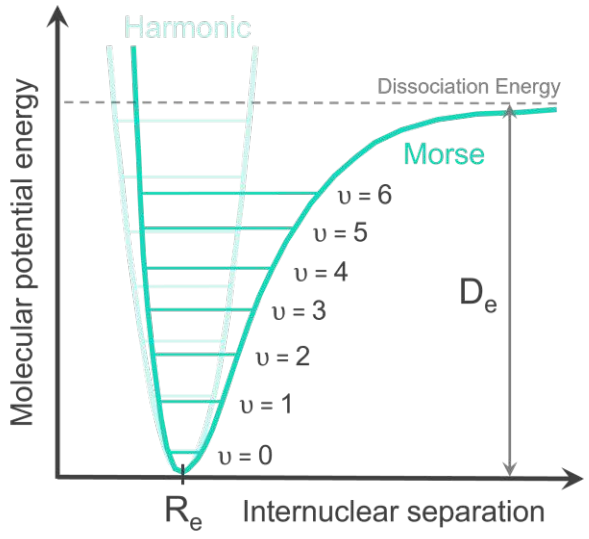

Figure 2.1.: Harmonic and Morse potential for describing the vibrational energy levels of molecules. The depth of the Morse potential, contrary to the harmonic potential, is not infinite, as there is an amount of energy (D_e) after the absorption of which the bond between the two atoms dissociates.

However, the harmonic oscillator model has limitations. It assumes that bonds behave purely harmonically, neglecting the anharmonicity of real molecular vibrations. The Morse potential model (Figure 2.1) provides a more accurate description of molecular vibrations by considering anharmonicity. Unlike the simple quadratic potential in the harmonic oscillator

model, the Morse potential includes a potential energy curve with a finite depth and therefore a dissociation energy. This allows for more realistic descriptions of molecular vibrations, especially at higher energy levels. In the Morse potential model, the energy levels are given by:

$$E_\upsilon = h\nu \left[\left(\upsilon + \frac{1}{2} \right) - \chi_e \left(\upsilon + \frac{1}{2} \right)^2 \right], \tag{2.4}$$

where χ_e is the *anharmonicity constant*, which is dependent on the dissociation energy (D_e) of the bond in the molecule. When anharmonicity is taken into account, the selection rule is less stringent, allowing overtones and combination vibrations.

In IR spectroscopy, the absorption peaks in the resulting spectrum denote the frequencies of infrared radiation that are absorbed by the molecule, signaling transitions between vibrational energy levels. These peaks, influenced by structure and transition dipole moments, hold information about molecular composition, functional groups, and bonding.

Fourier-Transform Infrared Spectroscopy

Instead of sequentially scanning each wavelength individually to produce a spectrum, as is the case for dispersive IR spectroscopy, Fourier-transform infrared (FTIR) spectroscopy simultaneously collects data across a broad spectral range. The technique relies on interferometry, where the sample's response to infrared light is transformed into an interferogram. This is done for both the light intensity before, I_0, and after the sample, I. Subsequently, by mathematically Fourier transforming the interferograms, the absorpotion spectra can be attained.[4–6]

Interferometers, which are typically based on a Michelson interferometer[7], split the infrared beam into two paths. One path reflects off a fixed mirror and the other off a movable mirror. The beams then recombine, producing an interference pattern. The recombined beam passes through the sample, where the infrared light interacts with the sample molecules. The transmitted light is detected and recorded as an interferogram, which is mathematically transformed into an infrared spectrum.[5, 6]

2.1.1. Mid-Infrared Spectroscopy

Within the electromagnetic spectrum, the wavelength of infrared radiation lies between visible light and microwave light, as is schematically visualized in Figure 2.2. The typical wavelength range for infrared radiation lies between $\lambda = 700\,\mathrm{nm}$ and $\lambda = 1\,\mathrm{mm}$. The

energy, E and the frequency, ν of the radiation are directly related to its wavelength, λ by *Planck's relation*:

$$E = h\nu = h\frac{c}{\lambda} = hc\tilde{\nu} \tag{2.5}$$

where c is the speed of light and $\tilde{\nu}$ the wavenumber. Infrared spectra are commonly depicted in wavenumbers (cm^{-1}).

Infrared is further divided into the near infrared region (NIR), 700-2500 nm (12500-4000 cm^{-1}), the mid infrared region (MIR), 2.5-25 μm (4000-400 cm^{-1}), and far infrared region (FIR), 25-1000 μm (400-10 cm^{-1}). In the MIR spectral region most of the fundamental structural information is attained, as it has the adequate energy for exciting fundamental molecular vibrations. On the other hand, NIR is responsible for exciting overtones and combination bands. Therefore, MIR is advantageous for determining molecular structures, as well as for the quantification based on absorption bands, especially for organic molecules. It is also used for identifying molecules, since it entails all fundamental vibrations. This is often described as the fingerprint region.[6]

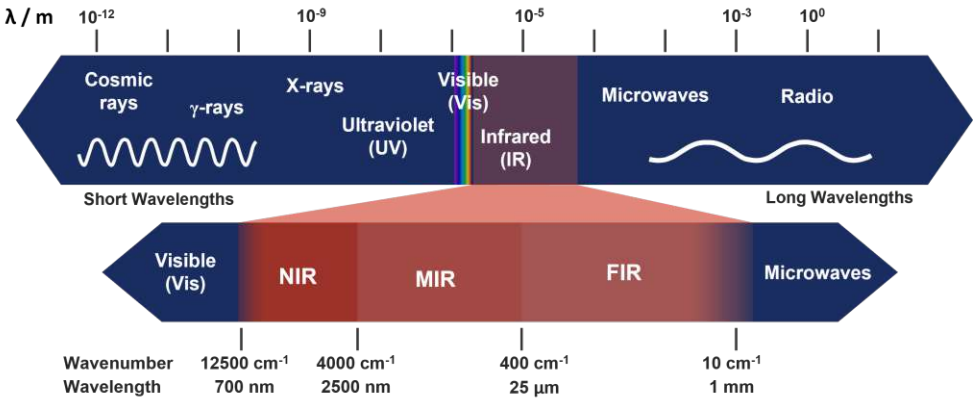

Figure 2.2.: Electromagnetic spectrum with a sub-categorization of the IR region. Adapted from [8]

2.1.2. Transmission Infrared Spectroscopy

Transmission IR spectroscopy is a technique used to analyze the absorption of IR radiation by a sample as the radiation passes through it. In this method, a beam of infrared light is directed through a sample, and the intensity of the transmitted light is measured as a function of wavelength. As stated in Section 2.1., an analyte absorbs specific wavelengths of infrared radiation depending on its molecular composition, which results in characteristic

absorption bands in the spectrum. The absorbance of the analyte can be calculated from the intensity of the incident radiation after measuring a sample with (I) and without (I_0) the analyte (reference), according to *Lambert Beer's* law, as shown in Equation 2.6. Based on this law, the absorbance, A, of a sample depends linearly on the pathlength the light travels though the sample, d, the concentration of the analyte, c, and the molar decadic absorption coefficient, ε.

$$A = -log_{10}\left(\frac{I}{I_0}\right) = \varepsilon cd \tag{2.6}$$

The pathlength is a point of contention, especially with the MIR, because a lot of molecules absorb strongly in this region. This makes the detection of low concentration of analytes is solvents such as water, which is a strong absorber, quite difficult.

2.1.3. Attenuated Total Reflection Spectroscopy

The basis of attenuated total reflection (ATR) spectroscopy lies in utilizing the phenomenon of total reflection of infrared radiation at the interface between two materials with different refractive indices. The refractive index (n) of a material determines the speed and direction of light propagation within that material. When light encounters a boundary between two materials with different refractive indices, its direction changes (i.e. it gets refracted) according to Snell's Law (Figure 2.3-a):[5, 6]

$$n_1 sin(\theta_1) = n_2 sin(\theta_2) \tag{2.7}$$

where n_1 and n_2 are the refractive indices of the first and second materials, respectively, and θ_1 and θ_2 are the angles of incidence and refraction, respectively. Snell's Law also describes the phenomenon of total reflection, where the radiation is not refracted anymore (Figure 2.3-a). This occurs when light traveling in a high refractive index material encounters a boundary with a lower refractive index material at an angle greater than the critical angle θ_c:[5]

$$\theta_c = arcsin\left(\frac{n_2}{n_1}\right) \tag{2.8}$$

n_1 being the refractive index of the optically denser and n_2 of the optically rarer medium.

ATR spectroscopy typically involves a crystal or prism made of a high refractive index material, known as internal reflection elements (IRE), such as silicon, germanium, or zinc selenide, in contact with the sample of interest. The IR beam passes through the IRE to get in contact with the sample. If the angle of the incident IR radiation exceeds θ_c, the

beam reflects internally, therefore, the light does not pass through the sample, as is the case for a transition measurement. However, as light is comprised of an electromagnetic field, an evanescent wave is formed upon local reflection between the IRE and the sample, that extends into the sample. This evanescent wave can interact with the sample (Figure 2.3-b). The strength E of this field decays exponentially with distance z from the interface:[5]

$$E(z) = E_0 e^{-\gamma z} \tag{2.9}$$

where E_0 is the initial strength of the field and γ the *decay constant*. The depth which the evanescent wave reaches before its strength dropping to $1/e$ of its initial strength is called depth of penetration. It essentially determines the portion of the sample probed by the ATR technique. By knowing the wavelength, λ_0, and angle, θ_1, of the incident light and both the refractive indices of the IRE, n_1, and the sample, n_2, it can be calculated following Equation 2.9.[5, 6]

$$d_p = \frac{1}{\gamma} = \frac{\lambda_0}{2\pi n_1 \sqrt{sin^2\theta - \left(\frac{n_2}{n_1}\right)^2}} \tag{2.10}$$

For a given wavelength, the depth of penetration can be tuned by changing the incident angle and/or the IRE material. To be able to compare ATR to transmission spectra, the effective penetration depth, d_e, is a more practical value. The effective penetration depth is defined as the equivalent pathlength in a transmission experiment, which matches the absorbance spectrum attained by a single-bounce ATR experiment. Its value is polarization dependent. For weakly absorbing samples, d_e for the parallel component of the electric field vector is defined as:[6, 9, 10]

$$d_{e,p} = \frac{n_{21}\lambda_0 cos\theta(2sin^2\theta - n_{21})}{n_1\pi(1-n_{21}^2)[(1+n_{21}^2)sin^2\theta - n_{21}^2]\sqrt{(sin^2\theta - n_{21}^2)}} \tag{2.11}$$

and for the perpendicular component of the electric field vector, the value of $d_{e,s}$ is:

$$d_{e,s} = \frac{n_{21}\lambda_0 cos\theta}{n_1\pi(1-n_{21}^2)\sqrt{(sin^2\theta - n_{21}^2)}} \tag{2.12}$$

where $n_{21} = \frac{n_2}{n_1}$. Typically, the average of $d_{e,p}$ and $d_{e,s}$ is taken as an approximate value for the effective penetration depth of unpolarized light. In case of a multi-bounce ATR crystal the value of d_e for one bounce is multipiled by the number of bounces. This value, be it for a singe bounce or multi-bounce crystal, can then be used in Lambert Beer's law:[5]

$$A = \varepsilon c d_e \tag{2.13}$$

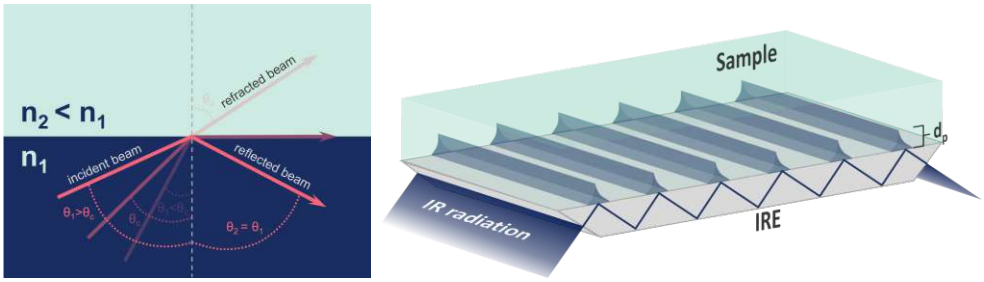

(a) (b)

Figure 2.3.: (a) Refraction and reflection of light. While the incidence angle of the radiation is smaller than the critical angle, the light is refracted into the optically rarer medium. After the incidence angle surpasses the critical angle, no refraction takes place anymore and the light is totally reflected back into the optically denser medium. (b) Schematic depiction of a multi-bounce ATR crystal and the penetration of the evanescent wave.

2.2. Synthesis of Mesoporous Films

2.2.1. The Sol-Gel Process

The sol-gel process is the typical synthesis method for attaining mesoporous silica layers and was utilized in this thesis as well.

The first steps towards sol-gel chemistry were done in 1824 by Ebelmen[11] and the term was first introduced by Graham in 1864[12], though the first attempts of making use of this for oxide films are attributed to Geffken and the German company Schott[13]. Later, the process was described by Schröder[14] and in the 1970s sol-gel processing started being used worldwide for the production of glass and ceramics at low temperatures.[15] Now, the sol-gel process has found a broad spectrum of applications in different fields, i.e. material development, drug delivery, separation and catalysis.[16]

To understand the process, it is important to understand the concepts of the two steps it encompasses. The sol represents a suspension of colloidal solid particles in a liquid, where the influence of gravity on the dispersed phase is negligible due to the nano-scale of these particles. A gel is a cross-linked continuous three dimensional network, which is still immersed in a liquid medium.[17–19] The process that connects these two states, producing inorganic oxides (ceramics), is known as the sol-gel process.[20]

The foundation of this process is built on two key reactions: hydrolysis and condensation.

During the hydrolysis reaction, silicon-oxygen bonds in the alkoxide are broken, and hydroxyl groups from water are incorporated into the silicon compound. This process results in the formation of silanol (Si-OH) groups. This transformation is illustrated in the initial reaction depicted in Figure 2.4. Condensation of the formed -OH moieties proceeds in either of two pathways, yielding either alcohol or water, as illustrated in the final two reactions in Figure 2.4. In both cases, a siloxane bond is formed and when the number of these bonds is maximized, a gel is formed.[17, 19]

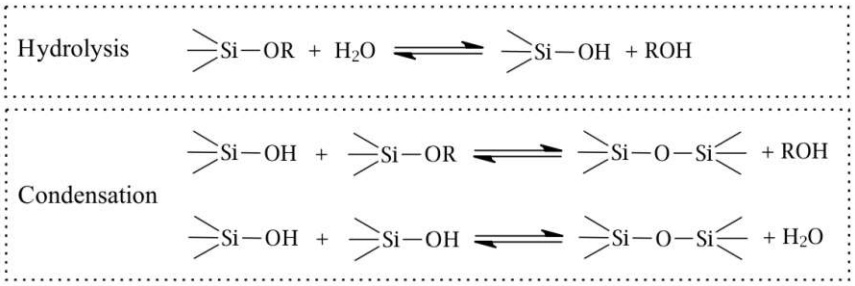

Figure 2.4.: General sol-gel two-step reaction mechanism.

The reactants and reaction conditions are crucial for the properties of the final product.[17, 18] The precursor molecule are usually metal or metalloid salts and alkoxides, though there are numerous other precursors.[20] Silicon compounds, particularly silicon alkoxides such as tetraethyl orthosilicate (TEOS), are very prevalent precursors. This is due to the fact that they are cheap, easily accessible, and also easy to handle.[15, 18] One more important aspect to consider is that gels form more favorably compared to powders only when the hydrolysis reaction is slower than the condensation. While other compounds need agents to slow the hydrolysis reaction, silicon compounds innately favor the condensation reaction, since silicon is less electro-positive and less susceptible to nucleophilic attacks.[20]

As tetraalkoxysilanes like TEOS are immiscible with water, an alcohol, usually ethanol (EtOH), is used as a solvent during the synthesis. Water is not completely removed from the solution, since it is necessary for the hydrolysis reaction to take place. Furthermore, both the hydrolysis and condensation reaction needs to be catalyzed by an acid or a base. While working with Si, its point of zero charge (PZC) is an important aspect to consider during the synthesis. It can be differentiated between two pathways (reaction mechanisms) based on the pH of the sol solution: pH below 2.5 (PZC of Si) and pH above 2.5. This is one of the key factors for the structural evolution of the gel and the final product. Acid-catalyzed hydrolysis yields polymer-like branched sols, while base-catalyzed

hydrolysis produces highly condensed particulate sols. The structural evolution based on the pH conditions is depicted in Figure 2.5.[17, 18]

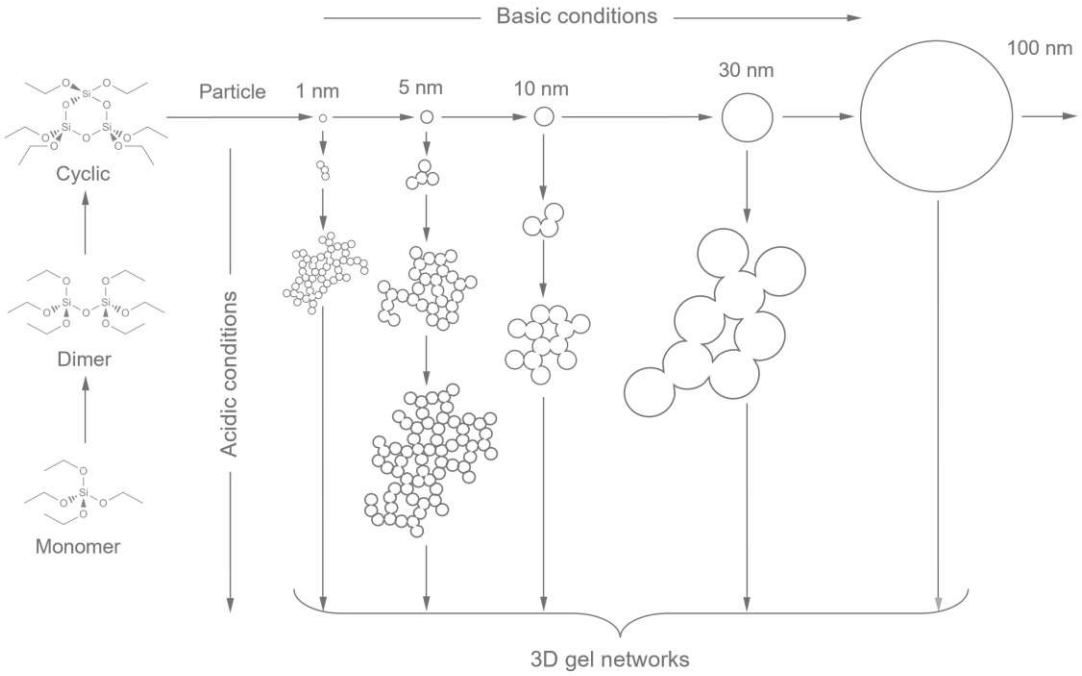

Figure 2.5.: Silica particle structure growth based on pH conditions starting from the precursor.

Relevant for this work is the acid catalyzed process and will therefore be explained further. The general hydrolysis and condensation reactions under acidic conditions are shown in Figure 2.6.

Hydrolysis likely proceeds via bimolecular nucleophilic displacement (S_N2) reactions (Figure 2.7). Under acidic conditions, the protonation of Si-OR groups creates good leaving groups and increases electrophilicity at the central silicon atom, thus, making it more prone to a nucleophilic attack. This facilitates hydrolysis or condensation reactions, where either water or a silanol group attack from the rear, creating a transition state. The positive charge on the protonated alkoxide is consequently diminished, thereby making alcohol a leaving group. The transition state breaks down as the alcohol is displaced, accompanied by the inversion of the silicon tetrahedron.[17, 18]

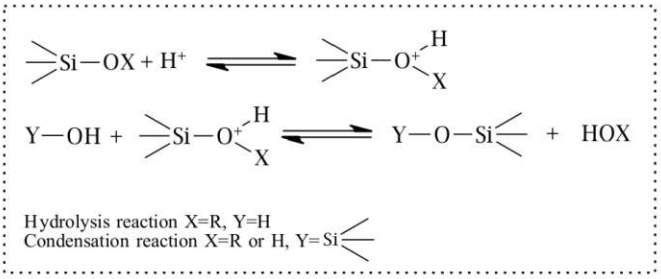

Figure 2.6.: Sol-gel hydrolysis and condensation reaction under acidic conditions.

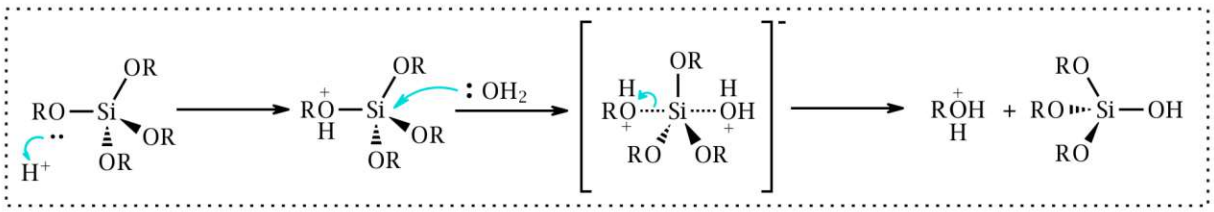

Figure 2.7.: S_N2 reaction mechanism under acidic conditions during sol-gel synthesis.

For acidic catalysts, higher electron density is preferred as it stabilizes the positively charged transition state more effectively. Consequently, reactions tend to be slower for more highly substituted species. This results in faster hydrolysis for monomeric $Si(OR)_4$ compared to partially hydrolyzed or oligomeric species. The decrease in the point of zero charge (PZC) of the silicon compound with increased substitution correlates with this phenomenon. Notably, when the PZC aligns with the pH of the solution, acid catalysis ceases to occur. This means that gel networks are then formed from exceedingly small primary particles, favored by the hydrolysis and condensation occurring predominantly at terminal silicon atoms. This preference is accentuated by the rapid hydrolysis under such conditions.[17, 18]

Gelation marks a critical phase in the sol-gel transition, where small 3D oligomeric particles initially form nuclei with Si-OH groups on their surface, subsequently growing or agglomerating into clusters *via* condensation. At the gel point, a sudden increase in viscosity signifies the establishment of a continuous network, akin to the formation of a giant molecule. This transition occurs when condensation reactions reach a critical point when the clusters collide and form a spanning cluster. An oxide network is formed when the gel is dried, which is then called a xerogel.[17, 18, 20, 21]

2.2.2. Evaporation Induced Self Assembly and Spin-Coating of Mesoporous Films

For a multitude of applications, including this thesis, it is desirable for the mesoporous silica to be applied as a thin film as well as to have bigger and well-ordered pores. These attributes can be attained through combining self-assembly and spin-coating.

Self-assembly refers to the natural tendency of molecules to spontaneously arrange themselves into stable, organized structures through non-covalent bonding interactions.[22, 23] Molecules like surfactants are pre-programmed to behave like this, driven by their hydrophobic and hydrophilic parts.[20, 23] Based on the concentration, surfactants display different structures. At lower concentrations surfactants exist as free molecules. As the concentration increases just above the critical micelle concentration (CMC1), surfactant molecules aggregate into spherical shapes; with further elevation in concentration (CMC2), they adopt a cylindrical rod shape, followed by an even higher concentration leading to liquid-cystalline mesophases such as ordered hexagonal packing or a lamellar structure. This structural behaviour of surfactants is shown in Figure 2.8.[20, 23]

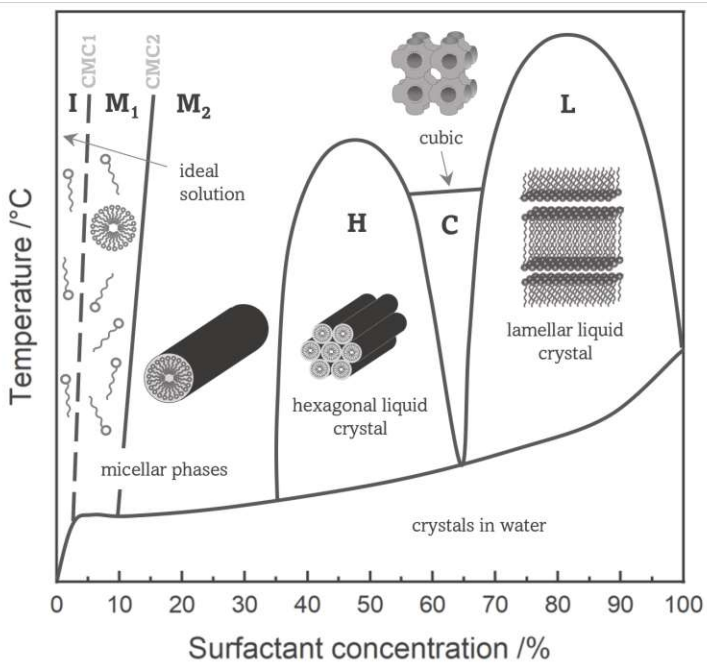

Figure 2.8.: Surfactant phase diagram showing the different structures formed by surfactants. The template that the surfactant forms is not only dependent on its concentration, but on the temperature as well.

Surfactants can be divided into four categories: anionic, cationic, non-ionic and amphoteric.[20]. Two of the most used surfactants in combination with mesoporous silica are alkylammonium surfactants such as cetyltrimethylammonium bromide (CTAB), which is a cationic surfactant, and pluronics such as F127, which is a nonionic block-copolymer (Figure 2.9).[20, 24, 25] CTAB was the first surfactant to be used in a mesoporous silica synthesis.[19] F127 is a poloxamer series of poly(ethylene oxide)-poly(propylene oxide)-poly(ethylene oxide) triblocks (PEO-PPO-PEO) which was used for the first time in combination with mesoporous silica by Zhao *et al.*[26] (hexagonal structure).

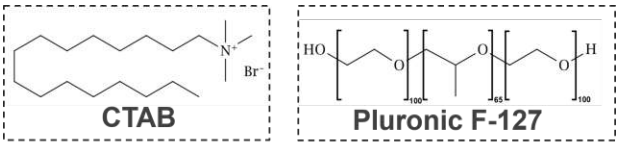

Figure 2.9.: Structural formula of the two surfactants used in this work, CTAB and F127.

These surfactants work as a template for the pores of the mesoporous silica.[20] The self-assembly of surfactant molecules drives the organization of molecular precursors into ordered structures. A schematic visualisation of this process is depicted in Figure 2.10. The first ones to discover this and use surfactants as directing agents in a mesoporous silica synthesis were scientists at Mobile Oil Research.[27]

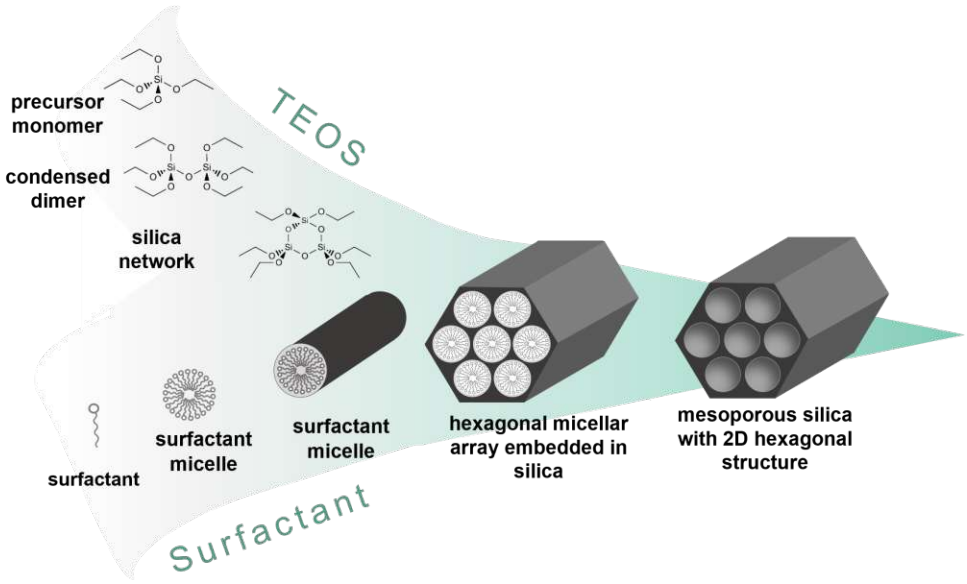

Figure 2.10.: Structure development of the surfactant templated mesoporous silica.

This self-assembly phenomenon in combination with spin-coating leads to evaporation-induced self assembly (EISA). During spin-coating the sol-gel solution containing the silica species as well as the template are deposited on a substrate, which is subsequently spun. Thereupon, the solution is pushed radially outward from the center and a consistent forced convection is induced within the vapor layer above the substrate, resulting in a uniform evaporation of the solvent.[18] This leads to the increase of the surfactant concentration towards structural mesophases, which act as a template for the silicon oxide network as it condenses around the mesophase.[20, 23, 28] After the template is removed, either by chemical or physical treatment, a mesoporous oxide network is left.[28, 29] This process (shown in Figure 2.11) together with the ratio of ethanol/water/surfactant and properties of the surfactant allows for tuning of the pore size and film thickness.[23, 30]

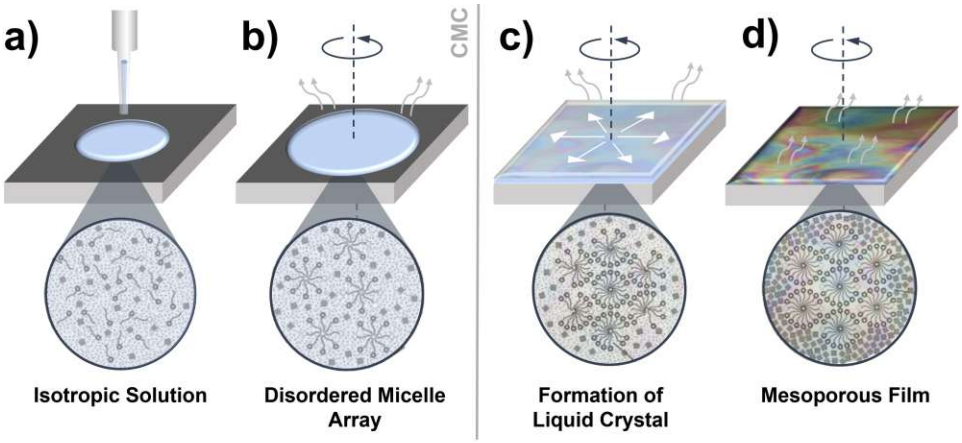

Figure 2.11.: Spin coating procedure. (a) The sol is pipetted on the surface, (b) the surface is spun and EISA starts, (c) the centripetal force pushes the sol outward, coating the surface, (d) an ordered mesoporous silica film is left on the surface. Adapted from[31]

2.2.3. Functionalization of Mesoporous Silica

One major advantage of mesoporous silica is their versatile surface chemistry. Because of the free silanol groups present on the surface, it is fairly easy to change the surface chemistry through functionalization, and thus, the molecules the surface is attracted to as well. Modification of silica surfaces is crucial for optimizing their performance in specific tasks, e.g. the adsorption of proteins. Various strategies have been explored to achieve this, including post-synthesis grafting and co-condensation methods.[32–34]

The co-condensation method, where the functionalization reagent is added during the sol synthesis, allows for more homogeneous distribution of organic groups throughout the inner pore surfaces of nanoparticles without pore blockage or shrinkage issues. Nonetheless, increasing concentrations of reagents may lead to decreased mesoscopic order of the products. On the other hand, post-synthesis grafting involves the addition of organic functionalities onto the silica surface after the initial synthesis and removal of the template. Although this method often results in uneven distribution of functional groups, with a preference for the exterior surface or mesopore openings due to kinetic accessibility, the possibility to calcine the silica beforehand and retaining the functionality as well as the highly ordered final product make it an appealing approach.[33–35]

Different reagents can be used for achieving the desired functionalization. Typically, a condensation reaction between trialkoxysilanes, trichlorosilanes or silazanes with the surface silanol groups is facilitated.[33, 35] Examples of favored reagents are (3-aminopropyl)triethoxysilane (APTES)[32], (3-chloropropyl)triethoxysilane (CPTES)[36] and hexamethyldisilazane (HMDS)[37], although there is a large palette of silanols that can be used to fit the purpose. HMDS (which was used in this thesis) introduces methyl groups onto the surface, changing its character from hydrophilic to hydrophobic.[37] The reaction between HMDS and terminal silanol groups is shown in Figure 2.12 and a schematic depiction of the methylation of the mesopores can be seen in Figure 2.13.

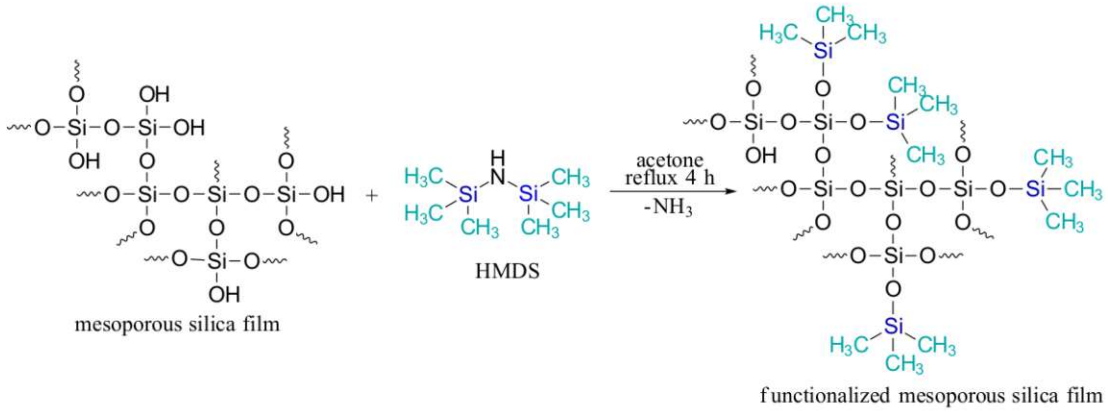

Figure 2.12.: Post-functionalization reaction of the mesoporous silica surface with HMDS.

The functionalization of silica allows for better control of the interaction between the mesoporous surface and the chemicals it comes into contact with, be it the solvent, the product of a reaction or the analyte itself. This poses a great advantage when working with different reaction systems, since optimization of the surface is possible.

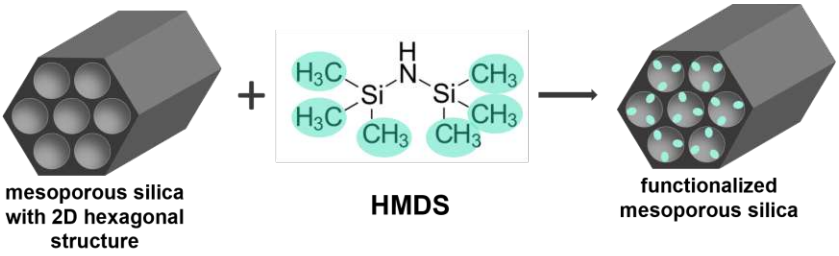

Figure 2.13.: Schematic visualization of the post-synthetic methylation of the silica mesopores.

2.3. Enzymatic Reactions

Enzymatic reactions are reactions facilitated by bio-molecules called enzymes. These are typically proteins that act as catalysts in biochemical reactions. They accelerate the rate of these reactions by lowering the activation energy required for the reaction to occur, thereby making the reactions proceed much faster than they would without the enzyme. Enzymes are essential for life as they regulate the chemical reactions of living organisms. They specifically interact with substances, called substrates, to catalyze particular reactions. By utilizing various intermolecular forces, they are able to combine substrates in an optimal orientation, and therefore facilitate dissolution and formation of chemical bonds. During the reaction, they selectively stabilizes specific transition states, thereby steering the reaction. Herein lies one of their most important characteristics: selectivity. The recognition of only particular substrates as partners for a specific reaction makes enzymes especially attractive catalysts.[38, 39]

Typically, enzymes are comprised of two entities, the main part, called apo-enzyme and a small molecule, called co-factor, which together form what is known as holoenzyme. Co-factors play an important role in enzyme activity, as both parts need to work together for the enzyme to function properly. Based on the reactions they catalyze, enzymes are classified into six groups: oxidoreductases, transferases, hydrolases, lyases, isomerases, and ligases.[39, 40]

Enzyme Kinetics

Enzyme kinetics is the study of the rates at which enzymes catalyze chemical reactions. It focuses on understanding how factors such as substrate concentration, enzyme concentration, temperature, and pH affect the rate of enzyme-catalyzed reactions. The Michaelis-Menten equation is a fundamental concept in enzyme kinetics, describing the relationship between substrate concentration and reaction rate through two kinetic parameters K_m and

v_{max}.[39, 41–43]

Michaelis-Menten kinetics are based on the concept of a steady-state system, although they still successfully describe cases outside this state. An enzymatic reaction goes over a transition state, which is known as the enzyme-substrate complex.

$$\mathrm{E} + \mathrm{S} \underset{k_{-1}}{\overset{k_1}{\rightleftharpoons}} \mathrm{ES} \xrightarrow{k_2} \mathrm{E} + \mathrm{P}$$

The product formation rate, v, is defined by the second (catalytic) step of this reaction:

$$v = \frac{dP}{dt} = -\frac{d[ES]}{dt} = k_2[ES] \tag{2.14}$$

These kinetics are typically determined in the initial stages of the reaction, since during this time the reverse reaction (k_{-2}) is negligible. During steady-state, the dissociation rate of the enzyme-substrate complex to product, k_2, is slow compared to the formation of the complex, k_1, and its dissociation into the precursors, k_{-1}. However, steady-state is defined as the equilibrium where the transition state is formed and consumed with the same rate, $d[ES]/dt = 0$, therefore:[39, 41–43]

$$k_1[E][S] = (k_{-1} + k_2)[ES] \tag{2.15}$$

Equation 2.15 can be rewritten as:

$$[ES] = \frac{k_1}{k_{-1} + k_2}[E][S] \tag{2.16}$$

The three rate constants in this equation can be combined into a single constant, K_m, known as the Michaelis-Menten constant and the equation can be simplified:

$$K_m = \frac{k_{-1} + k_2}{k_1} \tag{2.17}$$

$$[ES] = \frac{[E][S]}{K_m} \tag{2.18}$$

In this case, [E] refers to the concentration of unbound enzyme during the reaction, which is the difference between the initial total concentration of enzyme and the concentration of the enzyme bound into a complex, $[E] = [E]_{total} - [ES]$. With this information, Equation 2.18 can be rewritten as:

$$[ES] = [E]_{total}\frac{[S]}{[S] + K_m} \tag{2.19}$$

Substituting the expression for [ES] in Equation 2.19 into Equation 2.14, Equation 2.20 is obtained:

$$v = k_2[E]_{total}\frac{[S]}{[S] + K_m} \tag{2.20}$$

The maximum reaction rate is achieved when all of the enzymes are bound to substrate, $[E]_{total} = [ES]$. This is under the assumption that the concentration of enzyme is much lower than that of the substrate:

$$v_{max} = k_2[E]_{total} \tag{2.21}$$

Combining Equation 2.21 with Equation 2.20 yields the expression known as the Michaelis-Menten equation:

$$v = v_{max}\frac{[S]}{[S] + K_m} \tag{2.22}$$

This relationship between substrate and reaction rate entails two extreme cases:

1. For $[S] << K_m \Rightarrow v = v_{max}\frac{[S]}{K_m}$, which means the rate is directly proportional to the substrate concentration (Figure 2.14, turquoise shading)

2. For $[S] >> K_m \Rightarrow v = v_{max}$, which means the reaction rate is maximal and independent of the substrate concentration (Figure 2.14, dark blue shading)

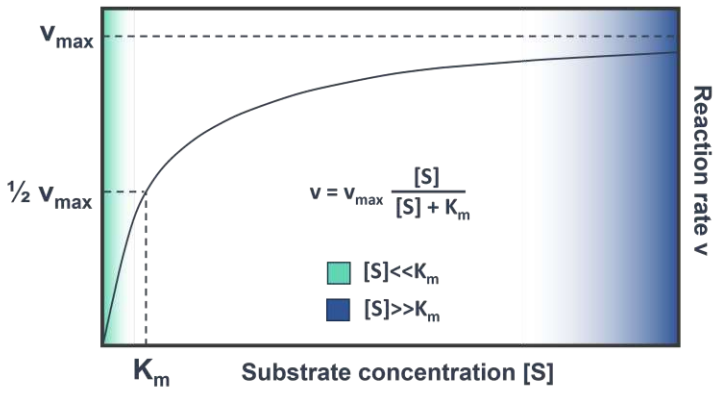

Figure 2.14.: Michaelis-Menten relationship between substrate concentration and reaction rate.

Determination of Substrate Concentration in an Enzymatic Reaction

It is often favourable to quantify a chemical through an enzymatic reaction. There are two distinct pathways to determining the concentration of a chemical, or substrate, for these types of reactions: the "complete conversion" approach and the "kinetic" approach.[44]

For the "complete conversion" method, the reaction catalyzed by the enzyme needs to reach completion, therefore the substrate is fully depleted. This can only be the case, if the product side of the reaction is favoured by the equilibrium. Furthermore, it is of utmost importance for the reaction to progress very rapidly. Hence, it is favourable for the reaction rate to be as close to the maximum, (v_{max}), as possible. This holds true for substrate concentrations $[S] >> K_m$. Additionally, it is beneficial to increase v_{max}, which commands a higher enzyme concentration, but resulting in a higher enzyme activity as well. One way to determine the concentration with this method is by direct measurements. This involves distinguishing substrates from products by their distinct properties, such as absorption spectra. Another path is by employing coupled reactions to further convert the initial product, facilitating quantification. Generally, shifting the equilibrium of the reaction is possible, i.e. by trapping the product, though shifting it to the necessary point for this type of substrate determination method is not always achievable.[44]

On the other hand, the "kinetic" approach relies on the relationship between substrate concentration and reaction rate. A linear dependence between the initial reaction rate and the substrate concentration can be established for $[S] << K_m$, as described above (2.3. sub-chapter "Enzyme Kinetics"). This method suits low substrate concentrations and entails a major time advantage, since the initial reaction rate is determined at the beginning of the reaction.[44]

2.3.1. Lipases

Of interest for this thesis are lipases, which fall unter the group of hydrolases. Specifically they are denoted with EC 3.1.1.3. in the Enzyme Commission (EC) number for systematic classification, where EC 3.1. is reserved for enzymes that act on ester bonds.[45]

Lipases fall under the same classification as esterases. Lipases posses a distinct structural feature that works like a lid, protecting the active site of the enzyme. The lid opens when the lipase comes into contact with a hydrophobic substance. This mechanism is where the distinction between esterases and lipases arises; esterases prefer substrates with shorter acyl chains, while lipases favour more hydrophobic ester substrates with longer acyl chains and are known for catalyzing reactions of triacylgycerides (fats and oils).[45]

Lipases are attractive bio-catalysts, as they mediate a multitude of reactions and are compatible with different substrates, are usually inexpensive, do not require a co-factor for performing a reaction and show high selectivity.[45]

Enzymatic Hydrolysis and Aminolysis Reactions

Lipases are a subgroup of serine hydrolases, which entail the catalytic triad the nucleophilic component serine (Ser), basic component histidine (His), and acidic component aspartic acid (Asp). This triad is an active site that mediates the catalytic acylation. The general catalytic reaction mechanism which is facilitated by lipases is shown in Figure 2.15:[45, 46]

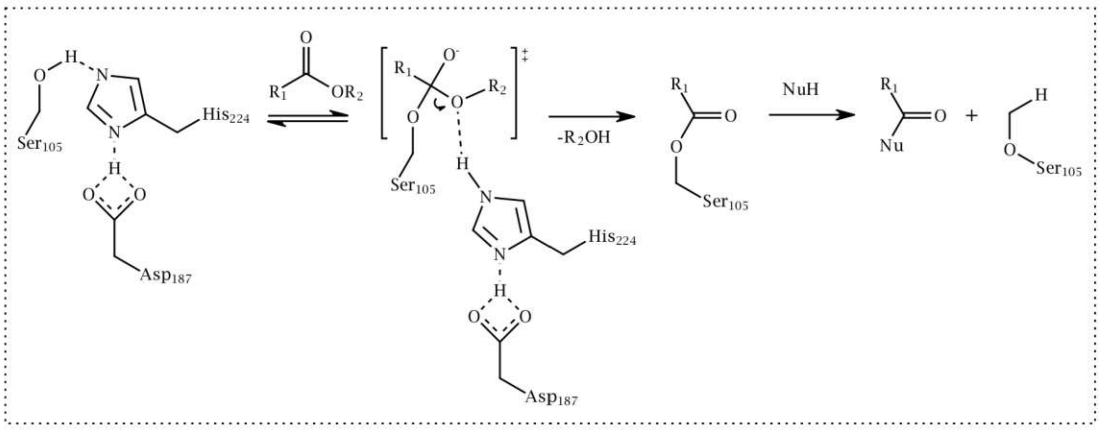

Figure 2.15.: Reaction mechanism of lipase catalyzed reactions depicting the active site of CALB.

The typical substrate for a lipase catalyzed reaction is an ester which is brought to reaction with a nucleophilic reactant. As the substrate enters the active site, it forms a transition state. This transition state disintegrates with the release of an alcohol and formation of a acyl-enzyme intermediate. In a final step, the nucleophile can attack the intermediate, releasing the product. As the primary function of lipases is the hydrolyzation and break down of the ester bonds of lipids, the nucleophile is typically water. The hydrolysis reaction yields fatty acids and glycerine (Figure 2.16 left).[45]

Although their main catalytic reaction is hydrolysis, lipases have been used to catalyze other acylation reactions as well. They are the most commonly used enzyme for N-acylation, also known as aminolysis. In this case, the nucleophile attacking the acyl-enzyme intermediate is an amine molecule. The reaction leads to an amide bond formation and the release of an alcohol (Figure 2.16 right). In order for the aminolysis reaction to take place

instead of the hydrolysis, water needs to be excluded form the reaction. Therefore, dry organic solvents are the medium of choice. Enzymatic aminolysis is highly dependent on the reagents, solvent, and enzyme. Not every combination between these components leads to successful conversion. Hence, it is crucial to choose compatible reagents for a adequate reaction environment.[45, 47]

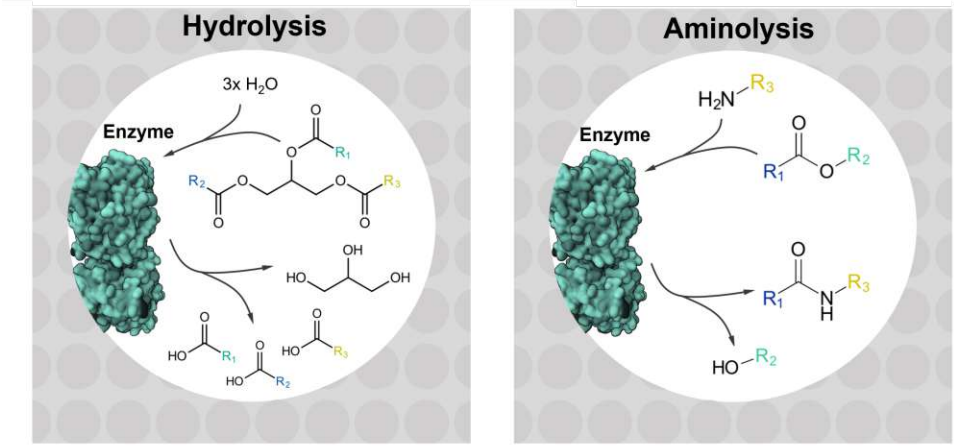

Figure 2.16.: Visualization of enzymatic hydrolysis (left) and aminolysis (right) reactions in a mesopore.

2.4. Introduction to Biosensors

A biosensor is a device that detects and analyzes biological substances by converting a biological response into an electrical, optical, or other measurable signal. Essentially, it is a tool that utilizes biological components, like enzymes, antibodies, or nucleic acids, to interact with a target analyte (a substance being measured) and produces a detectable signal. This signal can then be interpreted to provide information about the presence, concentration, or activity of the target substance. Selectivity is one of the key attributes of biosensors, generating a response only for specific analytes. This selective behaviour stems from both the biological component recognizing the analyte and from the transducer, which is the device that is responsible for converting the recognition event into a measurable signal.[15, 48]

Biosensor technology has seen a great deal of advancement ever since the introduction of the first "real" biosensor from Leland C. Clark Jr. and Champ Lyons for the detection of glucose, which was based on an amperometric enzyme electrode.[49] Biosensors find applications in various fields, including healthcare (for diagnostics, monitoring, and treatment),

environmental monitoring, food safety, contamination determination and biosecurity.[15, 48]

Enzymatic biosensors are a favored method, for one due to the versatile range of enzymes and their possible substrates (analytes), especially those of clinical interest. Because of the nature of enzymatic reactions, parameters such as pH and temperature need to be taken into account during biosensor development. The two main challenges during development are the type of transducer and the immobilization of the enzyme within the biosensor.[15]

2.4.1. Immobilization of Enzymes

As stated above, enzyme immobilization is a crucial process in the development of enzymatic biosensors where the immobilized enzymes must retain their biological activity. Various strategies have been explored for enzyme immobilization, each with its own set of advantages and disadvantages. These include covalent bonding, physical entrapment or encapsulation in a polymeric network, cross-linking, and nonspecific adsorption but no single method or material has emerged as a universal solution. While adsorption strategies offer simplicity, they may result in weaker enzyme binding and stability issues due to enzyme leaching. On the other hand, covalent immobilization, while more stable, often involves more complicated procedures and can lead to reduced enzymatic activity. Traditionally, enzyme immobilization has been mainly limited to polymers, but inorganic substrates such as silica offer advantages including improved mechanical strength as well as chemical and thermal stability.[15, 43]

Immobilization is essential for the reusability of enzymes. Furthermore, efficient enzyme use in non-aqueous media often requires immobilization on a suitable carrier material (matrix) to make the enzyme accessible to the reaction medium. However, the presence of the matrix can influence reaction kinetics, potentially affecting substrate or product concentrations near the immobilized enzyme. The choice of immobilization method and matrix depends on factors such as stability requirements, reusability, and the specific properties of the enzyme and application context.[15, 43, 47]

3. Results and Discussion

The results of the mesoporous silica layer optimization and characterization are shown and discussed in Section 3.1.. In Section 3.2., the outcomes of the tested enzymatic reactions, both hydrolysis and aminolysis, are discussed. After the layer and the enzymatic reaction, lipase enzyme immobilization experiments were performed, the results of which can be found in Section 3.3. Finally, some considerations concerning the final biosensor product are listed in Section 3.4..

3.1. Mesoporous Silica Layer Optimization

The stability of the sol and the formation of a gel network hinges on various system and experimental conditions. Some of these conditions were varied in different mesoporous silica syntheses (see Section 5.2.) to optimize the synthesis for the production of layers with the desired characteristics. The products of all syntheses were characterized to select the best performing silica film.

3.1.1. Considerations Regarding Sampling Depth

Before starting the optimization process, it was necessary to define the optimum outcome for the mesoporous silica layer. Since the mesoporous silica is going to coat an ATR crystal, some considerations regarding the sampling depth were necessary. In general, it was deemed important to keep a correlation between transmission and the ATR measurements. Therefore, the effective depth of penetration, d_e, for the parameters needed for the measurement was set as a reference point. As described in Section 2.1.3., d_e is dependent on the polarization of light. Assuming that the radiation is not polarized, the overall effective depth of penetration is calculated as follows:

$$d_e = \frac{d_{e,s} + d_{e,p}}{2} \tag{3.1}$$

Both $d_{e,s}$ and $d_{e,p}$ are dependent on the wavelength, λ_0, the angle of incidence, θ, and the refractive indices of both the IRE and sample, n_1 and n_2, respectively (according to the relationship described in Section 2.1.3.). Considering that the band of interest

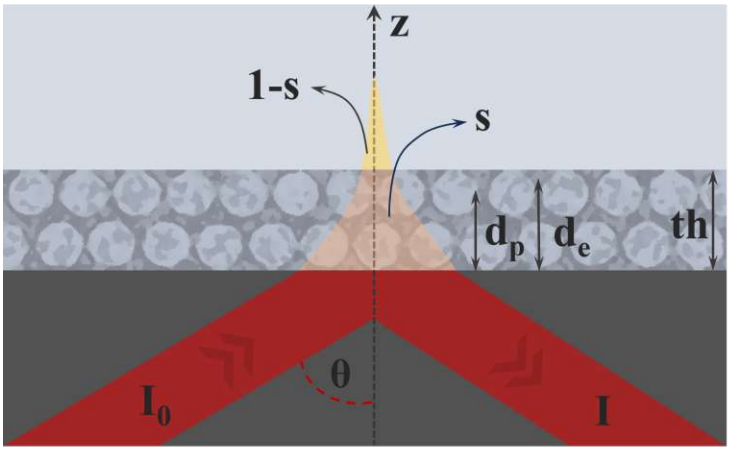

Figure 3.1.: Schematic visualization of the evanescent field within the mesoporous layer and the important parameters related to the incident radiation.

for the evaluation of FAME conversion and therefore for quantification is at 1749 cm^{-1}, the wavelength for calculating the optimum was $\lambda_0 = 5.74\mu m$. The angle of incidence is controlled by the beam defection mirrors and the angle of the polished ATR crystal, both of which are set to an angle of $\theta = 45°$. The refractive index of a Si ATR crystal is $n_1 = 3.4$.[5] The refractive index of the sample, in this case would be the mesoporous silica filled with kerosene ($n = 1.46$[50]). The refractive index of quartz is $n = 1.29$[51] for the wavelength of 5.74 µm. Since the solid part of mesoporous silica is nothing but amorphous silica, an approximation of the refractive index of the layer was performed by taking the average of the refractive indices of kerosene and quartz, resulting in $n_2 = 1.375$. By calculating the effective depth of penetration with these values, d_e is equal to $0.4757\mu m$. The conventional depth of penetration (calculated using Equation 2.9) for these parameters is $d_p = 0.4638\mu m$. Therefore, it was decided to aim for a mesoporous silica layer thickness of around 0.5 µm.

To calculate the fraction of radiation that can interact with the sample in the layer, s, which can be seen as the area of the evanescent wave that lies within the layer, equation 3.2 can be used:[52]

$$s = \frac{\int_0^{th} I(z)dz}{\int_0^{\infty} I(z)dz} = 1 - e^{-\frac{2th}{d_p}} \tag{3.2}$$

$$I(z) = I_0 e^{-\frac{2z}{d_p}} \tag{3.3}$$

with z being the distance form the interface, I_0 the intensity of the incident beam and th

the thickness of the mesoporous layer. With a layer thickness of 0.5 µm, approx. 88 % of the intensity of the evanescent wave is located inside the mesoporous silica ($s = 0.88$).

The reaction system this work is based on uses heptane as a solvent to ensure a matrix similarity to kerosene. The refractive index of heptane is $n_2 = 1.387$. For a single bounce a $d_e = 0.4754\,\mu m$ is obtained, whereas for a multi-bounce ATR crystal with 19 bounces, which is what was used, the effective penetration depth for the whole crystal amounts to $d_e = 19 * 0.4754\,\mu m$=9.0326 µm. The experimental value of d_e was determined to be $d_e = 7.4\,\mu m$ by comparing the intensity of that band at 1749 cm^{-1} of a fatty acid methyl ester measured in a transmission configuration with a path-length of 1 mm and a ATR configuration, using Lambert Beer's law. The values of the theoretical and experimental effective depth of penetration are somewhat in agreement. The discrepancy between the two may have different reasons. For one, the theoretical value is only an approximation. Furthermore, the experimental parameters do not always align with the parameters inserted in the formula for calculating d_e, as internal scattering, among other factors, may lead to less efficiency of the internal reflections.

3.1.2. Synthesis Optimization

As mentioned in Section 3.2.1., it was important for the final mesoporous silica layer to posses a certain thickness. The second point of contention for the layer, arguably the most important point, was the mesopore structure. From the beginning, the use of a surfactant molecule in the synthesis was deemed necessary, as using a templating agent is not only helpful in attaining a more ordered structure, it also steers the diameter of the mesopores to higher values. The conventional surfactant cetrimonium bromide (CTAB) leads to pores with a diameter of around 2 - 3 nm, while a block co-polymer such as Pluronic F-127 can form pores up to 7-12 nm.[28, 53]. Since lipases are relatively big molecules, a bigger pore size was desirable. For this reason, the synthesis variations were mostly performed on the synthesis procedure containing F-127 as a surfactant. For reference, a synthesis with CTAB as surfactant was performed as well (AL01A). The syntheses AL01B-04B follow the same procedure (Section 5.2.2.). AL01B-03B differ from each other in the relative humidity during spin-coating (20-60 %). AL04B has a higher amount of surfactant. AL05B-10B follow a different synthesis work-flow, and differ from each other in their F-127/TEOS molar ratio. Most samples were functionalized after synthesis and calcination. For a detailed description of the syntheses and post-synthetic treatment, refer to Section 5.2..

The samples were characterized *via* small-angle X-ray diffraction (SA-XRD), contact angle measurements, and profilometry. After some initial experiments, some syntheses were

modified to steer the product towards specific attributes. After all samples were characterized with these methods, the best performing one was determined and was then measured by transmission electron microscopy (TEM).

3.1.3. Characterization Results of the Mesoporous Silica Films

Small-Angle X-Ray Diffraction Measurement Results

XRD was performed to estimate the pore size of each of the samples. This was possible due to the ordered mesoporous structure of the layer, facilitated by the templating with a surfactant. As the pores were expected to be in the nanometer range, small-angle XRD was necessary. This method works only as an approximation, since the diffraction happens at the pores, therefore, the d-spacing from the diffractograms gives the distance between the centre of two pores, without taking the wall thickness between the pores into account. SA-XRD was the first step in selecting the most adequate synthesis, since a large pore-size was the most important attribute for the final mesoporous silica film.

As can be seen in Figure 3.2, there is a shift in the reflexes of the three first samples. AL01B, with a relative humidity (RH) of 20 % shows a reflex at a smaller 2θ angle than AL02B with a RH of 40 %. The reflex of AL03B, with a RH of 60 %, appears at the highest 2θ angle. These results are in agreement with previous work from Steinbacher[54]. Based on Bragg's Law:

$$\lambda = 2dsin\theta \tag{3.4}$$

where λ is the wavelength of the incident beam (1.54 Å), d the spacing between two pores and θ the incidence angle, the larger the angle, the smaller the pores. Therefore a trend in pore size based on the relative humidity during the spin-coating process is apparent for this synthesis procedure. This can be explained by the influence RH has on the EISA process during spin-coating. The RH affects the effective evaporation of the solvent, and therefore plays a crucial role during the template assembly and the formation of the pores.

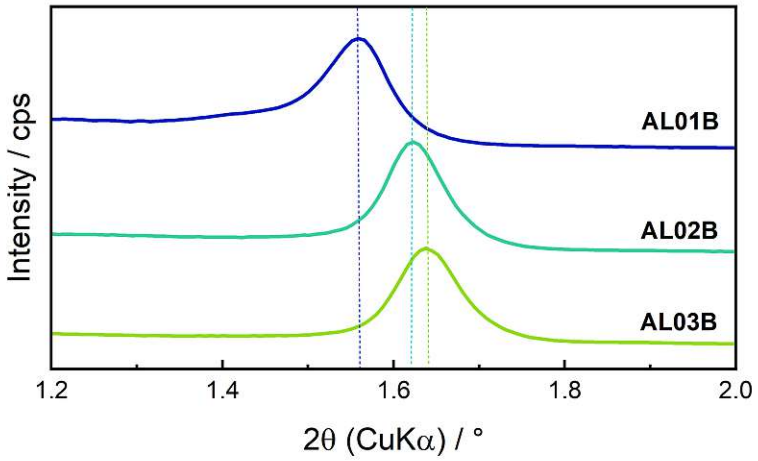

Figure 3.2.: SA-XRD diffractograms of the first three mesoporous silica syntheses with the surfactant F127.

Depicted in Figure 3.3 are the diffractograms of all ten syntheses. From the position of the reflex of each layer, the d-spacing between the pores could be determined using Bragg's equation. The results are shown in Table 3.1. Since the crystallographic orientation responsible for the reflex is not important, as the interest lies only on the pore size, a two dimensional crystallographic network and (100) reflexes were assumed. Based on the d-spacing, the synthesis AL07B had the largest pores, hence it was selected as most the promising. Synthesis AL10B performed the worst, followed by AL01B-03B. A correlation between the F127/TEOS molar ratio and the pore size can be observed. Generally, the syntheses with a higher amount of surfactant resulted in larger pores. The ratios of all syntheses can be found in Section 5.2.2.. AL04B, AL07B, and AL08B had similar F127/TEOS molar ratios and pore sizes. In the end, AL07B was chosen because it had a slightly bigger d-spacing than the other two contenders.

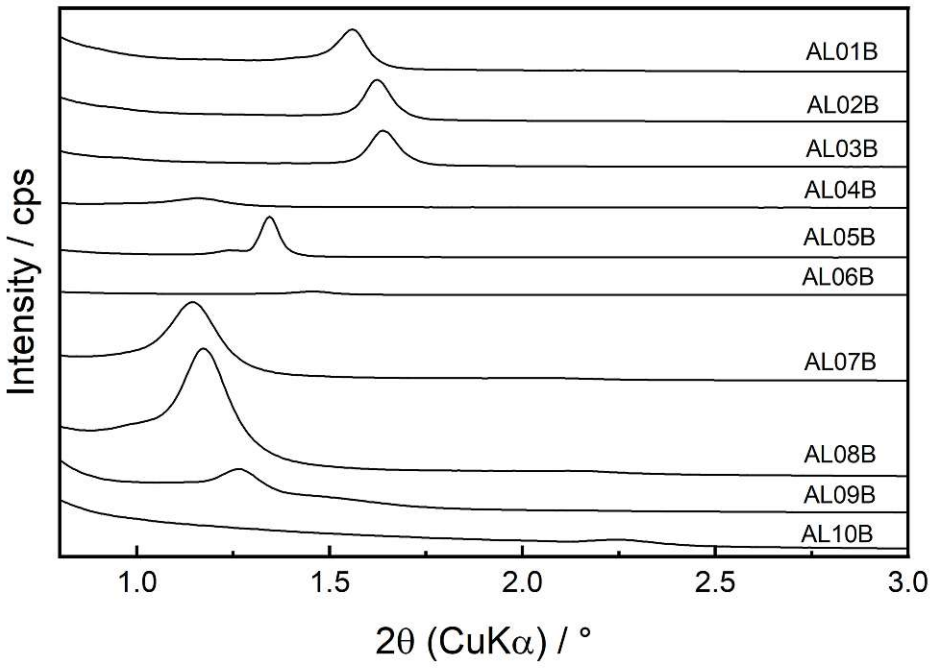

Figure 3.3.: SA-XRD diffractograms of all tested mesoporous silica film syntheses with F127 as a surfactant.

Table 3.1.: The diffraction angle and d-spacing measured for each mesoporous silica layer synthesis.

Synthesis	$2\theta/°$	d-spacing / nm
AL01B	1.558	5.7
AL02B	1.623	5.4
AL03B	1.637	5.4
AL04B	1.164	7.6
AL05B	1.344	6.6
AL06B	1.458	6.0
AL07B	1.143	7.7
AL08B	1.172	7.5
AL09B	1.265	7.0
AL10B	2.246	3.9

For comparison, in Figure 3.4 the diffractograms of both a F-127 and CTAB synthesis are shown. It is apparent that the reflex of the synthesis using CTAB appears at much larger 2θ angles, resulting in a d-spacing of around 3.5 nm. By comparing this value to the values of all ten F-127 syntheses in Table 3.1, it becomes clear that even the worst performing synthesis with F-127 as a surfactant (AL10B) leads to a higher d-spacing value. Since CTAB is a smaller molecule, the micelles and three dimensional structures they form, which the sol uses as a template, are smaller as well. This leads to the final gel structure having smaller pores.

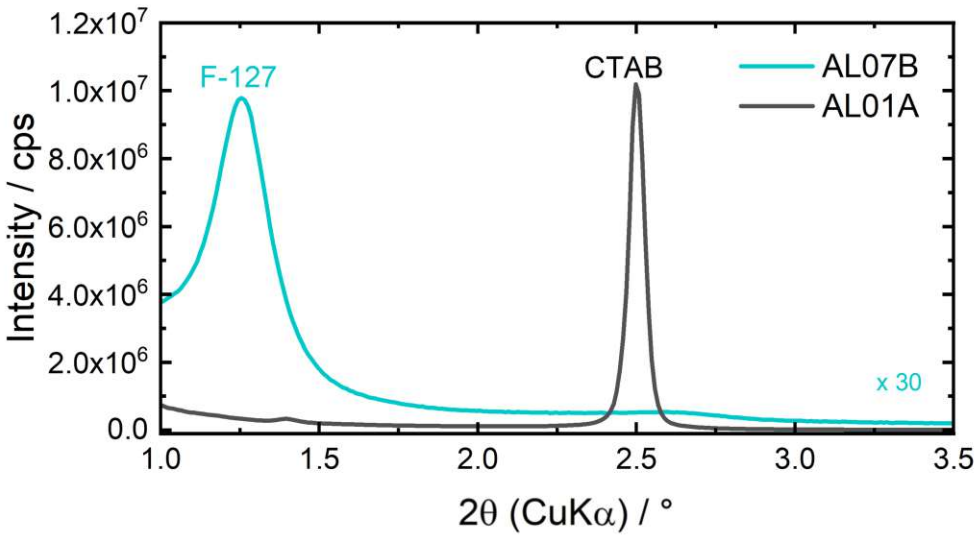

Figure 3.4.: SA-XRD diffractograms of one mesoporous layer synthesized with CTAB and of one synthesized with F127.

To test reproducibility, four films of each synthesis were applied and measured. The results for the chosen AL07B synthesis can be found in Figure 3.5. As can be seen, the four different films from the same synthesis show little variation in the reflex angle and therefore pore size. This was important, since it mitigates the necessity to measure every applied layer to verify the success of the synthesis.

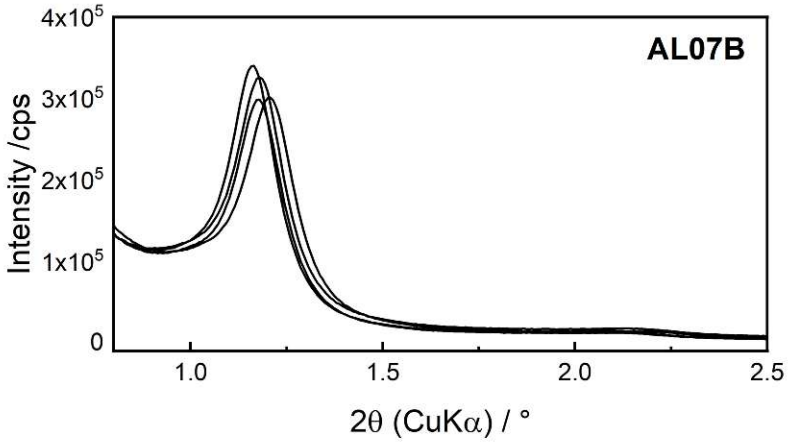

Figure 3.5.: SA-XRD diffractograms of four different AL07B mesoporous silica layers.

After the preliminary selection of the AL07B layers as the most promising, the synthesis was modified slightly. The goal was to vary the thickness of the film, while keeping the pore size relatively constant. This was done by changing the ethanol (EtOH) concentration in the sol solution. The original synthesis (described in Section 5.2.2.) entailed an EtOH:TEOS molar ratio of 16:1. Three other molar ratios were tested, 18:1, 25:1, and 28.5:1. All other parameters of the original synthesis were kept as they were. As evidenced by the diffractograms in Figure 3.6, the pore size was kept decently constant. Compared to the initial AL07B film, the increase in ethanol concentration does not have a significant import on the d-spacing. The d-spacings for all four EtOH/TEOS molar ratios lie in the range between 7.5-7.7 nm.

It is necessary to mention, that although there are reflexes that appear below 1 ° (2θ), they cannot be taken under consideration. As can be seen in Figure 3.7, a blank crystal produces a reflex in this region as well, slightly above the primary beam signal. Furthermore, under 0.6 °, the primary beam undergoes total reflection, which can cause the appearance of reflex-like structures in this region. Coincidentally, this is the region where the reflexes of the desired pore size would present (0.6 °=14.7 nm), which would not be able to be evaluated with certainty. For this reason, to verify the estimated pore-size and also see if there is a potentially bimodal behaviour (more than one pore size), transmission electron

(TEM) microscopy measurements were performed.

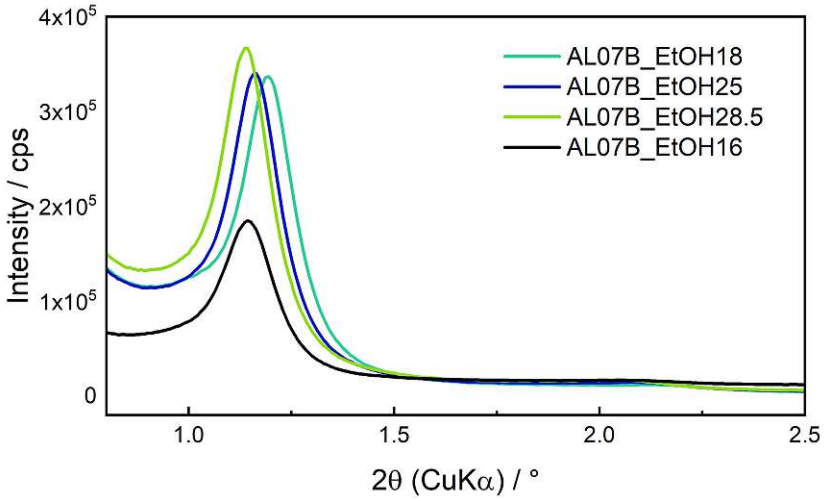

Figure 3.6.: SA-XED diffractograms of four mesoporous silica layers differing in the ethanol concentration during the synthesis.

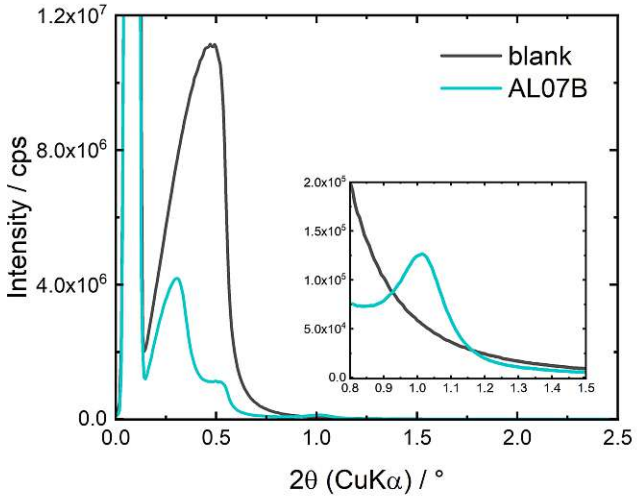

Figure 3.7.: SA-XRD diffractograms of a blank (un-coated) silicon wafer and the AL07B mesoporous silica layer.

Transmission Electron Microscopy Measurement Results

As XRD measurements could only be used for the estimation of the pore size, TEM was needed for confirmation. Therefore, a film of AL07B synthesis was measured. The TEM images of the layer are shown in Figure 3.8. Based on the images, the structure does not seem highly ordered, though a certain order exists, as evidenced by the previous XRD measurements. Further, a parallel orientation of the pores related to the surface can be observed, as is typical for surfactant templated and spin-coated mesoporous silica.[55] Additionally, the pores seem to have a cylindrical tunnel form with a certain uniform diameter. As the pores are not randomly orientated because of the templating, the sample cutting is important. Therefore, cuts in different directions can reveal different aspects of the sample. In this case, the cut seems to have revealed a more horizontal view of the cylindrical tunnels, left behind after surfactant removal.

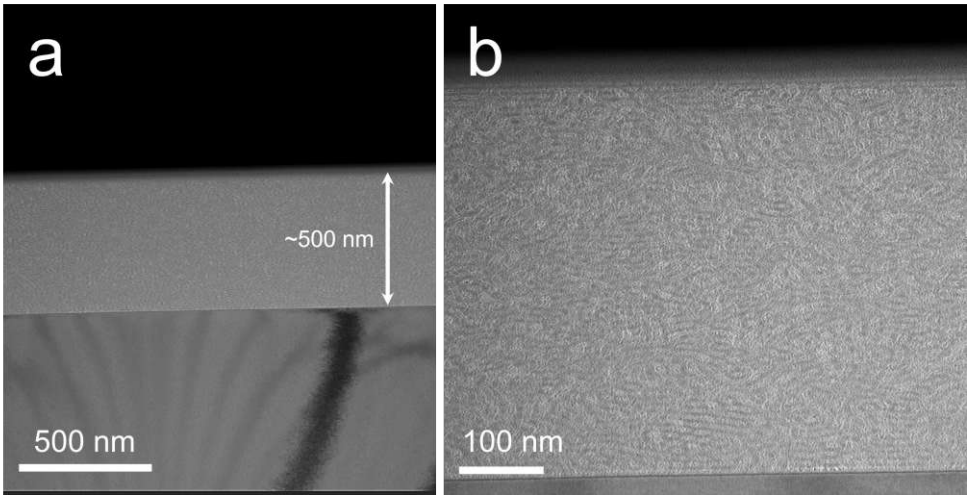

Figure 3.8.: (a) A TEM image of the AL07B_z_y2_25 mesoporous silica layer on top of a silicon wafer. (b) A close-up of the layer, showing the mesopores in dark gray.

In Figure 3.9-b, the Fourier transformation of the highlighted area in Figure 3.9-a can be seen. This shows the electron diffraction pattern of the area. Here, again, an ordered pattern of the structure can be made out, similarly to the XRD results. The diffraction ring shape shows that the pore size is different depending on direction, which means the layer has anisotropic properties. From the electron diffraction, the d-spacing was determined to be approx. 9 nm in one direction and 16 nm in the other. This d-spacing represents the distance between the middle of two tunnels. A less intense ring can also be observed which equates to a d-spacing of around 4 nm in one direction and 8 nm in the other. These

smaller, less ordered pores may be the ones connecting the bigger pores with each other. By plotting the gray value along a path in the TEM image, as can be seen in Figure 3.10, the pore size can be assessed. This was done with the program ImageJ. The pores appear darker in the TEM image, therefore have a lower gray value. The path was purposely chosen in such a way, that it goes across a few tunnels to be able to measure the tunnel diameter. The diameter, and thus the pore size, was determined to be approx. 8 nm.

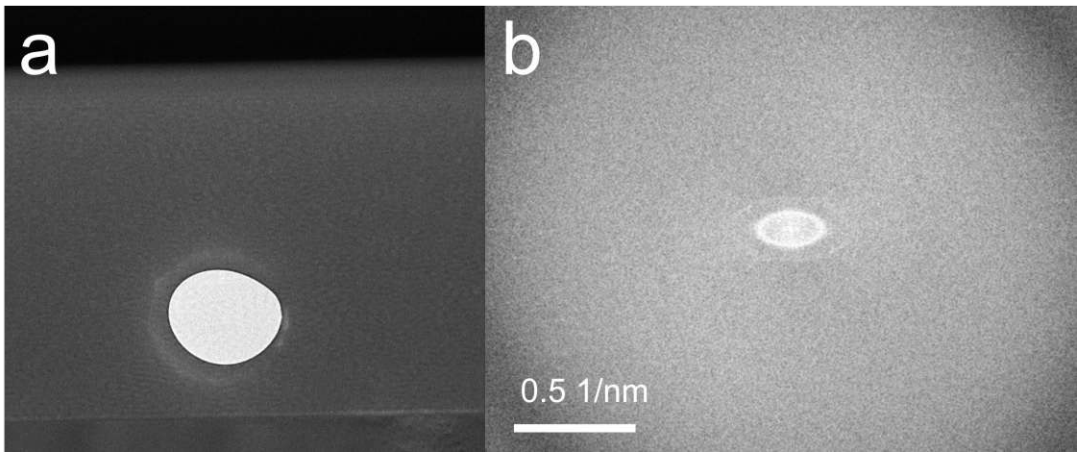

Figure 3.9.: The highlighted section in (a) was Fourier transformed to give the electron diffraction pattern in (b)

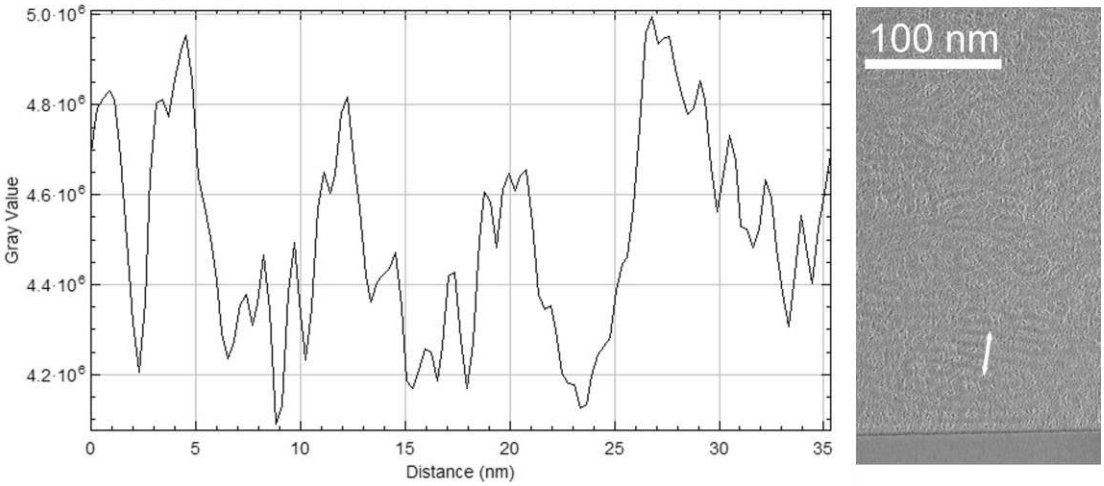

Figure 3.10.: On the left, the gray value of the TEM image plotted against the path shown on the right image.

Profilometry Results

The thickness, which is the second important aspect of the final layer, was measured *via* profilometry. All the results of the measurements can be found in Figure 3.11. After the measurement of the initial ten syntheses with F-127, a correlation between surfactant concentration and layer thickness could be perceived. While AL07B and AL08B had the most promising XRD results, their layer thickness exceeded the desired 500 nm by more than 50 % (AL07B_y2_z and AL08B_y2_z). As discussed above, the EtOH concentration during the synthesis was altered to change the film thickness and keep a relatively constant pore size. A higher EtOH:TEOS molar ratio resulted in a decrease of sample thickness. The samples with an EtOH:TEOS molar ratio of 18:1 were measured to have a layer thickness of around 720 nm (AL07B_y1/y2_z_18), the molar ratio 25:1 lead to a thickness of around 500 nm (AL07B_y1/y2_z_25), and 28.5:1 to 470 nm (AL07B_y1/y2_z_28). Ultimately, the synthesis yielding a thickness of 500 nm was chosen for the coating of the ATR crystal.

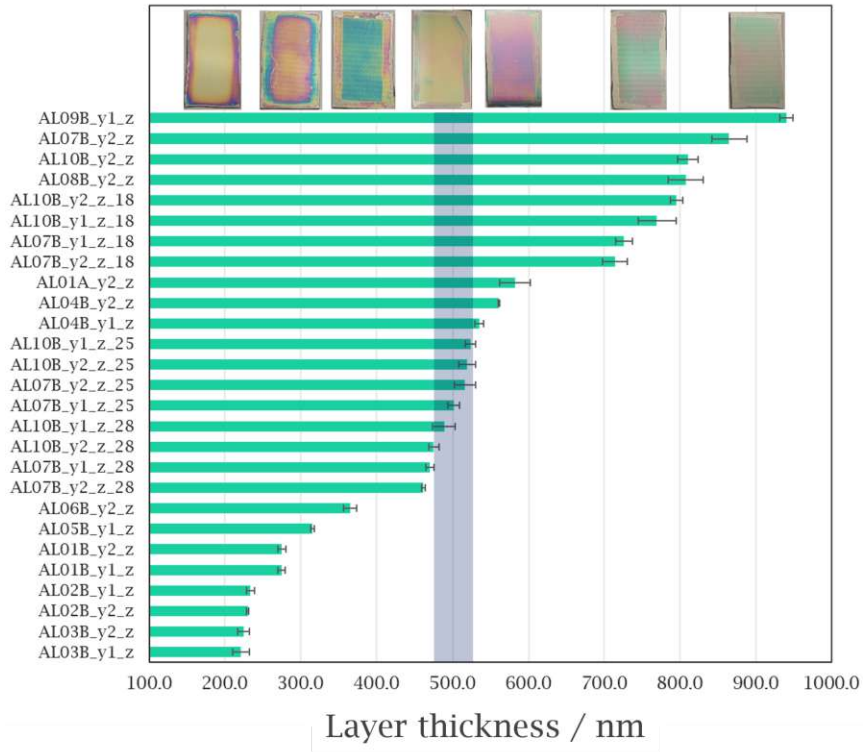

Figure 3.11.: Determined layer thickness for all measured mesoporous silica film syntheses. Pictures of the color difference based on the layer thickness are shown on top.

Contact Angle Measurement Results

Contact angle measurements were performed to verify the success of the post-synthetic functionalization of the mesoporous silica film. Prior to functionalizing, the surface of the mesopores and of the film have a hydrophilic character due to free silanol groups of the silica. Therefore, as is depicted in Figure 3.12-a for a layer of a AL07B synthesis before grafting, the surface is wetted by the water, and the water can enter the pores. After functionalization with hexamethyl disilizane (HMDS), methyl groups are introduced to the surface, turning it hydrophobic. This can be seen in Figure 3.12-b, again, for the AL07B synthesis, now after functionalizing. The contact angle increases, brought about by the surface of the film repulsing the water. This test confirmed the presence of methylated silanol groups on the surface of the silica.

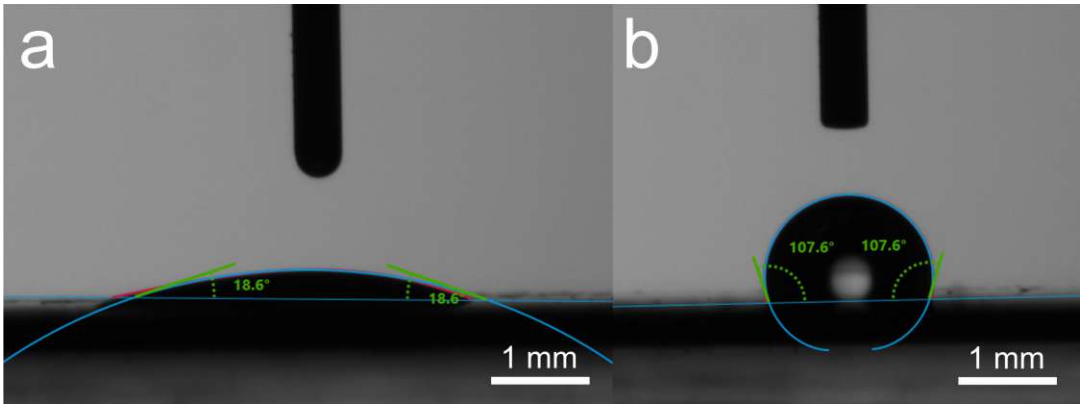

Figure 3.12.: Contact angle of water measured (a) before and (b) after the functionalization of the AL07B mesoporous silica layer

3.1.4. Final ATR-Crystal Mesoporous Silica Layer for Biosensor

As stated previously in this Section, the synthesis AL07B with a modified ethanol to tetraethyl orthosilicate molar ratio of 25:1 was selected for the coating of the ATR crystal. The final reagent molar ratio for the synthesis was TEOS:F127:EtOH:0.1MHCl:H_2O=1:0.0096:25:0.0152:16.29. During spin-coating, a relative humidity of 30 % was held, to hopefully increase the pore size, after determining the correlation between lower humidity and larger pores (Figure 3.2). An XRD diffractogram was measured before the use of the coated crystal (Figure 3.13 left). Based on this diffractogram, a larger d-spacing of 8.7 nm compared to all previous XRD measurements was calculated. A contact angle measurement was performed as well, which is shown in Figure

3.13-right. Both these measurements were undertaken to verify a successful synthesis, but also for later comparison with measurements of the film after use.

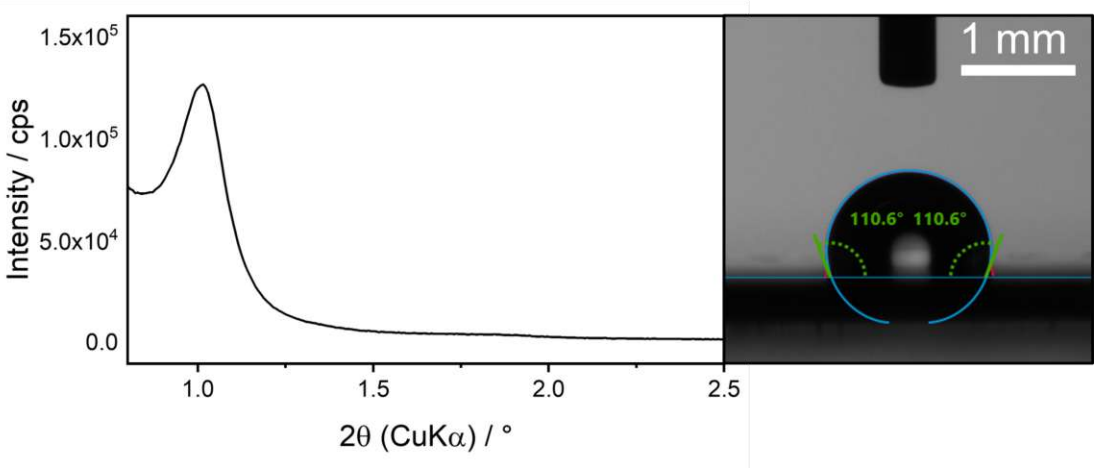

Figure 3.13.: The SA-XRD diffractogram of the final mesoporous silica layer applied onto the ATR crystal (left) and the measured contact angle of the functionalized final mesoporous film (right).

3.2. Enzymatic Reactions

3.2.1. Preliminary Lipase and Amine Selection

Lipases are enzymes that primarily catalyze the hydrolyzation of ester compounds. In the beginning, it was uncertain if all lipases would catalyze an aminolysis reaction, and if so with a high enough conversion. In literature it is stated that the type of lipase, as well as the lipase-amide pairing, are both very important for the conversion during an aminolysis reaction.[45] It was therefore decided to test a few different lipases and amines and find the most suitable pairing. Still, some thought went into the selection. A lipase candidate that stood out during literature research for its continuous good performance in organic solvents and especially for catalyzing aminolysis was *Candida antarctica* Lipase B (CALB).[45, 46, 56, 57] Lipase from *Candida rugosa* (LCR) is one of the most prevalent commercial lipases used in enzymatic catalysis and also shows great promise for catalyzing reactions in organic media.[58]. Since this lipase was also successfully immobilized in mesoporous silica during previous work in this group[54, 59], it was selected for testing as well. Amano Lipase from *Pseudomonas fluorescens* (ALPF) and Amano Lipase A from *Aspergillus niger* (ALA) were also included for the experiments. These lipases were utilized due to their immediate availability and to expand the repertoire of candidates, even

though very little information regarding their successful use in enzymatic aminolysis reactions could be found in literature. Lastly, after conferring with collaborators about similar previous work they had conducted, a lipase with the name Lipex® (LIPEX) was procured and added to the list. The collaborators mentioned one more lipase they had used, which is also mentioned in literature in combination with the aminolysis reaction, which was from *Thermomyces lanuginosus*[47]. In the end, this lipase was not selected because of its inconsistent performance, dependent on the purchased batch.

CALB is a lipase composed of 317 amino acids and a molecular weight of about 30 kDa. Unlike other lipases, CALB does not have a lid that protects the active site, which consists of the catalytic triad Asp_{187}, His_{224}, and Ser_{105}. It is a globular α/β type protein with a size of about 3 nm x 4 nm x 5 nm. Its function is strongly depended on the pH, temperature and solvent and has an isoelectric point (pI) of 6.0.[60–62] This lipase was measured *via* dynamic light scattering (DLS). As can be seen in Figure 3.14, all the measured CALB molecules had a particle diameter <5 nm, with a median of 2.5 nm.

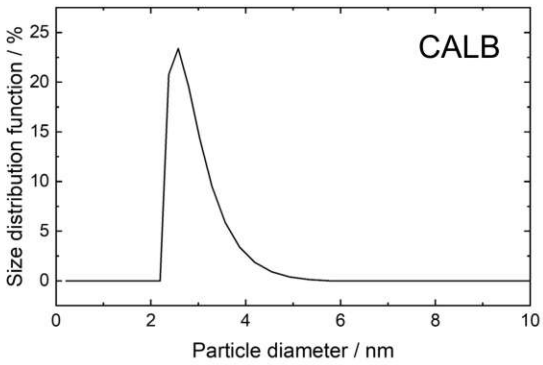

Figure 3.14.: DLS measurement results for CALB.

Candida rugosa has five genes that produce a mixture of isolipases.[58] Commercial LCR lipases almost always consist of a mixure of several of these isoenzymes.[63] Each of the isolipases is composed of 543 amino acids, has a molecular weight of around 60 kDa, and has dimensions of around 5 nm x 4.2 nm x 3 nm.[58, 64] It has a structural lid, typical for lipases, which canopies the active site consisting of Glu_{341}, His_{449}, and Ser_{209}.[58] Depending on which isoenzymes are contained, the pI ranges between 4.5 and 5.5.[65] The optimal catalytic temperature for the lipase is 35-40 °C.[66] The lipases from *Aspergillus niger* and from *Pseudomona fluorescens* have not been characterized, as there are different variations of the lipases. Therefore, it is difficult to find specific properties for these two lipases. LIPEX is a product which consists of one or more unknown lipases. The uncertainty about the nature of the lipase adds to the difficulty of making considerations regarding the

immobilization and reaction itself. Nevertheless, all five lipases shown in Figure 3.15 were tested in ester conversion reactions.

Figure 3.15.: Structure of the lipases used in this work. The enzyme structures were attained from alphafold and PDB. The entry 1TCA[67] was used for the CALB structure, and 1TRH[68] for the LCR structure. Due to the unknown structure of LIPEX, a placeholder was used here for visualization.

When it came to the amine, our collaborators recommended 3-isopropoxypropylamine (3PPA), as this amine worked the best with the LIPEX lipase. It was uncertain though if this amine would also work best with the other selected lipases, therefore three more amines were chosen for the experiments. They were chosen based on structural similarity to 3PPA, commercial availability and price point. Bulky amines were undesirable, since they do not react as readily with the substrate as smaller ones.[45] For this reason, 3-methoxypropylamine (3MPA), 2-methoxyethylamine (2MEA), and 3-(dimethylamino)-1-propylamine (3DAPA) were selected. The structure of each amine can be seen in Figure 3.16.

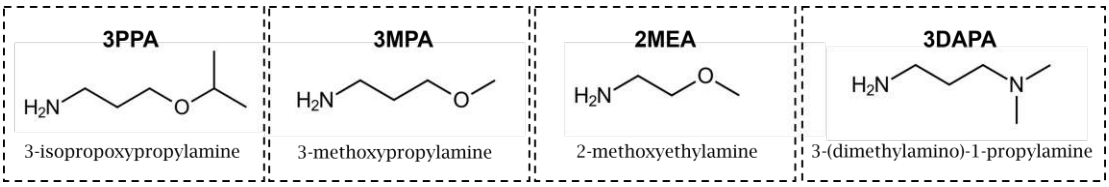

Figure 3.16.: Structural formula and name of the amines used in this work as reactants for the aminolysis reaction

3.2.2. Hydrolysis Reaction

Since lipases primarily catalyze the hydrolysis reaction of esters, it was decided to test the selected lipases in such a reaction. Moreover, once immobilized, the reaction the enzyme should facilitate can be chosen by the user. Therefore, the concept of the final biosensor is not restricted to only the aminolysis reaction. The chosen reaction in this case was the

hydrolysis of triacetin. Triacetin was selected because it is fully miscible with water. The reaction was performed in a 0.1 M phosphate buffer with a pH of 7.5 to ensure the optimal performance of the lipases. The products of this reaction are glycerine and acetic acid (Figure 3.17). All experiments were done in a transmission configuration, since it was only of interest which lipase performs the best.

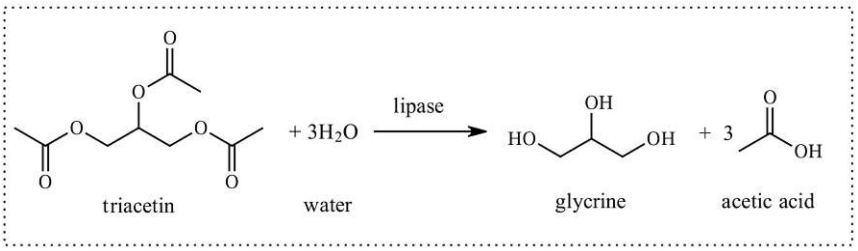

Figure 3.17.: Lipase catalyzed hydrolysis reaction of triacetin to glycerine and acetic acid.

As can be seen in Figure 3.18, multiple changes in absorption bands for the hydrolysis reaction with every lipase occur after 6 h. The band shift comes about mainly due to the depletion of triacetin and the formation of acetic acid. The best performing lipase after 6 h was CALB, followed by ALA and ALPF.

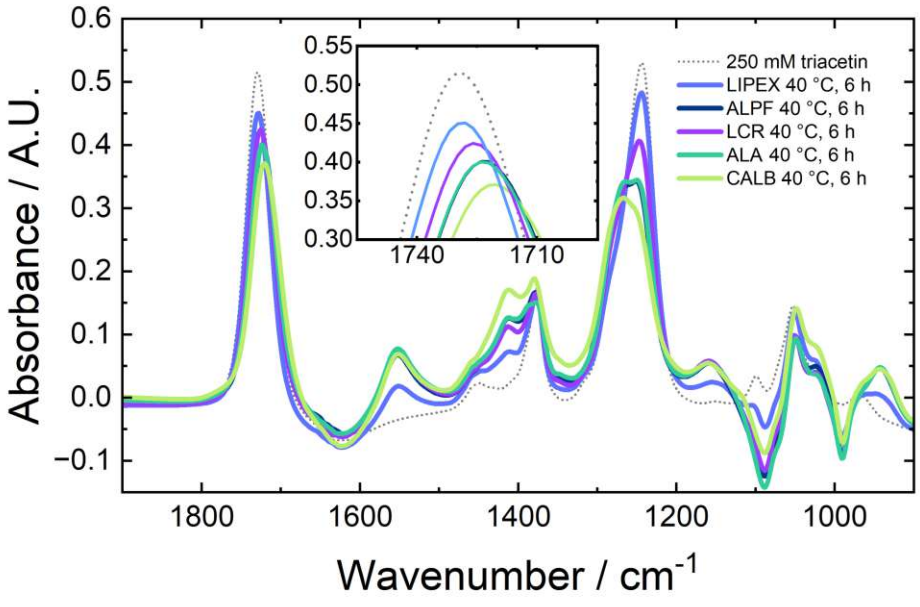

Figure 3.18.: Absorption IR spectra of enzymatic hydrolysis reactions of 250 mM of triacetin catalyzed by five different lipases measured after 6 h reaction time and the spectrum of 250 mM triacetin for comparison.

In Figure 3.19-a, the bands of the reagent and products can be seen. The main bands attributed to triacetin in the shown region are the carbonyl band at 1733 cm^{-1}, the C-O stretches at 1240 cm^{-1} and 1052 cm^{-1}, and the symmetric CH_3 deformation at 1375 cm^{-1}.[69] The most prominent bands of the product, acetic acid, are the carbonyl band at 1712 cm^{-1} and the C-O stretches at 1278 cm^{-1} and 1158 cm^{-1}. Due to the buffer system, the acetic acid is partly deprotonated, therefore, two prominent acetate bands appear as well at 1552 cm^{-1} and 1413 cm^{-1}, which can be attributed to the asymmetric and symmetric COO- stretches, respectively.[70] The dominant glycerine bands in this region appear at 1110 cm^{-1} and 1040 cm^{-1}, for the C-O stretches. As can can be seen in Figure 3.19 a), the reaction solution after 72 h, in this case with CALB as the biocatalyst, displays bands more similar to the two products acetic acid and glycerine. The carbonyl band shifts from 1733 cm^{-1}, attributed to triacetin to 1714 cm^{-1}, as depicted in Figure 3.19-b. The wavenumber does not completely align with the carbonyl band of acetic acid at 1712 cm^{-1}, because the reaction had not reached complete conversion. This fact is also reinforced by the band around 1400 cm^{-1} being an overlap between the CH_3 deformation of triacetin and the COO- stretch of acetate.

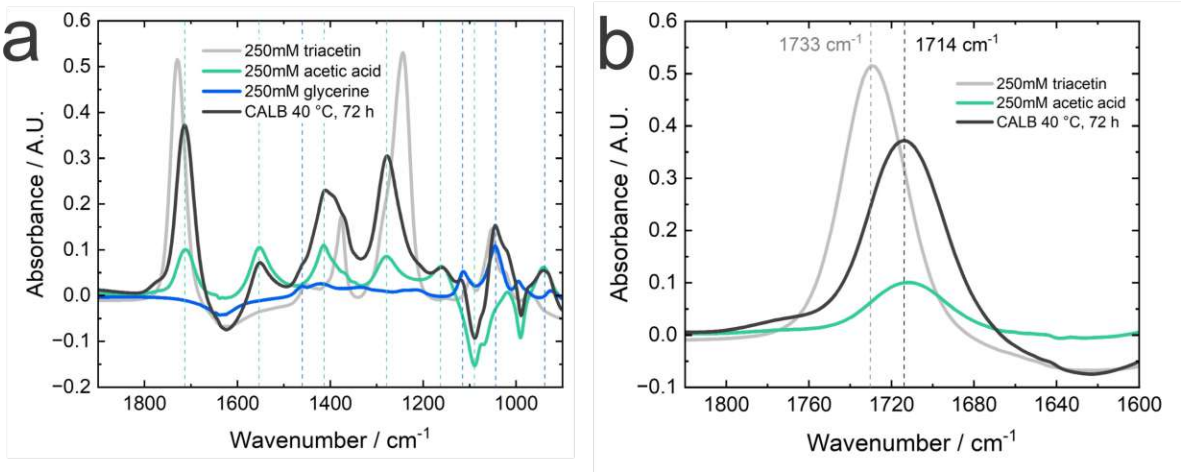

Figure 3.19.: (a) Absorption IR spectra of the reactant and products of the hydrolysis reaction, as well as the measured spectrum of the reaction of 250 mM triacetin catalyzed by CALB after 72 h. (b) Absorption IR spectrum showing the shift of the carbonyl band during the reaction from 1733 cm^{-1} for triacetin towards 1712 cm^{-1} for acetic acid.

All hydrolysis reactions were performed at 20 °C as well as 40 °C, and spectra were taken before the addition of lipase, once after 6 h and again once after 72 h. The temperature plays

a crucial role in chemical reactions, especially for enzymatic reactions.[71] Most enzymes have an optimum working temperature, for example LCR has an ideal working temperature between 35 and 40 °C and for CALB, the reaction works best at 40 °C[66]. Figure 3.20 shows the difference in the final IR absorption spectrum (collected after 72 h) between the two temperatures for the CALB catalyzed reaction. Based on the bands, it was evident that the reaction performed at 20 °C progressed more slowly than the reaction at 40 °C. The carbonyl band of the 40 °C reaction is closer to the product carbonyl band at 1712 cm^{-1}. A similar situation can be observed for the C-O stretch band changing from 1240 cm^{-1} (triacetin) to 1278 cm^{-1} (acetic acid). Due to the temperature optimum of the lipase, this comes as no surprise. A similar behavior was witnessed for all lipases.

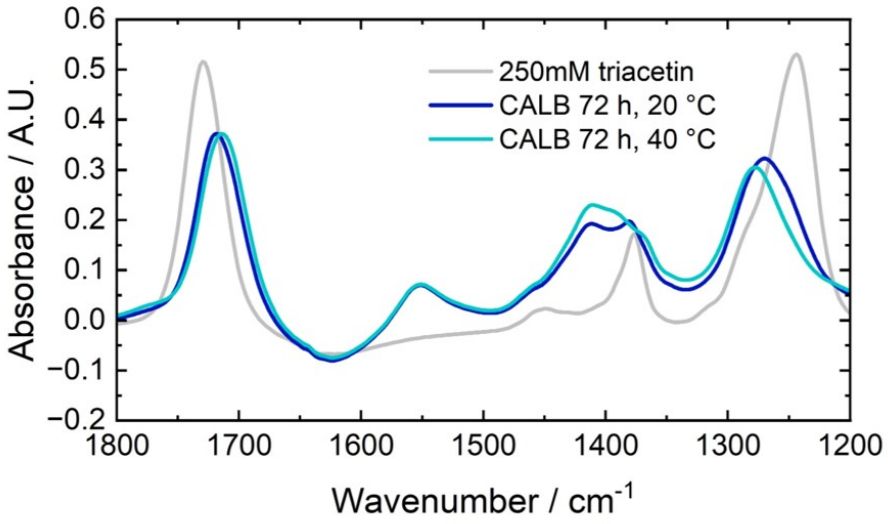

Figure 3.20.: Absorption IR spectra of the hydrolysis reactions of 250 mM triacetin performed at 20 °C (dark blue) and 40 °C (light blue) catalyzed by CALB measured after 72 h and of 250 mM triacetin as a reference (gray).

To quantify the reaction progression and conversion to product, a triacetin external calibration series was measured. The external calibration could have been performed with one of the products of the reaction as well, but since the triacetin bands are not susceptible to pH variations, the C=O stretch band at 1733 cm^{-1} was chosen for evaluation. The linear fit of the carbonyl band can be found in Figure 3.21-a, with a good fit of R^2=0.9978. During the reaction, the concentration of the triacetin continuously decreases while its being converted to acetic acid and glycerine. By the subtraction of the initial pre-reaction IR spectrum from the ones measured at later time points during the reaction, i.e. 6 h or 72 h, respectively, a difference IR spectrum is attained, as seen in Figure 3.21-b. By evaluating

the decrease of the C=O triacetin band with the external calibration and comparison with the initial amount of triacetin, the conversion rate could be calculated. The conversion rates for all performed reactions are summarized in Table 3.2. CALB performs the best in the earlier stages of the reaction, as it has the highest conversion rate for both temperatures after 6 h. ALA performs the best after 72 h at 20 °C but only second best at 40 °C. LIPEX shows the worst performance after 6 h, but has the best overall conversion rate from all reactions at 40 °C after 72 h. CALB seems to have the highest affinity to the substrate, showing high conversion in the initial stages by reaching v_{max} fairly quickly, as opposed to the other lipases. The other lipases, and especially LIPEX, seem to have a higher v_{max}, and once having reached it, show a faster progression of the reaction. Furthermore, as discussed above, all lipases show a higher conversion at 40 °C, both after 6 and 72 h.

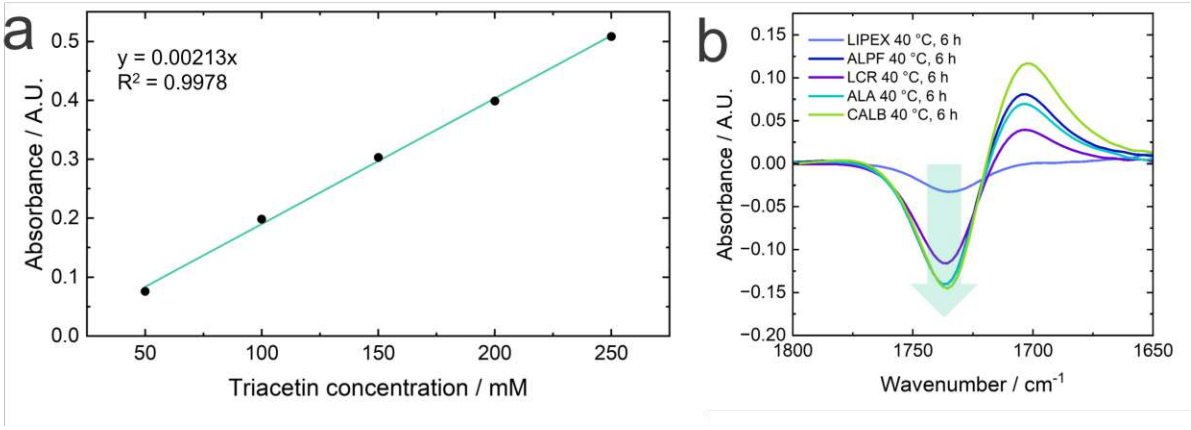

Figure 3.21.: (a) Calibration curve of triacetin for the carbonyl band at 1733 cm^{-1} and (b) Difference absorption IR spectra of the hydrolysis reaction after 72 h catalyzed by the five different lipases. The decrease of the carbonyl band marked with the arrow was used for determining the conversion.

Table 3.2.: Determined coversion of triacetin for all performed hydrolysis reactions.

	20 °C		40 °C	
	6 h	72 h	6 h	72 h
CALB	22 %	34 %	28 %	41 %
ALA	14 %	37 %	25 %	42 %
ALPF	18 %	31 %	26 %	39 %
LIPEX	4 %	31 %	6 %	46 %
LCR	7 %	29 %	22 %	35 %[a]

[a] After 48 h

Michelis Menten Kinetics

A kinetic characterization of two of the better performing lipases, CALB and ALPF, was performed. The conversion, and therefore the enzymatic activity for six different triacetin concentrations was monitored. The initial rate was determined by the decrease of the triacetin carbonyl stretching band at 1733 cm^{-1}. Conversely, the initial rate could also be determined by the increase of one of the product bands, but since the product and therefore its band position is pH dependent, the triacetin CO str. band was selected for evaluation. In Figure 3.22-a and -b, the decrease of the intensity of the carbonyl band over 25 min was plotted for triacetin concentrations between 5 and 250 mM for the ALPF and CALB conversion, respectively. As the kinetics are determined at the beginning of a reaction, while the reverse reaction is still negligible,[43], the initial rate, v, for each concentration was determined by the linear fit of the data between 2 and 4 min ($v = -d[triacetin]/dt$). In a next step, as is depicted in Figure 3.22-c and -d for ALPF and CALB conversion, respectively, the rate was plotted against the triacetin concentration. This data was subsequently modeled by the Michaelis Menten equation (Equation 2.22) and showed good fits (R^2=0.9905 for ALPF and R^2=0.9802 for CALB). The determined Michaelis-Menten constant, K_m was 45.83 mmol L^{-1} for the CALB conversion and 986.28 mmol L^{-1} for the ALPF conversion. The maximum reaction rate, v_{max}, for CALB was 0.857 mmol L^{-1} min^{-1}, whereas for ALPF it was 1.159 mmol L^{-1} min^{-1}. Based on these values, CALB has a higher affinity to this substrate than ALPF, therefore ALPF needs a higher triacetin concentration to reach v_{max}. Although, once the maximal reaction rate is reached, the ALPF conversion is faster due to the higher value of v_{max}, which reinforces previous statements regarding the conversion rate. The K_m value for CALB is comparable to that of LCR for this reaction found in literature (41.8 mmol L^{-1}).[69].

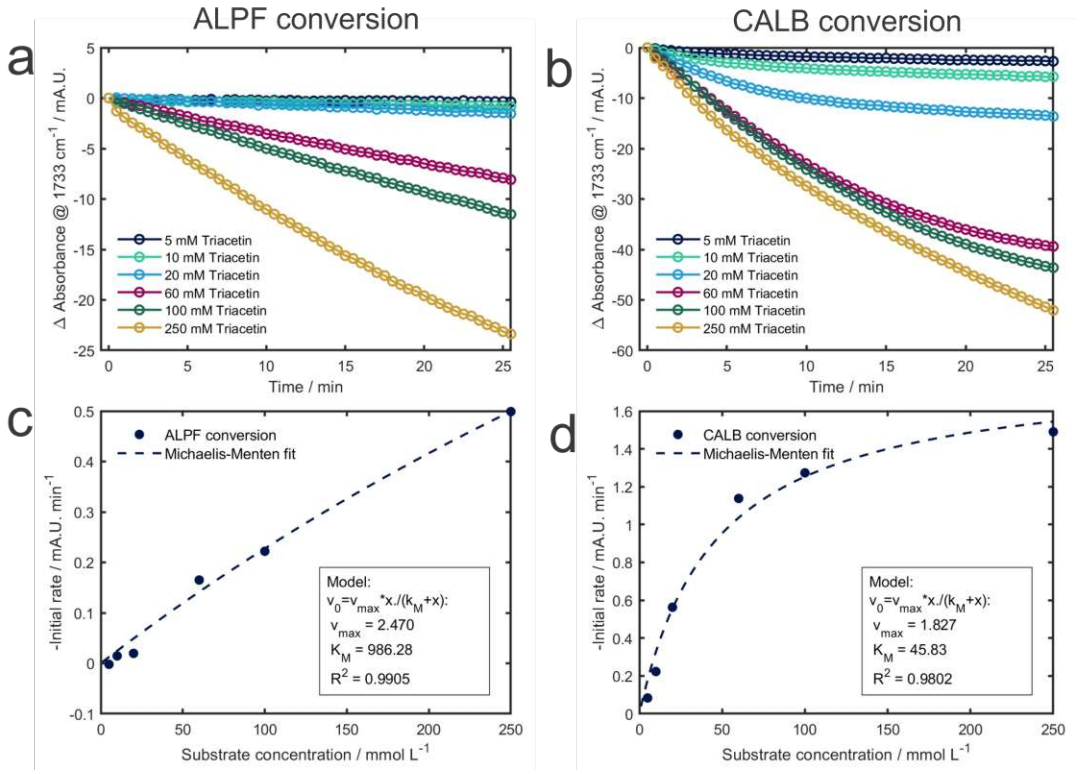

Figure 3.22.: Progression curve of the hydrolysis conversion reaction performed at six different substrate concentrations with (a) ALPF and (b) CALB as substrates. On the bottom the initial rate for each concentration of triacetin coverted with (c) ALPF and (b) CALB is plotted and fitted with the Michaelis-Menten model (dashed line).

For the kinetic tests, the conversion reaction of each substrate concentration catalyzed by CALB was monitored *in-situ*. The changes of the IR absorption spectrum during the course of the reaction for three different triacetin concentrations can be found in Figure 3.23. It is evident in these reaction spectra, in the yellow-marked area, that for the first two concentrations no band in this region appears. The increase in intensity for the band at 1712 cm^{-1}, which is the acetic acid carbonyl streching band, can firstly be observed for the 250 mM triacetin conversion. The reason behind this is the buffer system in which the reaction takes place. As stated above, the buffer is a 0.1 M phosphate buffer with a pH of 7.5. For the 60 mM and 100 mM triacetin conversion, the concentration of the acetic acid product is not high enough to break the buffer system when 25 min pass. After this time, the reaction show a conversion of only 9 % and 14 % for the 60 mM and 100 mM triacetin concetrations, respectively. This equates to 68 mM and 105 mM of acetic acid, respectively, since the ratio of triacetin to acetic acid for the reaction is 1:3. In fact, the

last few spectra of the 100 mM reaction show a minor increase of the carbonyl band, which are the 5 mM of acetic acid above the strength of the phosphate buffer. For the 250 mM triacetin concentration, the conversion rate was 19 %, which produces 140 mM of acetic acid. This is well above the 100 mM of the buffer, thus the carbonyl band of the acetic acid starts to appear. The bands that increase for the 60 mM and 100 mM concentrations are the acetate bands (1552 cm^{-1} asymm. COO- str. and 1413 cm^{-1} symm. COO- str.)[70], characteristic for acetate at pH 7.5. The buffering of the reaction is very important for the performance of the lipase[72], as enzymes have optimal working conditions. For the 100 mM concentration of triacetin after the phosphate buffer system is broken, the correct function of the lipase cannot be guaranteed anymore. This naturally affects the performed reactions for testing the lipases, since a triacetin concentration of 250 mM and a buffer strength of 0.1 M were used. A higher buffer molarity and a lower triacetin concentration would be preferable should the reaction be repeated. As the Michaelis-Menten kinetics were determined with the inital data of each reaction, where the buffer system is still functional, this does not effect these experiments.

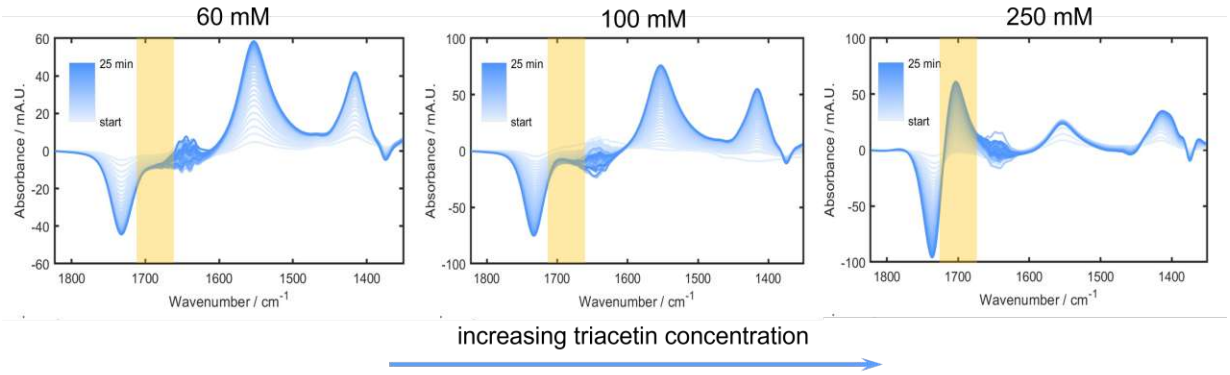

Figure 3.23.: Difference transmission absorption IR spectra taken with a pathlength of 15 µm during *in-situ* monitoring of the hydrolysis reaction catalyzed by CALB for 60, 100 and 250 mM triacetin in a 0.1 M phosphate buffer with a pH of 7.5. The area marked with yellow shows marks the position of the acetic acid carbonyl band.

3.2.3. Aminolysis Reaction

The enzymatic aminolysis reaction is the foundation for the biosensor. Since the biosensor is dependent on a successful conversion of the FAME, it was essential that the reaction was tested and optimized to some extent beforehand. Enzymatic aminolysis entails the reaction between an ester with an amine, facilitated by an enzyme, to produce an amide and an

alcohol. As stated in Section 3.2.1., the combination between amine, ester, enzyme and solvent is crucial for an effective reaction. The ester in this case is predetermined by the goal of the biosensor, the quantification of FAME. The FAME selected for these experiments was methyl myristate (MM). Heptane was chosen as a solvent to mimic the matrix of kerosene, as jet fuel is composed of mainly n-alkenes, although aromatic compounds are present as well.[73] Furthermore, enzymatic aminolysis has successfully been carried out in hexane, which made heptane a promising solvent.[46] It was already mentioned that lipases are known to biocatalyze the amidation of esters[45], therefore, they were selected as the enzymes. Initial tests with ALPF and 3MPA showed no conversion, prompting the used of CALB and LIPEX for further experiments. As the lipase and the amine were the only reactants that were left to optimize, reactions between three different lipases and four different amines were performed. The tested lipases were CALB, LIPEX and LCR, and the amines were 2MEA, 3MPA, 3PPA, and 3DAPA. The main objective was to find the pairing between lipase and amine that works best. Similarly to the hydrolysis experiments, the reaction mixture was measured right at the beginning of the aminolysis (t_0), once after t_1=6 h, and again after t_1=72 h. The mixture was kept at 40 °C for 72 h to give the reaction enough time to show conversion even for the weaker pairings. The IR measurements were done in transmission, as it was more efficient to test the reaction prior to the immobilization of the lipase, especially if one of the lipases ended up not showing any activity towards this reaction.

In Figure 3.24, the IR spectrum of one reaction mixture after three different reaction times can be seen. The pairing in this mixture was 2MEA and CALB. At t_0, in gray, only the reagent bands can be observed, i.e. the FAME and amine bands. In the range between 1650-1800 cm^{-1}, the two most relevant bands for this reaction can be observed. The band at 1749 cm^{-1} can be attributed to the C=O stretch of the methyl myristate, which is a characteristic FAME band. In the lower energy region, the C-O-C asymmetric and symmetric stretch bands of the FAME at 1248 cm^{-1} and 1171 cm^{-1}, respectively, are found. These bands overlap with various 2MEA bands, the C-N stretch and C-O-C asymmetric stretch among others. The broad band at 1620 cm^{-1} can be attributed to the N-H deformation of the amine.[74] A shift in bands can already be observed after 6 h of reaction time. A band at 1694 cm^{-1} starts to emerge, which can be attributed to the C=O stretching vibration of the amide product (N-2-methoxyethyl-tetradecanamide), also known as the amide I band. The amide II band increases in intensity at 1502 cm^{-1}, resulting from the combined N-H bending and C-N stretching vibrations of the amide group.[75, 76] In the lower region, the FAME and 2MEA bands decrease with time, while the reagents are converted to products. Bands in this region attributed to the aliphatic part of the ester remain, as this part is retained in the amide product. Nevertheless, new bands form in this region as well result-

ing from the amide and the alcohol that are produced during the reaction, i.e. the amide III band and the C-O stretch band of the alcohol. The progressive nature of enzymatic aminolysis is evident in Figure 3.24, as the reaction shows a higher conversion after 72 h (turquoise), compared to the 6 h (dark blue). For this pairing (CALB and 2MEA), after 72 h the FAME carbonyl band is nearly completely depleted.

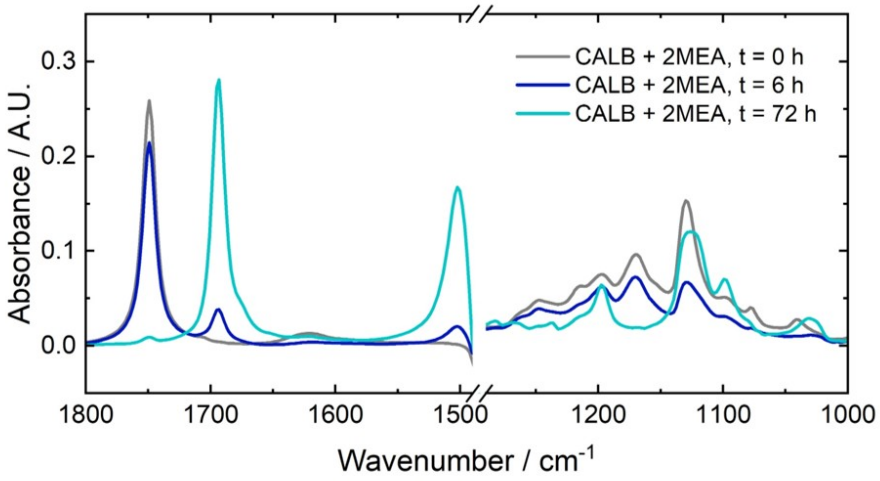

Figure 3.24.: Absorption IR transmission spectra of the aminolysis reaction of 0.08 mmol methyl myristate with 0.24 mmol 2MEA, catalyzed by CALB, measured at t=0 (gray), 6 (dark blue), and, 72 h (light blue), taken with a pathlength of 1 mm. The spectra are cut between 1300 and 1500 cm^{-1} since no valuable information is contained in this region due to the total absorption of the heptane solvent.

For the evaluation of the conversion, the carbonyl band of the FAME at 1749 cm^{-1} was selected. Similar to the hydrolysis reaction, the decrease of this band during the reaction was quantified. The FAME band was chosen because of ease of quantification. Also since FAME is the reactant, a calibration with it can easily be performed. Furthermore, the carbonyl band is a very strong and prominent band that does not overlap with any other bands in this reaction, which simplifies the evaluation. Conversely, the amide I band of the product has comparable characteristics to the carbonyl band of the FAME but the amide products of the reaction between methyl myristate and the four amines are not commercially available. This makes the quantification difficult, as no external calibration is possible.

The difference spectra for all lipase-amine pairings can be found in Figure 3.25. The depicted spectra were attained by subtracting the single channel spectrum at t_0 from the

single channel spectrum at t_1=72 h for each reaction. For the reactions containing CALB and LCR as a lipase, which are depicted in Figure 3.25-a and -c, respectively, there is a symmetry to the decrease of the FAME carbonyl band and the increase of the amide carbonyl band. The same cannot be said for the reactions containing LIPEX (Figure 3.25-b). Here, more FAME appears to be converted than desired product is formed. This suggests the formation of side products during the reaction. Since the interest lies in the quantification of the FAME substrate and not the amide, this does not affect the evaluation. Still, the unknown nature of the lipase and the production of possible side reactions, besides the aminolysis, reduce the appeal of LIPEX for the final selection. Looking at the carbonyl bands of the product, a slight shift of the band depending on the used amine can be observed. This can be related to the steric and resonance effects of the substituents of nitrogen on the C=O bond. The nitrogen atom in an amide has a lone pair of electrons. When a larger group is attached to the nitrogen, it can cause steric hindrance, affecting the bond angles and bond lengths around the nitrogen. This steric hindrance can alter the electronic distribution within the amide group, leading to changes in the C=O bond strength and vibrational frequency. As a result, the C=O stretching frequency (which corresponds to the C=O bond strength) can shift to a different wavenumber. The nature of the substituent attached to the nitrogen also plays a crucial role. Electron-withdrawing groups decrease electron density around the nitrogen, making the C=O bond stronger, which results in an absorption at higher wavenumber. Conversely, the opposite is true for electron-donating substituents.[77] Specifically for the amines used here, depending on the size, alkyl chain length and the position of the heteroatoms on the amine, the carbonyl band appears at a different wavenumber.

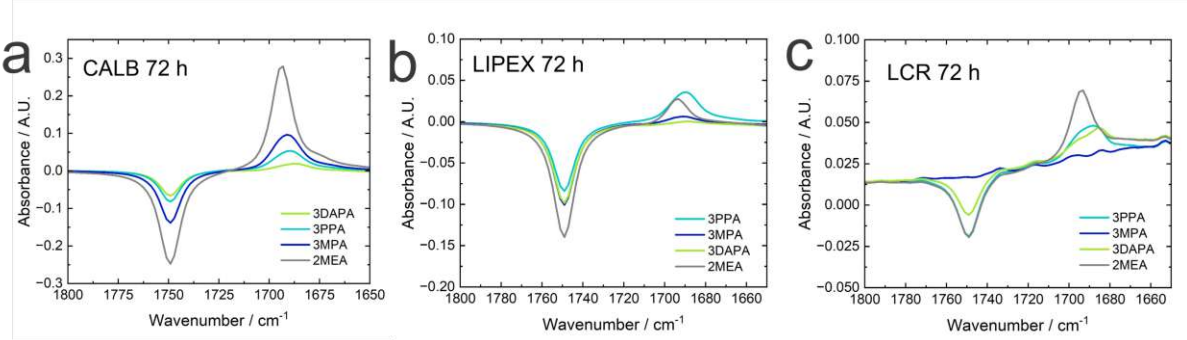

Figure 3.25.: Difference absorption IR spectra between 1650 and 1800 cm^{-1} of all performed aminolysis reaction with 0.08 mmol methyl myristate and 0.24 mmol amine after 72 h at 40 °C, taken with a pathlength of 1 mm. Aminolysis reactions with (a) CALB, (b) LIPEX, and (c) LCR as the biocatalyst.

When looking at the decrease of the band at 1749 cm^{-1} in all three graphs in Figure 3.25, it can be seen that 2MEA (gray difference spectrum) pairs the best with every lipase, since the highest decrease and therefore conversion can be seen for reactions with this amine. Figure 3.26 shows three difference spectra after 72 h, for the reactions containing 2MEA and each catalyzed by one of the three lipases. Based on the spectra, CALB showed the best performance from the lipases with this amine. For this reason, the pairing between CALB and 2MEA was chosen for further investigation.

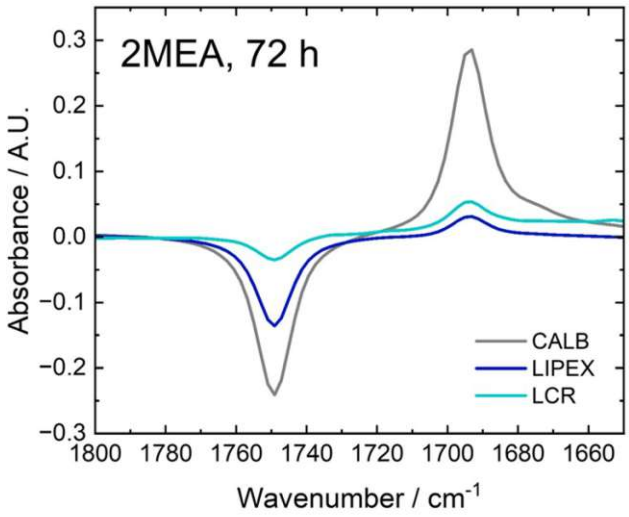

Figure 3.26.: Difference absorption IR transmission spectrum between 1650 and 1800 cm^{-1} of the aminolysis reactions between 0.08 mmol methyl myristate and 0.24 mmol 2MEA facilitated by three different lipases after 72 h at 40 °C. The spectra were taken with a pathlength of 1 mm.

In the context of the consideration of enzyme kinetics in Section 2.3., the influence of lipase concentration on the progression of the reaction was of interest. Thus, two reactions involving MM, CALB, and 2MEA in heptane were conducted under identical conditions, differing only in the concentration of CALB. In one reaction, 0.7 mmol of CALB, while in the other, 1.4 mmol were added to the 20 mL reaction mixtures. Both reaction mixtures were measured at the beginning of the reaction and again after 72 h of reaction time at 40 °C. In Figure 3.27 the results of these measurements can be found. The difference spectrum in Figure 3.27-b, shows a bigger decrease of the FAME carbonyl band for the reaction performed with 500 µL compared 250 µL, a clear indication for a higher conversion for the same reaction time. These results were expected due to the influence of the enzyme concentration on the reaction rate of the enzymatic reaction. Looking at Equation 2.21,

it becomes evident that v_{max} is dependent on the amount of available lipase. Therefore, the mixture with the higher lipase concentration has a higher maximal rate during the reaction, which in turn leads to a higher conversion within the same time frame compared to a lower concentration of lipase.

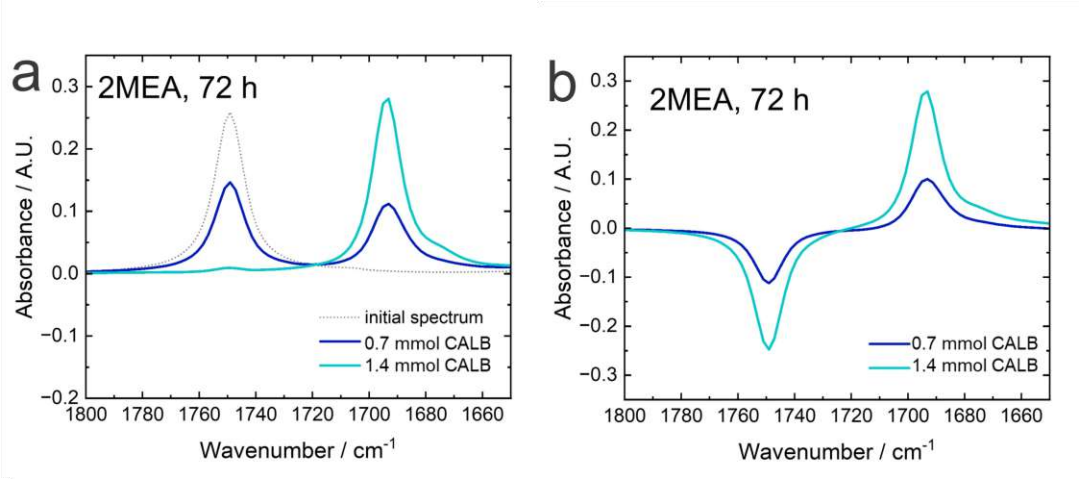

Figure 3.27.: (a) Absorption IR transmission spectrum between 1650 and 1800 cm^{-1} of the aminolysis reaction with 0.08 mmol methyl myristate, 0.24 mmol 2MEA after 72 h at 40 °C with two different concentrations of CALB, and the initial absorption spectrum of the reaction as a reference. (b) Difference absorption IR spectrum between 1650 and 1800 cm^{-1} of the same two reactions depicted in (a). Spectra were taken with a pathlength of 1 mm.

Biodiesel is generally a mixture of different fatty acid methyl esters (FAME), attained from animal fats and vegetable oils. In Europe rapeseed and canola oil are typically used for the production of biodiesel, whereas in the USA soybean oil and animal fats are utilized.[78] Therefore, biodiesel in Europe is generally composed of C16:0, C18:0, C18:1, C18:2 and C18:2 fatty acid esters. Because of the use of animal fats, in the USA C14:0 and C17:0 fatty acids esters end up in the biodiesel as well.[79, 80] Methyl myristate is the methyl ester of myristic acid C14:0. Since this FAME is not prevalent in the European biodiesel, the conversion of two other methyl esters of more common fatty acids was tested for comparison. The procured FAME for the reaction were methyl palmitate (MP), from palmitic acid C16:0, and methyl stearate (MS), from stearic acid C18:0. Figure 3.28 shows the difference spectra of the reactions with the three different FAME under otherwise identical conditions (2MEA, CALB, 72 h, 40 °C). There are no major differences in the depletion of FAME during the reaction, evidenced by the similar decrease of the FAME carbonyl band. The increase of the amide I band of the product is not as similar, which

implies the formation of side products. Nevertheless, the aminolysis reaction is successful for the tested three FAME, all of which are components of biodiesel.

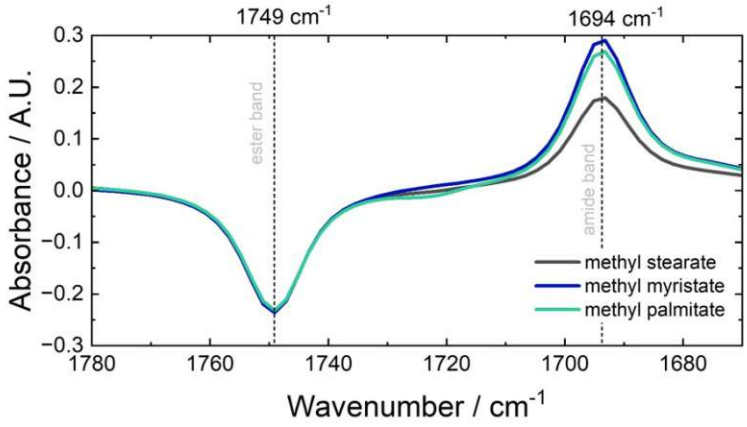

Figure 3.28.: Difference absorption IR transmission spectrum showing the ester and amide carbonyl bands of three aminolysis reactions after 72 h at 40 °C with 0.08 mmol methyl myristate, methyl stearate, and methyl palmitate. The spectra were taken with a pathlength of 1 mm.

Analogously to the hydrolysis reactions, the decrease of the main FAME IR band at 1749 cm^{-1} was used for determining the conversion during the reaction. Because of the use of three different FAME, MM, MP, and MS, three external calibrations were performed. The linear fit for each FAME can be found in Figure 3.29-) to -c. The results for the conversion of all conducted reactions are summarized in Table 3.3.

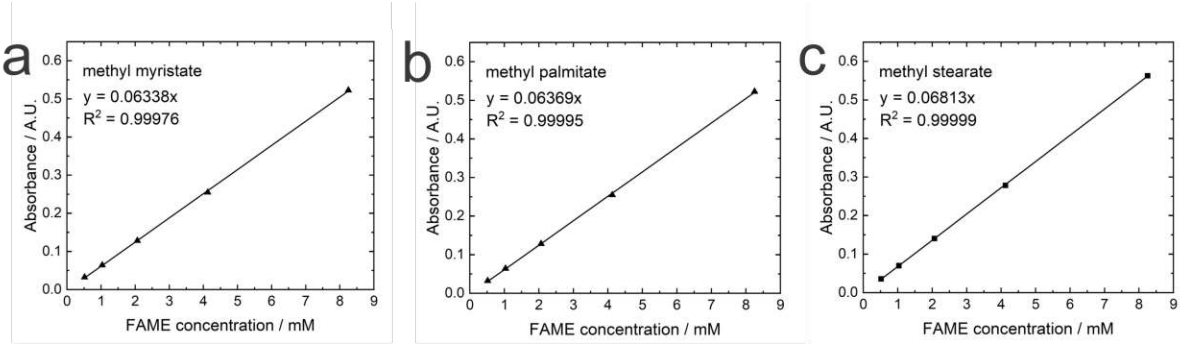

Figure 3.29.: Calibration curve of the carbonyl band at 1749 cm^{-1} for each used FAME substrate, (a) methyl myrsitate, (b) methyl palmitate, and (c) methyl stearate

The reactions with 2MEA and CALB show the highest conversion after 72 h, the highest overall being the one with MM with 95 % conversion, followed by MS with 89 % conversion,

and MP with 84 % conversion. The same pairing of 2MEA and CALB had a significantly higher conversion after 6 h with 15 %, compared to all other pairings, which all had a conversion of <3 %. In general, CALB was the lipase that performed best, followed by LIPEX. LCR showed the worst performance and also being part of the only pairing that showed no conversion at all (with 2MPA). 2MEA was the best reagent for all lipases as well, though, as previously stated, its pairing with CALB is by far the best. Even after only 6 h, this pairing had the same FAME conversion as LCR+MEA after 72 h, which was the best pairing for LCR. The conversion of the reaction with 250 µL CALB and 2MEA was 52 %, which is about half of the 95 % for the full 500 µL.

Table 3.3.: Conversion values of all performed reactions for 6 and 72 h.

FAME	amine	lipase					
		CALB		LIPEX		LCR	
		6 h	72 h	6 h	72 h	6 h	72 h
MM	3PPA	1 %	31 %	1 %	32 %	2 %	15 %
	3MPA	1 %	53 %	1 %	37 %	0 %	0 %
	3DAPA	1 %	25 %	1 %	38 %	1 %	10 %
		15 %	95 %	2 %	53 %	2 %	15 %
MS	MEA	-	89 %	-	-	-	-
MP		-	84 %	-	-	-	-

The comparison of CALB and LIPEX with LCR is not optimal because of the difference in purchased lipase state. Since CALB and LIPEX were procured already dissolved in glycerine and glycerine is not soluble in heptane, the reaction could only take place at the interface between the glycerine and heptane. Furthermore, the concentration of the lipases in glycerine on the specifications of the purchased product was an estimation (approx. 10 %). Furthermore, related to all samples, the reaction mixture was not stirred continuously. Stirring would most likely have had a positive effect on the progression of the reaction, especially for the samples containg CALB and LIPEX, since the interface area between the glycerine and heptane would have been increased.

Important to mention is that a reaction with the 2MEA+CALB pairing was performed at 60 °C as well. Because of the high vapor pressure of heptane, it evaporated fairly quickly and the seal vial was not efficient enough for the heptane vapor to not escape. The sample was measured nevertheless, and as expected, the intensity of the bands was higher than

in the inital spectrum due to the increased concentration of the reagents in heptane. But even with the increased concentration of the product, the intensity of the amine I band was lower than for the reaction conducted at 40 °C, hence, the decision was made to stay at the original temperature of 40 °C.

In-situ Experiment

One reaction was followed in-situ for an hour as well. The sample consisted of MM, LCR and 2MEA in heptane. LCR was selected for this experiment because the sample could be continuously stirred at 40 °C without the danger of phase separation in the transmission cell, as could be the case for the lipase dissolved in glycerine. For these lipases, trying to replicate the experiment did not result in meaningful spectra. Even for LCR, this experiment could only be successfuly performed for one hour, as for longer time periods, the high vapor pressure of heptane and the tendency of the enzyme to clog the tubings led to a decrease in performance. The resulting difference spectra over time for the region of the carbonyl bands of the ester and amide is shown in Figure 3.30. As can be seen in the Figure, after a quick initial conversion, there is a continuous decrease and increase of the ester band and amide band, respectively.

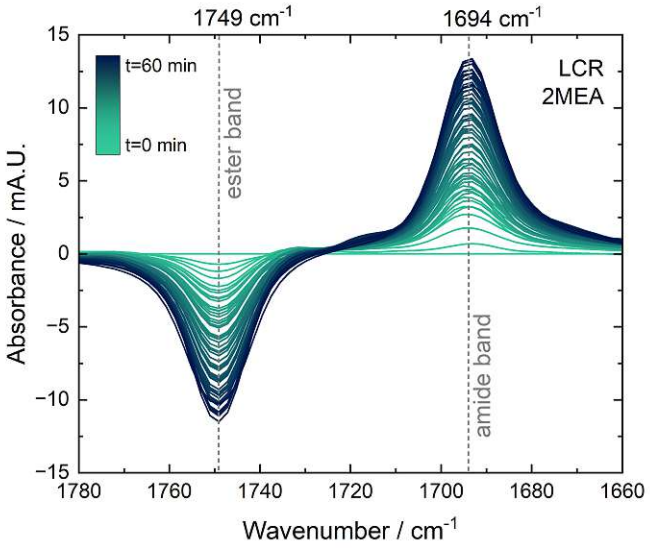

Figure 3.30.: Decrease of the ester (1749 cm^{-1}) and increase of the amide (1694 cm^{-1}) carbonyl band during the *in-situ* monitoring over 60 min of the 0.08 mmol methyl myristate conversion reaction with 0.24 mmol 2MEA, catalyzed by LCR at 40 °C.

From the decrease of the FAME carbonyl band at the beginning stages, the initial rate of the reaction could be determined. The absorbance decrease after each measurement was converted to mmol using the MM external calibration (Figure 3.29-a). The initial rate was determined by calculating the slope of the linear fit between 2 and 4.5 min, as shown in Figure 3.31. Since $v_0 = -d[S]/dt$ for $t \sim 0$ and $dt \to 0$, v_0 was determined to be 0.02017 mmol min^{-1}. This value is easily converted to an enzyme unit by converting the mmol to µmol, resulting in 1 µmol min^{-1}. By inserting this value and the amount of used lipase (50 mg) in Equation 3.5, the specific activity of the lipase could be determined:[44]

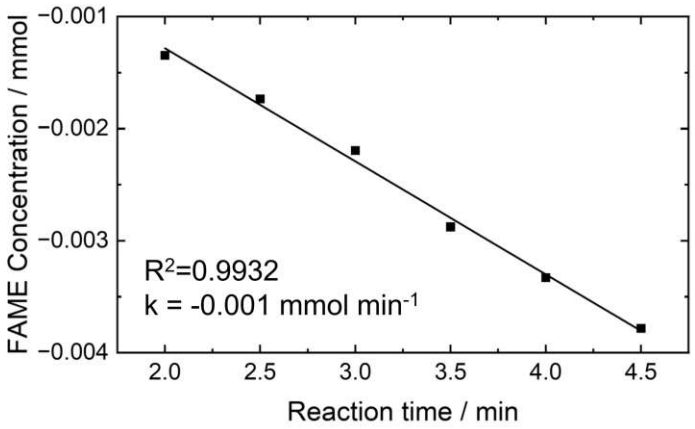

Figure 3.31.: Progression curve of the in-situ enzymatic reaction from 2 to 4.5 min linearly fitted.

$$\text{specific activity} = \frac{\text{µmol substrate converted/min}}{\text{mg enzyme}} \tag{3.5}$$

This resulted in an specific activity for LCR of 0.02 µmol min^{-1} mg^{-1} for the aminolysis reaction of 4 mM methyl myristate and 12 mM of 2-methoxyethylamine in heptane at 40 °C.

3.3. Lipase Immobilization Monitoring

After concluding that CALB was the best performing lipase in the aminolysis reaction, the next step was to immobilize it inside the pores of the mesoporous silica film applied on the ATR crystal. Through immobilization, the biocatalyst becomes reusable, which is of great interest, considering the aim of the coated ATR crystal being multi-use. Immobilization is an attractive option for enzymatic reactions performed in organic solvents, which is the case for aminolysis, since lipases are not soluble in these solvents and the leeching of the lipase

after immobilization is reduced.[81] Based on previous work from Steinbacher[54], ot was decided to use a methylated mesoporous silica film for the immobilization. The reason for using methylated silia is that in unmethylated silica the pH of the lipase solution becomes critically important for the immobilization, since the pI and the PZC govern the net charge and therefore the interaction between the enzyme and the silanol groups. For a desired interaction, the pH needs to be higher than the PZC for the silica to have a net negative charge and lower than the pI of the lipase for it to posses a positive charge. With a PZC for silica of 3.6 and a pI for CALB of 6.0, the pH window that fulfills the requirements is not very large. Further, the activity and stability of the lipase might suffer due to sub-optimal pH conditions. Initial tests from Steinbacher showed no immobilization for unmethylated mesopores, which was the reason for the derivatisation of the silica films with HMDS in this work. It was also stated that the aqueous buffer leads to the degradation of the un-functionalized silica. Methylated silica surfaces, which are hydrophobic, allow for physical adsorption immobilization of the lipase. It is often the preferred choice for immobilization of enzymes, especially lipases, because the properties (i.e. hydrophobicity) of the surface is similar to those of their preferred substrates, lipids. Because of this they undergo interfacial activation during adsorption, which leads to the opening of the lid that protects the active site.[81] This typically increases the activity of the lipase.[82].

The design of the immobilization experiments is outlined in Section 5.6.. Firstly, the lipase was measured on a blank un-coated ATR crystal as a reference. Next, the experiment was performed on a mesoporous silica coated and functionalized ATR crystal. Four concentrations of CALB in phosphate buffer (0.5 M, pH 7.5) were measured over time, starting from the lowest concentration, $1\,\mathrm{mg\,mL^{-1}}$. The time series is shown in Figure 3.32-a. In between every lipase concentration flush, the ATR cell was washed with the buffer solution, to remove any un-adsorbed lipase. The spectra needed to be corrected for water and water vapor due to the presence of tiny air bubbles and water content fluctuations. As the δ(OH) band of water (around $1650\,\mathrm{cm^{-1}}$) also interferes with the amide I band, the intensity of the amide II band of the lipase protein was plotted against the experiment time. As can be seen, the intensity of the band increases over the 50 min during which CALB is flushed through the cell for every measured concentration. The difference between concentrations is how fast the lipase concentrations in the pores increases, thus, how fast the intensity of the amide II band increases. During the buffer flush, the concentration of CALB stays relatively constant, but more importantly it does not decrease. This means the already adsorbed lipase does not desorb upon washing with buffer. The increase of the lipase concentration appears to have a linear behaviour during the 50 min of immobilization. As there is bound to be a maximal loading of the mesoporous silica with lipase, the increase of signal would asymptotically approach the maximal value after a certain amount of time.

This indicates that the loading limit was not close, as the intensity of the amide II band was showing no signs of plateauing. The potential for a higher immobilization can be tapped into through a longer loading time. A higher lipase load could be favorable, since it would increase the enzyme activity, though it might also obstruct the pores, blocking the analyte molecules from entering the deeper parts of the layer.

In Figure 3.32-b, the IR spectral region of the amide I and amide II band of CALB is shown. The amide I band of CALB appears around 1650 cm^{-1} and the amide II band around 1550 cm^{-1}. The intensity of the two bands for each concentration after 50 min of flushing is shown. It can be seen that the intensity and therefore the loading of the lipase increases with each concentration of lipase.

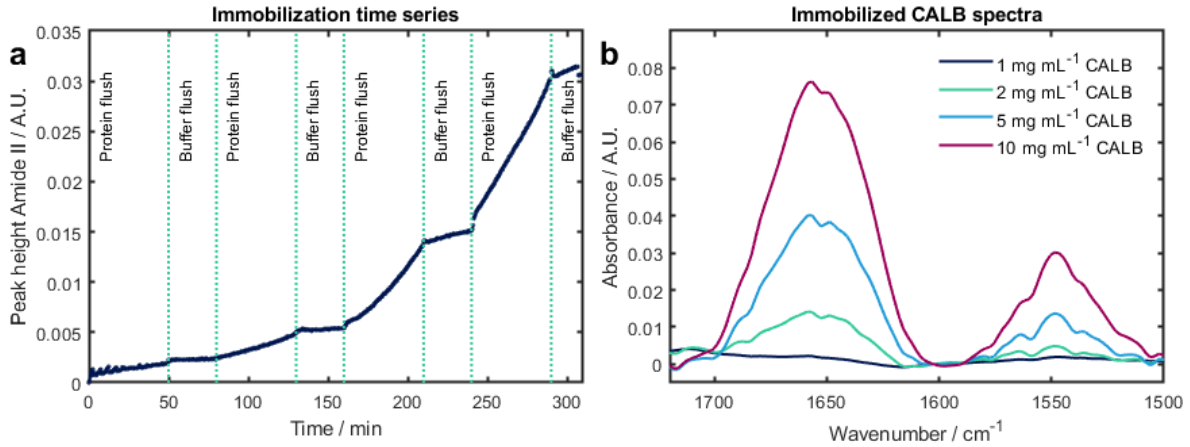

Figure 3.32.: (a) The time series of the CALB immobilization experiment. CALB with 1 $mg\,mL^{-1}$, 2 $mg\,mL^{-1}$, 5 $mg\,mL^{-1}$, and 10 $mg\,mL^{-1}$ in phosphate buffer was measured in increasing concentration. Between each concentration the system was washed with buffer (=buffer flush). The height of the measured amide II band was plotted against the immobilization time. (b) The amide I and amide II band intensity of each measured CALB concentration with the coated ATR crystal before the buffer flush.

To confirm a successful immobilization, it was important to verify if the lipase did in fact get immobilized inside of the pores and was not just adsorbed on top of the mesoporous silica film. For this, the signal intensity of the amide I band of the 10 $mg\,mL^{-1}$ CALB solution measured in the cell with the coated ATR crystal was compared to the signal of the same CALB solution measured with the un-coated crystal (Figure3.33). For the un-coated crystal, the band intensity was 0.01 A.U.. This accounts for 100 % of the evanescent field interacting with the sample. Assuming that the lipase does not get into the pores,

the mesoporous layer would only block 85 % (s) of the evanescent field form interacting (as calculated for a layer of 500 nm in Section 3.1.1., but for the wavelength of 1550 cm^{-1}). If the lipase only was adsorbed on the surface of the layer, the signal would be 15 % (1-s) of the intensity measured for the un-coated crystal, which would be 0.0015 A.U.. The actual intensity that was measured for the coated ATR crystal was 0.032 A.U.. This value is about 20 times higher than the calculated value for the lipase adsorbed only on the surface of the film, which means CALB is not only on top of the mesoporous silica layer, but also inside of the pores. This value would increase with a higher loading, but this proves that the immobilization was successful.

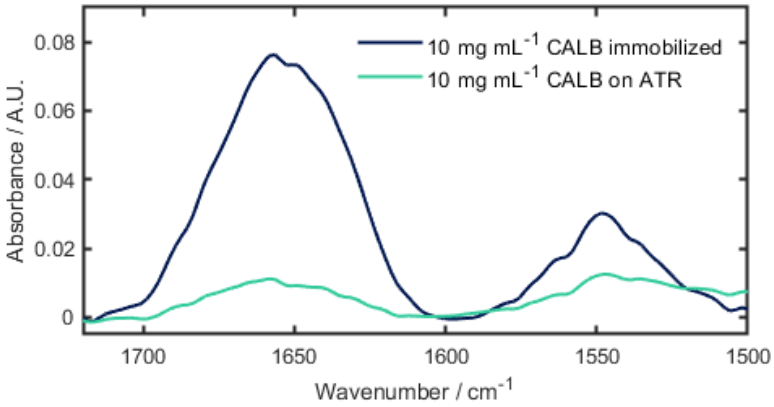

Figure 3.33.: IR spectrum of 10 mg mL^{-1} CALB in phosphate buffer solution measured with an un-coated ATR crystal (turquoise) and a mesoporous silica coated ATR crystal (dark blue), showing the amide I and amide II band of the lipase.

Furthermore, the enzyme loading of the pores was approximated. For this, BSA ATR calibrations for the amide I and amide II bands were used, since a calibration with CALB was difficult due to it being dissolved in glycerine. These calibrations can be found in the Appendix (Figure 3 and Figure 4). Through this calibration, the measured absorbance of the amide I and amide II bands of 10 mg mL^{-1} CALB after immobilization (Figure 3.33-dark blue) result in a CALB concentration of 41.44 mg mL^{-1} and 17.55 mg mL^{-1}, respectively. Due to the different ratio between the amide I and amide II band in CALB and BSA, the concentration of CALB was approximated by taking the average of the two concentrations, 29.5±12 mg mL^{-1}. The concentration was corrected under consideration that the evanescent field inside the layer accounts for only 85 %, resulting in a concentration of 34.7 mg mL^{-1}. From the dimensions of the ATR crystal and the layer thickness, a mesoporous silica layer volume of $1 \cdot 10^{-4}$ cm^3 was determined. The porosity of the silica was estimated to be about 63 % based on the work from Steinbacher[54], leading to a pore volume of $6.3 \cdot 10^{-5}$ cm^3. This

resulted in a CALB mass of 2.186 µg in the pores, which equaled to $6.53 \cdot 10^{-11}$ mol CALB (M_{CALB}=33.5 kDa). Using Avogadro's number (=$6.022 \cdot 10^{23}$), the number of molecules in the pores could be calculated, which equaled to $3.93 \cdot 10^{13}$. The volume of a CALB molecule of $60 \cdot 10^{-21}$ cm^3[61] lead to a total CALB volume of $2.36 \cdot 10^{-6}$ cm^3 in the pores. This equates to 3.7 % of the total pore volume.

CALB has already been successfully immobilized on mesoporous silica in pores approx. 5 nm. The immobilized CALB showed a higher stability, re-usability and enhanced catalytic activity.[83] These literature findings are very promising for performance of the immobilized CALB in the FAME conversion reaction.

3.4. FAME Enrichment on Unfunctionalized Mesoporous Silica Results

The concentrations of MM for this experiment were chosen to cover the region of interest for the FAME quantification in jet fuel.[1] No signal, and therefore no enrichment, could be observed in the spectra. A reason for this could be that MM is too apolar due to its long alkyl tail (which makes it an attractive substrate of the lipid-attracted enzyme, lipase), therefore maiking it unatteacted to the polar surface of the silica. Furthermore, since this experiment was only performed once, it is possible that the mesoporous layer was faulty, making it difficult for the MM to enter the pores. Nevertheless, it was decided to not pursue this method any further during the scope of this thesis, because of the more promising results of the lipase-catalyzed approach.

3.5. Considerations Regarding the Quantification

In Section 2.3., the two possibilities of substrate determination in an enzymatic reaction were introduced, both of which are utilizable methods for the biosensor. In both cases a calibration with a standard series would be necessary. In general, preliminary tests need to be performed to determine the kinetic parameters, since the feasibility of each method is dependent on these parameters. If the concentration of FAME in jet fuel was substantially lower than K_m, then the "kinetic" approach would present as a better option. The relationship between the reaction rate and substrate concentration in this region is linear. The determination of the initial rate of the reaction for a sample and subsequently relating it to a measured calibration curve measured beforehand results in the simple quantification of the substrate. The advantage of this approach is the time efficiency. The

disadvantage is that the sensitivity of the IR spectrometer needs to be good enough to be able to record the initial decrease in the FAME band and, thus, guarantee a good limit of detection (LOD) of the biosensor, since the initial rate is ideally determined right at the beginning of the reaction.[43] On the other hand, the "complete conversion" approach would be a better choice if K_m for the set parameters is smaller than the FAME concentration in kerosene. This approach is also highly dependent on v_{max}, which should be as high as possible. Since v_{max} is dependent on the enzyme concentration, a high enzyme loading on the silica pores would be of great advantage. The high conversion of FAME with this method is advantageous because of the high carbonyl band intensity drop, which is easy to detect. Contrary to the "kinetic" approach, this approach is time-demanding, which is generally undesirable. It is possible to change some of the parameters of the reaction, i.e. the amine concentration or temperature, to influence the kinetic parameters in order to steer the quantitative analysis approach in a specific direction. Though, this can only be done to a certain degree, since most reaction parameters are set by the nature of the experiment. There are advantages and disadvantages to both approaches, therefore it is crucial to evaluate which factors are more important in combination with the specified reaction and detection method.

4. Conclusions and Outlook

This work was started with the aim of developing a biosensor for the quantification of low concentrations of FAME. The chemical analysis technique of the senor is ATR-FTIR spectroscopy, enhanced by a mesoporous silica film coating on the ATR-crystal, used for the immobilization of a lipase-catalyst for facilitating the conversion of the FAME. Three big steps towards a functioning entity were made through this work.

Firstly, the synthesis of the mesoporous layer was optimized to attain a product which fits the requirements set by different aspects of the biosensor. On the one hand, it was important for the mesopores of the layer to be large enough to accommodate the biocatalyst, lipase, which is a relatively large molecule. Therefore, from the beginning, surfactant molecules were chosen in the synthesis with the aim to enlarge the pores. The used surfactants were CTAB and F127. The latter was quickly established as the better performer in regards to producing bigger-sized mesopores. Furthermore, a higher surfactant to TEOS ratio proved to be successful as well; the optimal molar ratio being 0.0096 to 1, the synthesis denoted with AL07B. The second important aspect concerning the silica film was its layer thickness. After some considerations regarding the evanescent field of the ATR-crystal, the decision was made to modify the synthesis towards a thickness of 500 nm. This was achieved by altering the ratio of ethanol in the synthesis. Changing the ethanol to TEOS ratio in the AL07B synthesis from 16:1 to 25:1, a film with the desired thickness could be synthesized. The final synthesis molar ratio of reagents was TEOS:F127:EtOH:0.1MHCl:H_2O=1:0.0096:25:0.0152:16.29, producing a mesoporous silica layer with approx. 8 nm pores and a thickness of 500 nm.

Secondly, the enzymatic reaction was tested and optimized. Given that the intrinsic reaction of lipases is hydrolysis, this reaction was tested first. Among the five lipases tested on the substrate triacetin, CALB exhibited the fastest initial reaction, leading to higher a conversion at shorter reaction times. In contrast, LIPEX had a higher maximal reaction rate, v_{max}, resulting in greater triacetin conversion at longer reaction times. A higher reaction temperature of 40 °C proved beneficial for all the reactions performed. The enzymatic process more relevant for the biosensor, aminolysis, required additional attention. After testing all combinations of three lipases and four amines in the conversion of a FAME,

methyl myristate, CALB and 2MEA showed the best conversion performance. The pair showed the highest conversion after 6 h and near complete conversion, with 95 %, after 72 h. The lack of side products during the reaction was another positive aspect as well. CALB was therefore selected for immobilization on the mesoporous silica coated ATR-crystal.

Finally, immobilization experiments were undertaken for CALB. After comparing the amide II band intensity of CALB between an un-coated and a mesoporous silica coated ATR-crystal, it could be concluded that the lipase was indeed adsorbed inside the mesopores of the silica film. Through the immobilization, the stability as well as the activity of the lipase should be enhanced, thereby improving the efficiency of the aminolysis reaction in the biosensor.

Within this work, the foundation of the mesoporous silica-based MIR biosensor for the quantification of FAME has been laid. Next in line would be the testing of the aminolysis reaction with the immobilized CALB and 2MEA within the mesoporous layer by ATR-FTIR spectroscopy. After a successful outcome, the kinetics of the reaction need to be determined to decide on the method of quantification for the biosensor. Based on the decision, a standard series needs to be measured, either by the "kinetic" or the "complete conversion" approach, for external calibration. A sample with a known FAME concentration needs to measured and evaluated with the calibration. Following an accurate sample FAME concentration determination, an initial working biosensor would be established.

5. Experimental

5.1. Chemicals

All following chemicals were used as purchased without further alteration or purification: heptane (*Sigma-Aldrich*, CHROMASOLV®, for HPLC, ⩾99 %), acetone (*VWR*, GC-capillary grade), ethanol (EtOH, *Chem-Lab NV*, abs. 100 % a.r.), tetraethyl orthosilicate (TEOS, *Sigma*, ⩾99.0 %), Pluronic® F-127 (*Sigma*, powder, BioReagent), 3-methoxypropylamine (3MPA, *Sigma-Aldrich*, 2-methoxyethylamine (2MEA, *Sigma-Aldrich*), 99 %), 3-isopropoxypropylamine (3PPA, *TCI*, ⩾98.0 %), 3-(Dimethylamino)-1-propylamine (3DAPA, *Sigma-Aldrich*, 99 %), Amano Lipase A from Aspergillus niger (ALA, *Sigma-Aldrich*, ⩾120,000 U g^{-1}), Amano Lipase from Pseudomonas fluorescens (ALPF, *Sigma-Aldrich*, ⩾20,000 U g^{-1}), Lipase from Candida rugosa (LCR, *Sigma*, Type VII, 900 U g^{-1}), 99 %), Lipex® (LIPEX, *Chiralvision*), Candida Antarctica Lipase B (CALB, *Chiralvision*, liquid), methyl myristate (MM, *Sigma-Aldrich, for synthesis*), methyl palmitate (*Sigma-Aldrich*, analytical standard), methyl stearate (*Sigma-Aldrich*, analytical standard), hexamethyldisilazane (HMDS, *TCI*, >96 %), sodium hydroxide (*ITW Reagents, pellets, pharma grade*, di-sodium hydrogen phosphate dihydrate (*Merk*, for analysis), sodium phosphate monobasic monohydrate (*Sigma-Aldrich*, ⩾98 %), glycerol triacetate (*Sigma-Aldrich*, ⩾99 %). Hydrochloric acid (HCl, *Merck KGaA*, fuming 37 %) was diluted with deionized water to recieve 0.056 M and 0.1 M HCl.

5.2. Synthesis of Mesoporous Silica Films

The synthesis of the mesoporous layers was performed based on the procedures established by Steinbacher[54] and Baumgartner[59].

The objective was to obtain mesoporous layers with pores large enough to accomodate lipases. The target of >10 nm for the pore size was set to accommodate a range of lipase sizes. Therefore, different *sol-gel* batches were prepared and characterized to determine the optimal candidate for further investigation. The parameters that were varied in the synthesis were the type of surfactant (CTAB, F127), the amount of surfactant, the relative

humidity during spin-coating and the amount of ethanol added to the solution.

To test the films before applying them on an ATR crystal, they were applied on 20 x 10 mm single-side-polished silicon platelets, which were cut out of a silicon wafer. Later, Si ATR crystals (20 x 10 x 0.5 mm^3) cut out of a double-sided-polished Czochralski Silicon wafer were faceted on a 45 ° angle with three aluminum oxide (15 µm, 9 µm, 3 µm) discs and two diamond (1 µm, 0.1 µm) polishing discs.

In the upcoming chapters, each synthesis batch is designated by the label ALXYZ, where AL represents Adea Loxha, XY is a sequential number starting from 01, and Z indicates either A for CTAB or B for F127, depending on the surfactant used in the synthesis. If the heat treatment is carried out at 80 °C or 110 °C, 'y1' or 'y2' is appended to the name, respectively. Additionally, if the sample undergoes calcination, 'z' is included. To illustrate, AL05B_y2_z would identify a sample synthesized by the author (Adea Loxha), the fifth batch overall (at least one different parameter compared to the previous four), using F127 as the surfactant, subjected to heat treatment at 110 °C, and finally, calcined at 400 °C.

5.2.1. Synthesis with CTAB as Surfactant

The synthesis of mesoporous silica films with CTAB as surfactant was started by the addition of 1.75 g abs. EtOH, 2.08 g TEOS and 0.9 g 0.056 M HCl in a round necked flask. The solution is then heated under reflux. Concurrently, 0.041g CTAB were dissolved in 0.4 g abs. EtOH. After 3 h under reflux, 0.5 mL of the first solution are added to the CTAB solution and stirred for 5 min. Every dissolving step was supported by ultrasonic bathing, if necessary. The final solution is used for spin-coating. These steps and conditions yielded a film with a 3D hexagonal structure. The final ratios of the synthesis can be found in Table 5.1

Table 5.1.: Molar ratios and reagent amounts used in the CTAB mesoporous layer synthesis.

AL01A	TEOS	CTAB	EtOH	0.056 M HCl	H_2O
molar ratio	1	0.12	13	0.005	5
mmol	0.9365	0.1125	12.2459	0.01125	4.6858
g	0.1951	0.041	0.5641	0.8442	0.0844

5.2.2. Synthesis with Pluronic F-127 as Surfactant

To prepare the batches AL01B to AL04B, F127 was dissolved in a mixture of EtOH, 0.056 M HCl, and water. Once the polymer was fully dissolved, tetraethyl orthosilicate (TEOS) was introduced, and the solution was briefly shaken. Following a 10-minute aging period (simply storing the solution at room temperature without stirring), the sol was utilized for spin-coating. Subsequently, heat treatment was conducted at 80 °C/110 °C overnight, followed by calcination at 400 °C for 4 hours (3 h temperature ramp). The reactant amounts for each batch are given in Table 5.2.

The molar ratio for the initial three batches remained consistent; however, the varying parameter in this instance was the humidity during spin-coating. Specifically, AL01B was spin-coated at 20 % relative humidity, AL02B at 40 %, and AL03B at 60 %. This choice was influenced by Steinbacher's findings[54], which indicated a humidity-dependent pore size development in films produced through this synthesis procedure.

Table 5.2.: Molar ratios and reagent amounts used in the mesoporous silica syntheses AL01B-04B with F127 as a surfactant.

	TEOS	F127		EtOH	0.056 M HCl	H_2O
		AL01B-03B	AL04B			
molar ratio	1	0.0036	0.0094	18.62	0.0145	30.49[a]
mmol	0.5500	0.0020	0.0052	10.2805	0.0080	16.8333[a]
g	0.1150	0.0250	0.0650	0.4736	0.1430	0.1600
mL	0.1220				0.1430	0.1600

[a] After taking the water from the 0.056 M HCl into account

A variation of the aforementioned synthesis was realized for the batches AL05B to AL10B. To create the sol, EtOH, TEOS, and 0.1 M HCl were stirred at room temperature for 20 minutes. Simultaneously, a polymer solution (=pol) was prepared by stirring F127, EtOH, 0.1 M HCl, and water until the sol solution was ready and the polymer (F127) was completely dissolved. The two solutions were combined and gently stirred for 3 hours at room temperature before spin coating. The resulting material underwent heat treatment at 80 °C/110 °C overnight, followed by calcination at 400 °C for 4 hours. All reagent amounts and ratios can be found in Table 5.3 and Table 5.4.

Table 5.3.: Molar ratios and reagent amounts used in the mesoporous silica syntheses AL05B-10B with F127 as a surfactant.

	TEOS	F127	EtOH		0.1 M HCl		H_2O	
	sol	pol	sol	pol	sol	pol	sol	pol
sum ratio	1		16		0.0152		16.29	
molar ratio	1.0000		8.6966	7.3051	0.0108	0.0044	6.0044	10.2831[a]
mmol	3.1200	[b]	27.1338	22.7924	0.0338	0.0136	18.7341	32.0839[a]
g	0.6500		1.2500	1.0500	0.3375	0.1360		0.4420
mL	0.6915		1.5843	1.1170	0.3375	0.1360		0.4420

[a] After taking the water from the 0.1 M HCl into account

[b] The amounts of F127 are dependent on the *sol-gel* batch and can be found in Table 5.4

Table 5.4.: Molar ratios between F127 surfactant and TEOS for and surfactant amounts used in the syntheses AL05B-10B.

	molar ratio F127/TEOS	mmol	g
AL05B	0.0030	0.0093	0.1160
AL06B	0.0037	0.0115	0.1435
AL07B	0.0097	0.0302	0.3770
AL08B	0.0095	0.0296	0.3695
AL09B	0.0118	0.0370	0.4620
AL10B	0.0142	0.0444	0.5545

Upon measuring the film thickness, it became evident that the batches that seemed promising in terms of pore size (AL07B) resulted in films that exceeded the optimum thickness based on depth of penetration. Thus, to maintain the pore size constant while achieving thinner films, the EtOH ratio in the reaction was increased. While keeping all other parameters and conditions constant for the AL07B batch, three variations of the batch were prepared with different EtOH ratios (18, 15 or 28.5 instead of 16). Synthesis details are summarized in Table 5.5.

Table 5.5.: Molar ratios and reagent amounts used in the mesoporous silica syntheses AL07B with different ethanol concentrations.

			sum molar ratio	molar ratio	mmol	g	mL
TEOS		sol	1	1.0000	3.1200	0.6500	0.6915
F127	AL07B	pol	0.0096	0.0096	0.0302	0.3770	
	AL10B		0.0142	0.0142	0.0444	0.5545	
EtOH		sol		8.6966	27.1338	1.2500	1.5842
	A		18	9.3032	29.0267	1.3372	1.6948
	B	pol	25	16.3029	50.8661	2.3433	2.9700
	C		28.5	19.8031	61.7869	2.8464	3.6076
0.1 M HCl		sol	0.0152	0.0108	0.0338	0.3375	0.3375
		pol		0.0044	0.0136	0.1360	0.1360
H_2O		sol	16.29	6.0044[a]	18.7341[a]		
		pol		10.2831[a]	32.0839[a]	0.5780[a]	0.4420

[a] After taking the water from the 0.1 M HCl into consideration

5.2.3. Spin-Coating

Spin-coating for all mesoporous silica syntheses was performed on silicon platelets (described in section 5.2.) and for the final chosen layer on a silicon ATR crystal. The substrate (either platelate or crystal) was spun at 1750 rpm for 50 sec. The relative humidity was varied based on the synthesis, varying from 20 % to 60 %. For the final layer the relative humidity inside the spinning chamber was held at 40 %. The substrate was thoroughly cleaned before spin-coating in an ultrasonic bath while being submerged in EtOH, and wiped down with acetone right before coating. After closing the chamber and letting the relative humidity stabilize, the substrate was spun and 60-80 µL of the sol sample were deposited from the top on to the middle of the substrate. After spin-coating, the sample was heat treated at 110 °C overnight.

5.2.4. Functionalization of Mesoporous Silica Films

For functionalization, the ATR crystal or Si platelet with the calcined mesoporous silica layer was placed in an empty three-necked round bottom flask. The flask was then connected to a reflux cooler, evacuated and flushed with nitrogen three times. An oil bath was heated to 150 °C and the flask was placed inside the bath for 2 h under vacuum. Next, the

temperature was reduced to 90 °C and 20 mL abs. acetone as well as 0.5 mL HMDS were added to the flask under nitrogen counter flow. The sample in solution was heated under reflux for another 4 h. Finally, the sample was taken out, thoroughly washed with acetone and placed in an 150 °C oven over night.

Remark: The acetone serves as a removal agent for the CTAB as well.[84]

5.3. Characterization of Mesoporous Silica Films

5.3.1. Small-Angle X-Ray Diffraction

The X-ray diffraction data was recorded with an Empyrean PANanalytical multipurpose diffractometer with Bragg-Brentano geometry (BBHD mirror) and Cu(Kα) primary radiation ($\lambda_{K\alpha}$=1.54 Å) at 45 kV and 40 mA. A divergent slit of 1/8°, a 0.04 rad soller slit, a 10 mm mask, an anti-scatter slit of 1/2°, a 150 µm beam knife and a GalliPix detector were used. The samples were measured at room temperature between 0° and 5° (2θ), with a step size of 0.0071620 °.

5.3.2. Profilometer

A Dektak Stylus profilometer (Bruker, Germany) was used for measuring the mesoporous silica film thickness. The film was scratched at three different positions, the indents of which were subsequently measured.

5.3.3. Contact angle measurements

Contact angle measurements were performed on a KRÜSS DSA30 drop shape analyzer. The Sessile Drop method was used in the KRÜSS ADVANCE software, with water as solvent. A drop of 2 µm was produced with a rate of 0.16 mL min^{-1} and deposited on the surface of the mesoporous layer, either before or after functionalization. The analysis of the contact angle was performed by Young Laplace fitting method with automatic baseline correction.

5.3.4. Transmission electron microscopy (TEM)

Transmission electron microscopy measurements were performed on a TECNAI F20 with a X-FEG emitter and an operating voltage of 200 kV (energy resolution: 0.7 eV, lattice resolution: 0.14 nm). The operating camera was a Gatan Rio16, 30 fps full HD. The sample (AL07B_y2_z_25) preparation was done using a focused ion beam (FIB).

5.4. Dynamic Light scattering Experiments

To determine the particle size of CALB, dynamic light scattering (DLS) measurements were performed. DLS measurements were conducted using a Liteizer 500 instrument from Anton Paar, Austria, at a temperature of 25 °C. The instrument was calibrated and temperature stabilized for 60 s prior to measurements. The necessary measurement paramters were adjusted for a 50:50 water-glycerine mixture according to the CALB sample dilution. Particle size distribution functions were determined according to ISO 22412 using a narrow analysis model in the Kalliope software package provided by Anton Paar, Austria.

5.5. Enzymatic Reactions

5.5.1. Hydrolysis Reaction

Firstly, a standard series (100 mM, 200 mM, 300 mM, 400 mM, 500 mM) of triacetin in water with a pH of 7.5 (phosphate buffer) and a blank were prepared. To prepare a 0.1 M phosphate buffer with a pH of 7.5, 2.3389 g sodium dihydrogen phosphate monohydrate and 5.8825 g sodium hydrogen phosphate dihydrate were dissolved in distilled water. A pH electrode and sodium hydroxide were used to adjust the pH of the buffer if needed and the solution was added to a 500 mL volumetric flask, which was subsequently filled to its mark. The correct amount of triacetin for the 500 mM standard solution was used, dissolved, and topped with buffer. This standard solution was subsequently to produce the lower concentration standard solutions.

The instrument used for the measurements was a Bruker Vertex 80v FT-IR Spectrometer and the experiments were performed in a transmission cell setup. The parameters of the method were as follows: scan range between 800-4000 cm^{-1}, 256 scans, 3 mm aperture, 80 kHz, path-length 15 µm, with a spectral resolution of 4 cm^{-1}. The software OPUS 8.0 was used for data processing.

A blank sample of only the phosphate buffer and the five standard solutions were measured, with the phosphate buffer being the background. Based on the signal intensity of the absorbance of each standard, a concentration of 250 mM triacetin was chosen for the following hydrolysis reaction.

For the hydrolysis reaction 20 mL of 250 mM triacetin solution were added to a 40 mL screw top vial. Subsequently, 50 mg (or 500 µL for liquid lipases with a lipase concentration of 10 %) lipase are added to the vial. The sample was measured with phosphate buffer as a background (t_0). The vial was then placed in a 40 °C oven or left at room temperature

for 6 h. Afterwards, the sample was measured with phosphate buffer as a background (t_1). The sample was then placed once more in the oven at 40 °C or left at room temperature for further 66 h (for a total of 72 h). These steps were performed with five different lipases: LCR, APFL, ALAA, CALB and LIPEX. For an overview refer to Table 5.6.

Table 5.6.: Summary of performed lipase-catalyzed hydrolysis reactions.

	LCR	ALPF	ALAA	CALB	LIPEX
20 °C	6 h	6 h	6 h	6 h	6 h
	48 h	72 h	72 h	72 h	72 h
40 °C	6 h	6 h	6 h	6 h	6 h
	72 h	72 h	72 h	72 h	72 h

Following the testing of the five lipases, CALB and ALPF were chosen fur further investigation. *In-situ* experiments in a transmission configuration (Figure 5.1) were performed where 250 mM triacetin in a 0.1 M buffer was continuously pumped with a rate of 1 mL min^{-1} (*via* peristaltic pump) through the transmission cell. A repeated measurement was started, consisting of 66 measurements, with a delay of 30 sec and a scanning time of 0.4 min. The other parameters of the method were kept unchanged. After a stable baseline was obtained, 250 µL of CALB or 25 mg of ALPF were added to the 20 mL of sample with the triacetin substrate. This was repeated for six triacetin concentrations: 5 mM, 10 mM, 20 mM, 60 mM, 100 mM, and 250 mM.

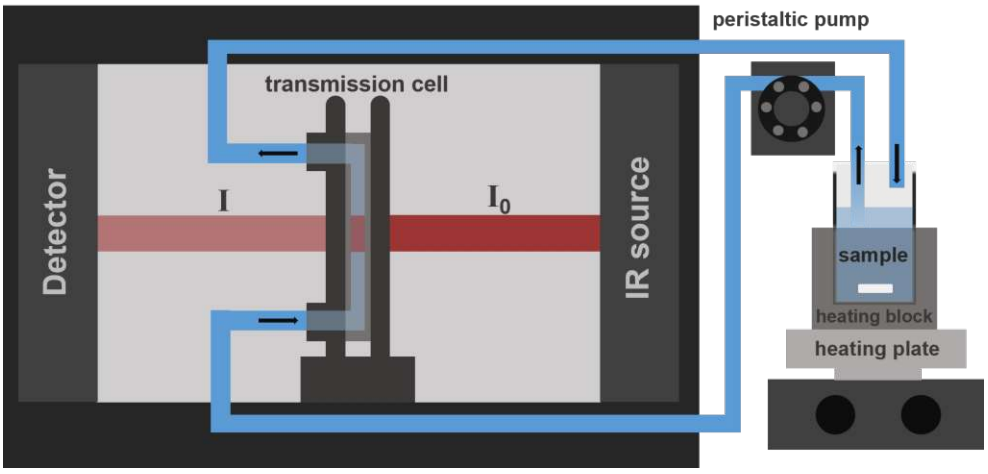

Figure 5.1.: Experimental configuration of the in-situ transmission measurements of the enzymatic reactions.

5.5.2. Aminolysis Reaction

The reaction solution was started with the addition of 20 mL of heptane with a concentration of 1 g L^{-1} (4 mM) FAME in a 40 mL screw top vial. This amounts to 0.08 mmol FAME. The main FAME used in the experiments was methyl myristate, but some reactions were also performed with methyl stearate and methyl palmitate. Here, the same conditions were chosen. Next, 0.24 mmol of amine and 50 mg of lipase or 500 µL (approx. 1.4 mmol) of liquid lipase (glycerine with a lipase concentration of approx. 10 %) were added to the vial. The added amount of each amine can be found in Table 5.7. After a short shake, the sample was quickly measured with heptane as background. This measurement represented the IR spectrum at t_0. The sample was then placed into an oven at a set temperature (T) for a defined amount of time (t_1). An overview of the experiments can be found in Table 5.8. After the completion of t_1, the sample is measured, once again, with a heptane background. This represents the IR spectrum at t_1.

Table 5.7.: Characteristics of the amines used in the enzymatic aminolysis reactions.

	3PPA	3DAPA	3MPA	3MEA
Molecular weight / g mol^{-1}	117.19	102.18	89.14	75.11
Density (25 °C)[85] / g mL^{-1}	0.845	0.812	0.874	0.870
Amount used / µL	33.2	30.2	24.4	20.7

Table 5.8.: Summary of performed lipase-catalyzed aminolysis reactions.

	3PPA		3DAPA		3MPA		2MEA	
T / °C	40	60	40	60	40	60	40	60
CALB								
LIPEX			t_1 = 6 h and 72 h					
LCR								

The instrument and the method used were kept identical as described in Section 5.1.1., the only difference being the path-length of the cell with 1 mm. For every measurement, 2.5 mL of sample were pumped through the transmission cell with a rate of 2 mL min^{-1} and the cell was washed with heptane between each measurement until the baseline showed no signs of the sample.

For the *in-situ* aminolysis reaction, the same amounts stated above were used. The screw top vial with FAME dissolved in heptane with the addition of amine was placed in an

aluminum cylinder, which was subsequently heated until the sample reached and held 40 °C during continuous stirring. The setup was identical to the one used for the *in-situ* hydrolysis reaction experiments (Figure 5.1). After stable conditions were reached, a background spectrum of heptane was measured. Next, the sample was pumped through the transmission cell in a loop with a speed of 1.5 mL min^{-1}. The lipase was added to the vial and a repeated measurement over 60 min was started with a measurement delay of 1 min and a scan time of 0.5 min. The lipase chosen for the for *in-situ* investigation was LCR. The reason behind the decision was the availability of the lipase in a powder form. Since purchased form of CALB and LIPEX was approx. 10 % in glycerine and the sample is stirred during the experiment, it was deemed unfavorable to test these two lipases in this type of experiment (discussed in Section 3.2.3.).

5.6. Lipase immobilization

An aluminum ATR flow cell with a volume of 20 µL mounted inside a Bruker Vertex 80v spectrometer was used for the following experiments. The seal between the cell and ATR crystal was achieved through a FKM O-ring (heptane resistant).

5.6.1. Un-coated ATR Crystal

For later comparison, adsorption experiments on a un-coated ATR crystal were performed. The lipase used for this investigation was CALB because of its better performance compared to the other lipases during both the hydrolysis and aminolysis reactions. Four lipase concentrations were prepared (1 mg mL^{-1}, 2 mg mL^{-1}, 5 mg mL^{-1}, 10 mg mL^{-1}) by dissolving the lipase in a pH 7.5 0.5 M phosphate buffer, assuming a 10 wt% solution of enzyme in glycerine. The phosphate buffer was pumped though the ATR cell (0.5 mL min^{-1}) for 15 min and was then measured as background. Next, the sample was continuously pumped though the cell in a loop (0.5 mL min^{-1}) while a repeated measurement over 20 min was started (scan delay 0.5 min, scan time 0.4 min, 40 repetitions, aperture 8 mm, resolution 4 cm^{-1}). After 20 min, the cell was flushed with phosphate buffer to remove loosely adsorbed lipase while, again, starting a repeated measurement (identical parameters). At the end, 1 % sodium dodecyl sulfate (SDS) in pH 7.5 0.1 M phosphate buffer was run through to remove adsorbed lipase from the ATR crystal and repeated spectra were measured for another 20 min. These steps were performed for all four lipase concentrations.

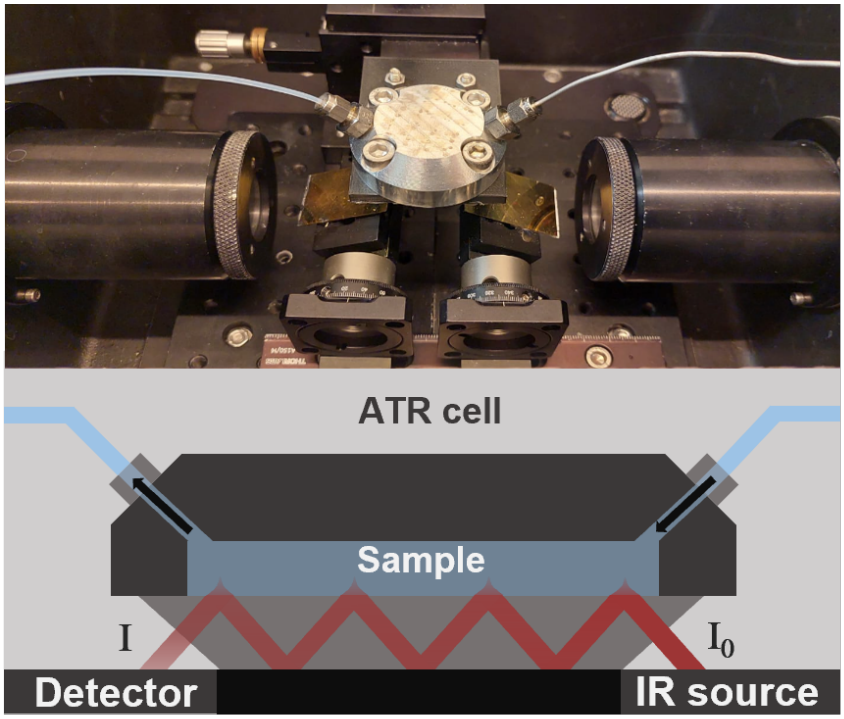

Figure 5.2.: A picture of the ATR measurement configuration on a Bruker 80v spectrometer used for the experiments is shown on top and a schematic representation of ATR cell on the bottom.

5.6.2. Coated and Functionalized ATR Crystal

The procedure for the lipase immobilization on the mesoporous silica coated and functionalized Si ATR crystal was similar to the one used for the un-coated ATR crystal. The same four CALB concentrations in a pH 7.5 0.5 M phosphate buffer were used (1 mg mL^{-1}, 2 mg mL^{-1}, 5 mg mL^{-1}, 10 mg mL^{-1}). The cell was flushed with the same buffer for 15 min before the immobilization until a stable spectrum was recorded. Next, the lowest concentration of CALB (1 mg mL^{-1}) was pumped though the cell in a loop with 0.5 mL min^{-1}. A spectrum was measured every 30 sec for 50 min (scan delay 0.5 min, scan time 0.4 min, 100 repetitions, aperture 8 mm, resolution 4 cm^{-1}) with phosphate buffer as a background. The cell was subsequently washed though with buffer for 20 min, all the while measuring every 30 sec (40 repetitions). These steps were repeated for the next three CALB concentrations. Finally, the cell was flushed with 1 % SDS in phosphate buffer, to remove the lipase. SDS was pumped though for 30 min, while, again, continuously measuring every 30 sec (60 repetitions).

5.7. FAME Enrichment on Unfunctionalized Mesoporous Silica

For testing the FAME enrichment on the unfunctionalized mesoporous silica coated ATR-crystal, four methyl myristate concentrations in heptane were prepared (0.05 g L^{-1}, 0.125 g L^{-1}, 0.25 g L^{-1}, 0.5 g L^{-1}). The ATR cell with the coated crystal was flushed with heptane *via* a peristaltic pump with 1.5 mL min^{-1} for 15 min before the enrichment experiment and heptane was recorded as background. Next, the lowest concentration of FAME was pumped in a loop though the cell with 1.5 mL min^{-1}. A spectrum was measured every 30 sec for 60 min (scan delay 0.5 min, scan time 0.4 min, 120 repetitions, aperture 8 mm, resolution 4 cm^{-1}). Each concentration was followed by a wash step with heptane for 5 min and then the next lowest concentration was measured.

Appendix

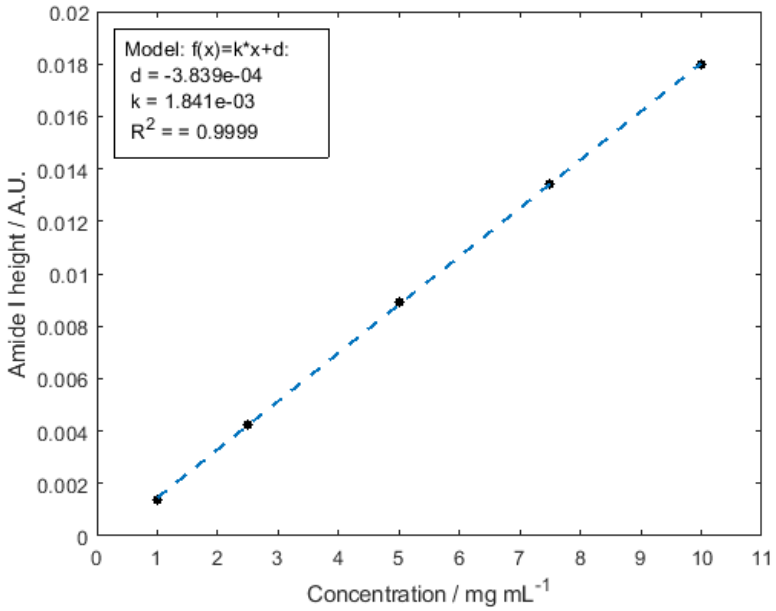

Figure 3.: Linear fit of the amide I band of BSA measured with by ATR spectroscopy with a laser based detector

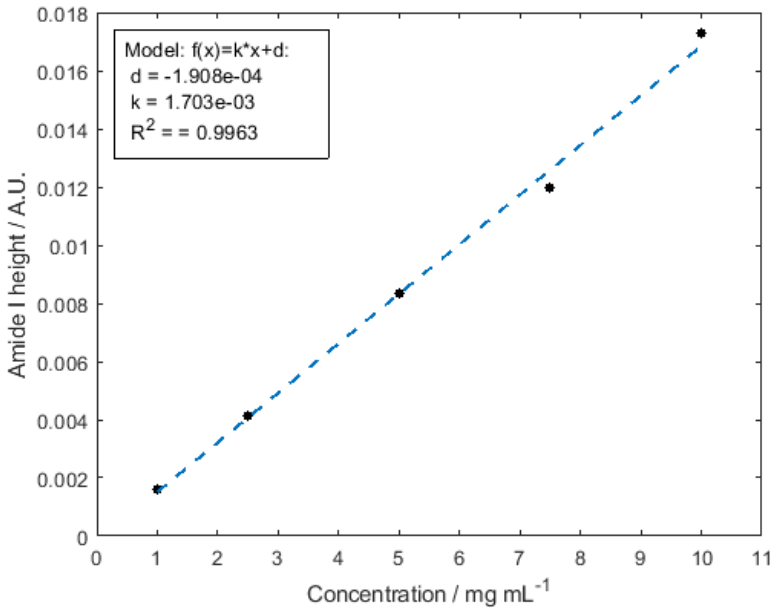

Figure 4.: Linear fit of the amide II band of BSA measured with by ATR spectroscopy with a laser based detector

List of Figures

List of Tables

Bibliography

[1] Defence standard 91-091, October 2019. Issue 11.

[2] (Quantared Technologies GmbH) Wolfgang Ritter, Bernhard Lendl. VERFAHREN ZUR QUANTITATIVEN BESTIMMUNG VON FETTSÄUREESTERN IN TREIBSTOFFEN, 2020.

[3] Standard test method for determination of fatty acid methyl esters (FAME) in aviation turbine fuel using mid-infrared laser spectroscopy, 2020.

[4] Bruker. SPECTROSCOPY BASICS: FT-IR or IR spectroscopy? https://www.bruker.com/en/products-and-solutions/infrared-and-raman/ft-ir-routine-spectrometer/what-is-ft-ir-spectroscopy/difference-ir-vs-ftir.html. Accessed: 2024-05-01.

[5] Peter R. Griffiths and James A. de Haseth. *Fourier Transform Infrared Spectroscopy*. John Wiley & Sons, 2 edition, 2007.

[6] Georg Ramer and Bernhard Lendl. Attenuated total reflection fourier transform infrared spectroscopy, March 2013.

[7] A. A. Michelson and E. W. Morley. On the relative motion of the earth and the luminiferous ether. *American Journal of Science*, s3-34(203):333–345, November 1887.

[8] Glen Fox. The brewing industry and the opportunities for real-time quality analysis using infrared spectroscopy. *Applied Sciences*, 10(2):616, January 2020.

[9] Francis M. Mirabella. Internal reflection spectroscopy: Theory and applications, August 2020.

[10] Lacey A. Averett, Peter R. Griffiths, and Koichi Nishikida. Effective path length in attenuated total reflection spectroscopy. *Analytical Chemistry*, 80(8):3045–3049, March 2008.

[11] M. Ebelmen. On silicic æthers. *The London, Edinburgh, and Dublin Philosophical Magazine and Journal of Science*, 25(167):397–398, nov 1844.

[12] Thomas Graham. Xxxv. on the properties of silicic acid and other analogous colloidal substances. *J. Chem. Soc.*, 17(0):318–327, 1864.

[13] Jenaer Glaswerk Schott und Gen, 1939.

[14] H Schroeder and G Hass. Physics of thin films. *Advances in Research and Development*, 5:87, 1969.

[15] Lisa Klein, Mario Aparicio, and Andrei Jitianu, editors. *Handbook of Sol-Gel Science and Technology*. Springer International Publishing, 2018.

[16] Yonghui Deng, Jing Wei, Zhenkun Sun, and Dongyuan Zhao. Large-pore ordered mesoporous materials templated from non-pluronic amphiphilic block copolymers. *Chem. Soc. Rev.*, 42(9):4054–4070, 2013.

[17] Ulrich S. Schubert and Nicola Hülsing. *Synthesis of Inorganic Materials*. John Wiley & Sons, 1 edition, 2000.

[18] C. Jeffrey Brinker and George W. Scherer. *Sol-Gel Science*. Elsevier, 1990.

[19] Lok P. Singh, Sriman K. Bhattacharyya, Rahul Kumar, Geetika Mishra, Usha Sharma, Garima Singh, and Saurabh Ahalawat. Sol-gel processing of silica nanoparticles and their applications. *Advances in Colloid and Interface Science*, 214:17–37, dec 2014.

[20] Alain C. Pierre. *Introduction to Sol-Gel Processing*. Springer US, 1998.

[21] Ralph K. Iler. *The Chemistry of Silica: Solubility, Polymerization, Colloid and Surface Properties, and Biochemistry*. JOHN WILEY & SONS, 1979.

[22] George M. Whitesides, John P. Mathias, and Christopher T. Seto. Molecular self-assembly and nanochemistry: a chemical strategy for the synthesis of nanostructures. *Science*, 254(5036):1312–1319, nov 1991.

[23] C. Jeffrey Brinker, Yunfeng Lu, Alan Sellinger, and Hongyou Fan. Evaporation-induced self-assembly: Nanostructures made easy. *Advanced Materials*, 11(7):579–585, may 1999.

[24] U-Hwang Lee, Min-Hye Kimand, and Young-Uk Kwon. Mesoporous thin films with accessible pores from surfaces. *Bulletin of the Korean Chemical Society*, 27(6):808–816, 2006.

[25] Chengzhong Yu, Jie Fan, Bozhi Tian, Galen D. Stucky, and Dongyuan Zhao. Synthesis of mesoporous silica from commercial poly(ethylene oxide)/poly(butylene oxide) copolymers: Toward the rational design of ordered mesoporous materials. *The Journal of Physical Chemistry B*, 107(48):13368–13375, November 2003.

[26] Dongyuan Zhao, Jianglin Feng, Qisheng Huo, Nicholas Melosh, Glenn H. Fredrickson, Bradley F. Chmelka, and Galen D. Stucky. Triblock copolymer syntheses of mesoporous silica with periodic 50 to 300 angstrom pores. *Science*, 279(5350):548–552, jan 1998.

[27] C. T. Kresge, M. E. Leonowicz, W. J. Roth, J. C. Vartuli, and J. S. Beck. Ordered mesoporous molecular sieves synthesized by a liquid-crystal template mechanism. *Nature*, 359(6397):710–712, October 1992.

[28] Darren R. Dunphy, Pratik H. Sheth, Fred L. Garcia, and C. Jeffrey Brinker. Enlarged pore size in mesoporous silica films templated by pluronic f127: Use of poloxamer mixtures and increased template SiO_2 ratios in materials synthesized by evaporation-induced self-assembly. *Chemistry of Materials*, 27(1):75–84, dec 2014.

[29] Yan Yan, Sophia C. King, Man Li, Tiphaine Galy, Michal Marszewski, Joon Sang Kang, Laurent Pilon, Yongjie Hu, and Sarah H. Tolbert. Exploring the effect of porous structure on thermal conductivity in templated mesoporous silica films. *The Journal of Physical Chemistry C*, 123(35):21721–21730, aug 2019.

[30] Qisheng Huo, David I. Margolese, and Galen D. Stucky. Surfactant control of phases in the synthesis of mesoporous silica-based materials. *Chemistry of Materials*, 8(5):1147–1160, January 1996.

[31] Bettina Baumgartner, Jakob Hayden, Jérôme Loizillon, Sophia Steinbacher, David Grosso, and Bernhard Lendl. Pore size-dependent structure of confined water in mesoporous silica films from water adsorption/desorption using ATR–FTIR spectroscopy. *Langmuir*, 35(37):11986–11994, sep 2019.

[32] Benjamin Punz, Litty Johnson, Mark Geppert, Hieu-Hoa Dang, Jutta Horejs-Hoeck, Albert Duschl, and Martin Himly. Surface functionalization of silica nanoparticles: Strategies to optimize the immune-activating profile of carrier platforms. *Pharmaceutics*, 14(5):1103, May 2022.

[33] Hao Li, Xueping Chen, Danqing Shen, Fan Wu, Roser Pleixats, and Jianming Pan. Functionalized silica nanoparticles: classification, synthetic approaches and recent advances in adsorption applications. *Nanoscale*, 13(38):15998–16016, 2021.

[34] Jayesh Gupta, Mural Quadros, and Munira Momin. Mesoporous silica nanoparticles: Synthesis and multifaceted functionalization for controlled drug delivery. *Journal of Drug Delivery Science and Technology*, 81:104305, March 2023.

[35] Brian G. Trewyn, Igor I. Slowing, Supratim Giri, Hung-Ting Chen, and Victor S.-Y. Lin. Synthesis and functionalization of a mesoporous silica nanoparticle based on the sol-gel process and applications in controlled release. *Accounts of Chemical Research*, 40(9):846–853, July 2007.

[36] Kasim Mohammed Hello, Ahmed Abbas Ibrahim, Jawad K. Shneine, and Jimmy Nelson Appaturi. Simple method for functionalization of silica with alkyl silane and organic ligands. *South African Journal of Chemical Engineering*, 25:159–168, June 2018.

[37] T.I. Suratwala, M.L. Hanna, E.L. Miller, P.K. Whitman, I.M. Thomas, P.R. Ehrmann, R.S. Maxwell, and A.K. Burnham. Surface chemistry and trimethylsilyl functionalization of stöber silica sols. *Journal of Non-Crystalline Solids*, 316(2-3):349–363, February 2003.

[38] Editors of Encyclopedia Britannica The. enzyme. *Encyclopedia Britannica*, 2024.

[39] Jeremy M. Berg, John L. Tymoczko, and Lubert Stryer. *Biochemistry*. W.H. Freeman, 5 edition, 2002.

[40] Raymond G. Bistline, Alexander Bilyk, and Stephen H. Feairheller. Lipase catalyzed formation of fatty amides. *Journal of the American Oil Chemists' Society*, 68(2):95–98, feb 1991.

[41] Eleanore Seibert and Timothy S. Tracy. *Fundamentals of Enzyme Kinetics*, pages 9–22. Humana Press, 2014.

[42] Alistair Rogers and Yves Gibon. *Enzyme Kinetics: Theory and Practice*, pages 71–103. Springer New York, April 2008.

[43] Hans Bisswanger. *Enzyme Kinetics*. Wiley, jun 2017.

[44] Hans-Ulrich Bergmeyer, editor. *Methods of enzymatic analysis*. Elsevier Inc., 1965.

[45] J. W. Schmidberger, L. J. Hepworth, A. P. Green, and S. L. Flitsch. 1.4.4 enzymatic synthesis of amides. In *Biocatalysis in Organic Synthesis 1*. Georg Thieme Verlag KG, 2015.

[46] Max Lubberink, William Finnigan, and Sabine L. Flitsch. Biocatalytic amide bond formation. *Green Chemistry*, 25(8):2958–2970, 2023.

[47] Fred van Rantwijk, Michiel A. P. J. Hacking, and Roger A. Sheldon. Lipase-catalyzed synthesis of carboxylic amides: Nitrogen nucleophiles as acyl acceptor. *Monatshefte fuer Chemie/Chemical Monthly*, 131(6):549–569, jun 2000.

[48] Nikhil Bhalla, Pawan Jolly, Nello Formisano, and Pedro Estrela. Introduction to biosensors. *Essays in Biochemistry*, 60(1):1–8, June 2016.

[49] Leland C. Clark and Champ Lyons. Electrode systems for continuous monitoring in cardiovascular surgery. *Annals of the New York Academy of Sciences*, 102(1):29–45, October 1962.

[50] Boniphace Kanyathare and Kai-Erik Peiponen. Hand-held refractometer-based measurement and excess permittivity analysis method for detection of diesel oils adulterated by kerosene in field conditions. *Sensors*, 18(5):1551, May 2018.

[51] Mikhail N. Polyanskiy. Refractiveindex.info database of optical constants. *Scientific Data*, 11(1), January 2024.

[52] Bettina Baumgartner, Jakob Hayden, Andreas Schwaighofer, and Bernhard Lendl. In situ ir spectroscopy of mesoporous silica films for monitoring adsorption processes and trace analysis. *ACS Applied Nano Materials*, 1(12):7083–7091, December 2018.

[53] Yonghui Deng, Ting Yu, Ying Wan, Yifeng Shi, Yan Meng, Dong Gu, Lijuan Zhang, Yan Huang, Chong Liu, Xiaojing Wu, and Dongyuan Zhao. Ordered mesoporous silicas and carbons with large accessible pores templated from amphiphilic diblock copolymer poly(ethylene oxide)-*b*-polystyrene. *Journal of the American Chemical Society*, 129(6):1690–1697, jan 2007.

[54] Sophia Steinbacher. ATR FTIR spectroscopy for in situ monitoring of protein interaction with mesoporous silica films. Master's thesis, TU Wien, 2019.

[55] Hong Yang, Alex Kuperman, Neil Coombs, Suzan Mamiche-Afara, and Geoffrey A. Ozin. Synthesis of oriented films of mesoporous silica on mica. *Nature*, 379(6567):703–705, February 1996.

[56] S. van Pelt, R. L. M. Teeuwen, M. H. A. Janssen, R. A. Sheldon, P. J. Dunn, R. M. Howard, R. Kumar, I. MartÃnez, and J. W. Wong. Pseudomonas stutzeri lipase: a useful biocatalyst for aminolysis reactions. *Green Chemistry*, 13(7):1791, 2011.

[57] Lucie Couturier, Delphine Taupin, and Florent Yvergnaux. Lipase-catalyzed chemoselective aminolysis of various aminoalcohols with fatty acids. *Journal of Molecular Catalysis B: Enzymatic*, 56(1):29–33, January 2009.

[58] Sailas Benjamin and Ashok Pandey. Candida rugosa lipases: Molecular biology and versatility in biotechnology. *Yeast*, 14(12):1069–1087, December 1998.

[59] Bettina Baumgartner. *Mid-Infrared Spectroscopy and Porous Oxides*. PhD thesis, TU Wien, 2019.

[60] Rafaely N. Lima, Charlene S. dos Anjos, Erika V.M. Orozco, and André' L.M. Porto. Versatility of candida antarctica lipase in the amide bond formation applied in organic synthesis and biotechnological processes. *Molecular Catalysis*, 466:75–105, April 2019.

[61] Jonas Uppenberg, Mogens Trier Hansen, Shamkant Patkar, and T.Alwyn Jones. The sequence, crystal structure determination and refinement of two crystal forms of lipase b from candida antarctica. *Structure*, 2(4):293–308, April 1994.

[62] Benjamin Stauch, Stuart J. Fisher, and Michele Cianci. Open and closed states of candida antarctica lipase b: protonation and the mechanism of interfacial activation. *Journal of Lipid Research*, 56(12):2348–2358, December 2015.

[63] Pablo Domínguez de María, Jose M. Sánchez-Montero, José' V. Sinisterra, and Andrés R. Alcántara. Understanding candida rugosa lipases: An overview. *Biotechnology Advances*, 24(2):180–196, March 2006.

[64] Siliang Gao, Yujun Wang, Xiang Diao, Guangsheng Luo, and Youyuan Dai. Effect of pore diameter and cross-linking method on the immobilization efficiency of candida rugosa lipase in sba-15. *Bioresource Technology*, 101(11):3830–3837, June 2010.

[65] Marina Lotti, Anna Tramontano, Sonia Longhi, Fabrizia Fusetti, Stefania Brocca, Elisabetta Pizzi, and Lilia Alberghina. Variability within the candida rugosa upases family. *Protein Engineering, Design and Selection*, 7(4):531–535, 1994.

[66] Narisa Binhayeeding, Tewan Yunu, Nisa Pichid, Sappasith Klomklao, and Kanokphorn Sangkharak. Immobilisation of candida rugosa lipase on polyhydroxybutyrate via a combination of adsorption and cross-linking agents to enhance acylglycerol production. *Process Biochemistry*, 95:174–185, August 2020.

[67] J. Uppenberg and T.A. Jones. The sequence, crystal structure determination and refinement of two crystal forms of lipase b from candida antarctica, May 1994.

[68] P. Grochulski and M. Cygler. Two conformational states of candida rugosa lipase, January 1994.

[69] Andreas Schwaighofer, Christopher K. Akhgar, and Bernhard Lendl. Broadband laser-based mid-ir spectroscopy for analysis of proteins and monitoring of enzyme activity. *Spectrochimica Acta Part A: Molecular and Biomolecular Spectroscopy*, 253:119563, May 2021.

[70] Mustafa Kansiz, J.Richard Gapes, Don McNaughton, Bernhard Lendl, and K.Christian Schuster. Mid-infrared spectroscopy coupled to sequential injection analysis for the on-line monitoring of the acetone-butanol fermentation process. *Analytica Chimica Acta*, 438(1-2):175–186, July 2001.

[71] Roy M. Daniel, Michael J. Danson, Robert Eisenthal, Charles K. Lee, and Michelle E. Peterson. The effect of temperature on enzyme activity: new insights and their implications. *Extremophiles*, 12(1):51–59, September 2007.

[72] Sibel Fadiloglu and Zerrin Söylemez. Kinetics of lipase-catalyzed hydrolysis of olive oil. *Food Research International*, 30(3-4):171–175, April 1997.

[73] Editors of Encyclopedia Britannica Erik Gregersen, The. kerosene. *Encyclopedia Britannica*, 2024.

[74] John Coates. Interpretation of infrared spectra, a practical approach, oct 2000.

[75] Yan Ji, Xiaoliang Yang, Zhi Ji, Linhui Zhu, Nana Ma, Dejun Chen, Xianbin Jia, Junming Tang, and Yilin Cao. Dft-calculated ir spectrum amide i, ii, and iii band contributions of n-methylacetamide fine components. *ACS Omega*, 5(15):8572–8578, April 2020.

[76] Mehtap Fevzioglu, Oguz Kaan Ozturk, Bruce R. Hamaker, and Osvaldo H. Campanella. Quantitative approach to study secondary structure of proteins by ft-ir spectroscopy, using a model wheat gluten system. *International Journal of Biological Macromolecules*, 164:2753–2760, December 2020.

[77] T. Threlfall. The infrared spectra of amides. part 1. the stretching vibrations of primary carboxamides. *Vibrational Spectroscopy*, 121:103386, July 2022.

[78] Nicholas M. Holden, Mary Leigh Wolfe, and Enda J. Cummins. *Introduction to Biosystems Engineering*. Virginia Tech Publishing, 2021.

[79] S. Kent Hoekman, Amber Broch, Curtis Robbins, Eric Ceniceros, and Mani Natarajan. Review of biodiesel composition, properties, and specifications. *Renewable and Sustainable Energy Reviews*, 16(1):143–169, January 2012.

[80] Jana Orsavova, Ladislava Misurcova, Jarmila Ambrozova, Robert Vicha, and Jiri Mlcek. Fatty acids composition of vegetable oils and its contribution to dietary energy intake and dependence of cardiovascular mortality on dietary intake of fatty acids. *International Journal of Molecular Sciences*, 16(12):12871–12890, June 2015.

[81] Aniello Costantini and Valeria Califano. Lipase immobilization in mesoporous silica nanoparticles for biofuel production. *Catalysts*, 11(5):629, May 2021.

[82] José M Palomo, Gloria Mu noz, Gloria Fernández-Lorente, Cesar Mateo, Roberto Fernández-Lafuente, and José M Guisán. Interfacial adsorption of lipases on very hydrophobic support (octadecyl=sepabeads): immobilization, hyperactivation and stabilization of the open form of lipases. *Journal of Molecular Catalysis B: Enzymatic*, 19-20:279–286, December 2002.

[83] Yanjun Jiang, Pengju Zheng, Liya Zhou, Weixi Kong, Jing Gao, Jinxia Wang, Jinyan Gu, Xu Zhang, and Xiaomei Wang. Immobilization of lipase in hierarchically ordered macroporous/mesoporous silica with improved catalytic performance. *Journal of Molecular Catalysis B: Enzymatic*, 130:96–103, August 2016.

[84] Bettina Baumgartner, Jakob Hayden, and Bernhard Lendl. Mesoporous silica films for sensing volatile organic compounds using attenuated total reflection spectroscopy. *Sensors and Actuators B: Chemical*, 302:127194, January 2020.

[85] Merck KGaA. `https://www.sigmaaldrich.com/AT/de`. Accessed: 2024-01-15.